High-throughput simulation studies of angiogenesis

Reverse engineering the role of tip cells and pericytes in vascular development

Margriet Palm

Cover: Network formation with tip cells (ivory) and stalk cells (red). The cells are dynamically selected via lateral inhibition and respond less to a chemoattractant that is secreted by all cells. See chapter 4 for further details.

High-throughput simulation studies of angiogenesis

*Reverse engineering the role of tip cells
and pericytes in vascular development*

Proefschrift

ter verkrijging van
de graad van Doctor aan de Universiteit Leiden,
op gezag van Rector Magnificus prof.mr. C.J.J.M. Stolker,
volgens besluit van het College voor Promoties
te verdedigen op dinsdag 30 september 2014
klokke 15.00 uur

door

Margaretha Maria Palm
geboren te Heumen
in 1985

Promotiecommissie:

Promotor: prof.dr. Roeland M.H. Merks

Overige leden: prof.dr. Peter Stevenhagen
                prof.dr. Arjen Doelman
                prof.dr. Reinier O. Schlingemann
                dr. Markus O. Heydenreich

*Voor mama, die mij het vertrouwen
gaf om de grote onbekende wereld om
mij heen te onderzoeken*

Contents

1

Introduction

A large network of blood vessels, called the circulatory system, supplies the body with oxygen and nutrients, and removes the waste products of metabolism. The circulatory system starts to develop early on during embryonic development when groups of cells form primitive networks that later connect to form the circulatory system. Disturbance of blood vessel formation during the early stages of development is often lethal because without blood vessels organs do not develop properly. After birth, blood vessel formation continues to facilitate growth and repair.

The smallest blood vessels, called capillaries, develop in a process that is called angiogenesis. This process plays an important role in the abovementioned physiological processes, but it is also important in many diseases. Two common examples of diseases that involve blood vessel growth are cancer [1] and eye diseases [2]. When a tumor grows too big to directly extract oxygen from its environment, tumor cells start secreting growth factors to attract blood vessels [1]. These new blood vessels supply the tumor with oxygen and nutrients that enable the tumor to grow [1]. Furthermore, the tumor vasculature acts as a conduit for tumor cells to enter the blood stream, which can result in tumor metastasis [1, 3, 4]. Blood vessel growth can cause damage to the retina and this results in an impaired vision or blindness. In various forms of retinopathy, such as proliferative diabetic retinopathy and retinopathy of prematurity, hypoxia induces the formation of new blood vessels [2]. These new vessels can obscure vision or damage the retina. In age-related macular degeneration blood vessels grow behind the retina which also damages the retina [2] and results in a loss of central vision.

Recently, blood vessel formation has also be studied outside of the context of diseases. In the upcoming field of tissue-engineering blood vessel formation is studied because larger tissues and organs can only function when they become vascularized [5–7]. When vascularization of a tissue engineered implant depends on blood vessel ingrowth from the host, vascularization takes a up to several weeks [8]. During this time the core of the implant is deprived of oxygen and nutrients and this could damage the implant. Recent studies have focused on improving blood vessel formation after implantation by using a scaffold or adding angiogenic factors, or on inducing blood vessel growth before implantation [7, 8].

Blood vessel formation is commonly studied in the wet lab, either *in vitro* or *in vivo*. An alternative approach to research blood vessel formation are computational models. Classically, computational models have been used to test or investigate hypotheses generated in the wet lab. This is achieved by translating the biological hypothesis into a model consisting of rules or equations. Then, by solving the equations or simulating the model, the hypothesis can be tested. If the hypothesis is supported by the model, the model can be used further study the hypothesis. Specific parts of the hypothesis can be

studied by altering the model components that describe these mechanisms. Furthermore, in contrast to wet lab experiments, the evolution of any model component, such as cells or chemical concentrations, can be observed without affecting the system. Therefore, computational modeling is good tool for studying blood vessels formation. Ideally, computational modeling is used alongside wet lab experiments. Computational models can help to steer experiments, while wet lab experiments are necessary to validate the model. Together, these two methods can help us to provide new insights in the development of blood vessels in health and disease [9].

In this introductory chapter we first discuss the biological processes by which blood vessels develop. Following this, we provide an overview of the computational modeling approaches used to better understand various aspects of blood vessel formation. Finally, we give an overview of the research that will be discussed in the remainder of this thesis.

1.1 Blood vessel formation

Blood vessels form via two processes: vasculogenesis and angiogenesis [10]. Vasculogenesis is the *de novo* formation of blood vessels, which occurs during embryonic development. During vasculogenesis endothelial cell precursors, called angioblasts, organize into primitive vascular networks [10]. Angiogenesis, is the formation of new blood vessels from existing ones. Via this process the primitive vascular networks that formed during vasculogenesis are remodeled and extended. After birth, angiogenesis is responsible for the formation of blood vessels in growing and healing tissue [10]. Altogether, vasculogenesis is limited to the early stages of embryogenesis while angiogenesis is the main process of blood vessel formation after early embryogenesis. Therefore, we will mainly focus on angiogenesis and the cells involved in this process.

There are two mechanisms of angiogenesis: 1) intussusceptive angiogenesis and 2) sprouting angiogenesis [11]. In intussusceptive, or splitting, angiogenesis vessels split along the longitudinal direction by forming intraluminal tissue [11, 12]. In this manner, blood vessels are remodelled with minimal endothelial cell proliferation and migration, and without proteolysis of extracellular matrix components [11, 12]. These new blood vessels are formed during sprouting angiogenesis, which precedes intussesceptive angiogenesis [12]. Sprouting angiogenesis, is involved in the formation of new blood vessels during growth and regeneration, and in pathological processes such as tumor vascularization and neovascularization of the eye. In sprouting angiogenesis a new vessel sprouts from the side of an existing vessel as is illustrated in Figure 1.1. The wall of a blood vessel consists of quiescent endothelial cells, called *phalanx cells* [13], and pericytes partially cover the outside of

3

the vessel (Figure 1.1**B**). When a tissue becomes hypoxic, it secretes growth factors that activate the phalanx cells in the vessel wall [14]. One of the cells becomes the leader cell, which is called the *tip cell* (Figure 1.1**B**) [15]. When the tip cell migrates further it is followed by other activated cells, which are called *stalk cells* [15], and simultaneously the pericytes detach from the vessel wall (Figure 1.1**C**) [14]. The sprout grows longer because the stalk cells directly behind the tip cell proliferate (Figure 1.1**D**) [15]. As the tip cell moves further away, the cells at the base of the new sprout become quiescent phalanx cells that develop a lumen and recruit pericytes (Figure 1.1**E**) [14]. When the sprout grows longer new sprouts may split of from the initial sprout resulting in branches. Such branches later on connect with other branches, from the same or another sprout, and thereby form a vascular network.
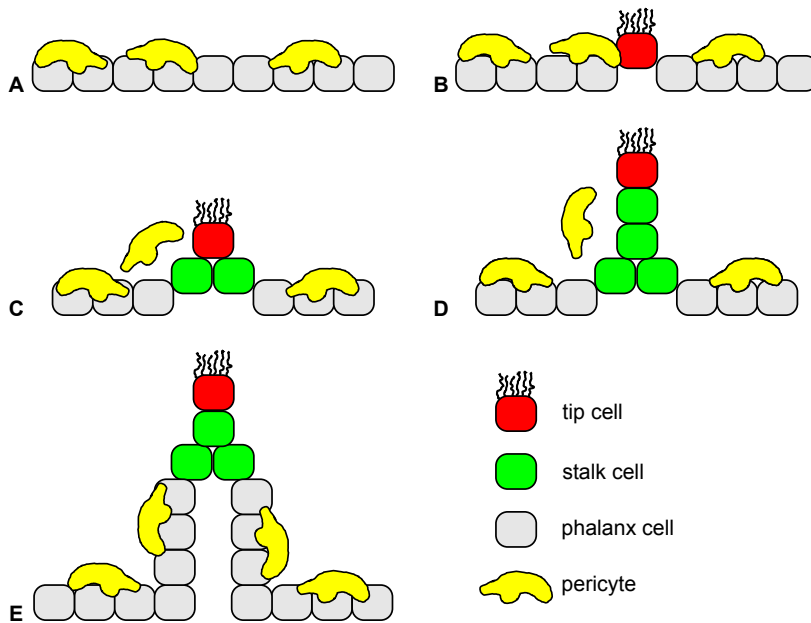
Figure 1.1: Sprouting angiogenesis. **A** row of phalanx cells (gray) that line a the blood vessel and pericytes (yellow) that partially cover the vessel on the outside. **B** one cell is activated and becomes a tip cell that migrates outwards. **C** the stalk cells (green) follow and the pericyte next to these stalk cells dissociates from the vessel. **D** the sprout elongates because the tip cells migrates further and the stalk cells proliferate. **E** at the base of the sprout a lumen forms and pericytes are recruited.

Angiogenesis nor vasculogenesis requires spatial prepatterning or genetic predetermination [9, 16]. Instead, endothelial cells migrate and thereby respond to and change their own environment. This, can affect the behavior of other endothelial cells, either close by or further away. For example, for

sprouting angiogenesis it does not matter which endothelial cell becomes the tip cell. As long as one cells becomes a tip cell the sprout can develop. As the sprout growth, the environment changes and an endothelial cells in the sprout may become a tip cell as well. This cell may either take over the tip [17, 18] or start a new sprout [15]. Thus, endothelial cell collectively self-organize into blood vessels. Whereas genes do not predetermine the vessels that are formed, genes do affect cell behavior. Genes are part of the pathways that regulate cell migration and behavior. These pathways integrate signals from outside, such a membrane-bound ligands of adjacent cells or diffuse ligand, with the genes expressed in the cell. In this manner, cell behavior is adapted to the environment. However, to understand the mechanisms involved in angiogenesis and vasculogenesis, it is not necessary to know all these pathways. Instead, the cell can be used as the main level of abstraction. In this manner we can first understand which cell behaviors are important, and then focus on the source of these behaviors. Therefore, in this thesis we will study angiogenesis with the cell as base unit. We study how certain cell behaviors and interactions to differentially behaving cells affect the patterns that form.

1.2 Computational models of angiogenesis

Computational models have been used to study angiogenesis since the 1980s. Angiogenesis research benefits from this approach in three ways. Firstly, computational models help to gain an overview in this complex system by testing which components and interactions are minimally required. These components and interactions can then be examined to understand their function and predict their effects [19–35]. Computational models are therefore not only useful to gain mechanistic understanding of angiogenesis, but also to find new therapeutic targets. In this manner, computational models can be used to direct experimental studies. Secondly, computational models can discriminate between and select from alternative hypotheses [36–39]. Often, more than one hypothesis explains a biological observation, such as network formation from dispersed endothelial cells. Computational models can test the sufficiency of each hypotheses to reproduce the biological observations. Predictions that result from these models can be validated experimentally to support or reject the tested hypotheses. Thirdly, computational models can connect and combine knowledge on single proteins and mechanisms to examine angiogenesis as a system [17, 40–44]. Experimental research is often limited to a specific step or protein in angiogenesis and does not grasp how this part is integrated in the whole. Ultimately, computational models include processes at multiple scales, like extracellular matrix, cells, and cell-regulation simultaneously. Such a model can than be used to model angiogenesis as it happens in the body and predict how modifications at any scale

affect angiogenesis.

The earliest models of angiogenesis were continuum models that describe angiogenesis in terms of the spatial density of cells. The cell density is described by a set of equations that may include processes such a random cell movement, proliferation, chemotaxis, etc. The main advantage of these models is that they can often be solved analytically, but they are often too abstract to mimic angiogenesis realistically. More complex techniques allow for a more detailed description of angiogenesis, which yields more realistic models. Such techniques include discrete methods such as particle based modeling that describe cells as point-like particles and cell-based models that also explicitly model the cell shape and membrane. These discrete methods are often combined with continuum models, creating a hybrid model in order to utilize the strength of both methods.

In this section we review the contribution of computational modeling to angiogenesis research. First, we discuss how computational modeling resulted in several hypothetical driving mechanisms for vascular network formation. Second, we describe several computational models that are used study specific aspects of sprouting angiogenesis. Finally, we review how the knowledge gained from simple computational models and experiments is used to build large multi-scale models, which can for example be used to study the effects of anti-angiogenic drugs.

1.2.1   Network formation

During early vascular development endothelial cells join into a primitive vascular network. Vascular network formation can be mimicked *in vitro* by seeding endothelial cells on a suitable matrix containing nutrients and angiogenic factors [45]; for example Figure 1.2A shows human umbilical vein endothelial cells (HUVECs) seeded on Matrigel matrix forming a network-like pattern. The conditions in *in vitro* network formation experiments differ greatly from *in vivo* angiogenesis. Yet, specific cases of angiogenesis result in similar vascular networks such as angiogenesis in the yolk sac and retinal angiogenesis [46].

In vitro experiments showed that, after the network is formed, almost all matrix is located beneath the cells [47]. This led to the hypothesis that cells pull on the matrix, resulting in matrix accumulation below cell clusters. The pulling forces of the cells also cause the formation of tension lines, radiating from the clusters, in the surrounding matrix, along which cells migrate [21]. This model assumes that cells can exert traction on the matrix, which results in matrix deformation and heterogeneity of strain in the matrix. Cells preferentially move along the orientation of high stress. The model suggests that matrix remodeling suffices for network formation.

Namy and coworkers [22] combined the effects of cell traction with hap-
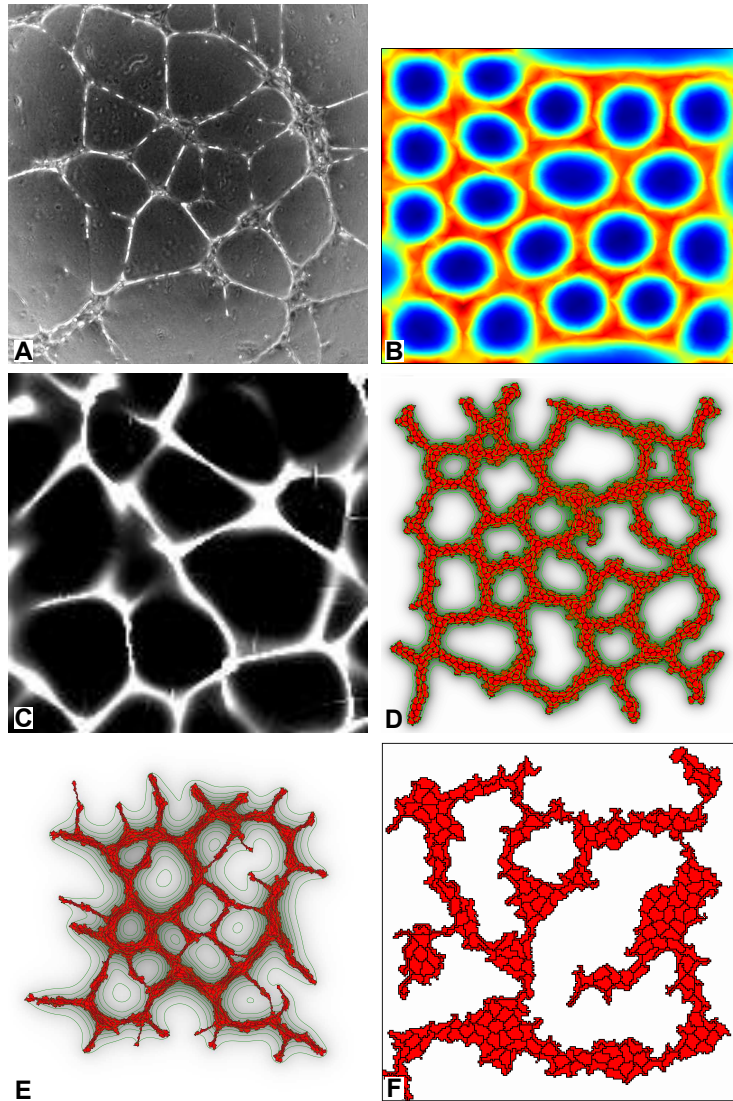
Figure 1.2: Overview of vascular network formation. **A** vasculature developed *in vitro* with HUVEC on Matrigel. **B** networks formed with the mechanical continuum model [22], **C** the chemical continuum model [20], **D** cell-based model with contact inhibition [28], **E** the cell-based model with cell elongation [25]. **F** the cell-based model with preferential attraction to elongated structures [31]. All images were reproduced with the publishers' permission.

totactic cell migration along matrix gradients (Figure 1.2**B**). They found an optimal cell density at which networks can be created, corresponding with experimental observations [48]. Similarly, a range of matrix stiffness, which is linked to the fibrin density of the experimental matrix, was tested. This model suggested that active cell migration may be required for network formation which contradicts the observations by Manoussaki *et al.* [21].

Both previous models consider mechanical interactions between cells and the matrix to be the driving forces for network formation. Serini *et al.* [19, 20] proposed that chemotaxis is the driving force of network formation [20]. In the *in vitro* models cells move predominantly towards regions of high cell density suggesting that the cells are attracted by a chemoattractant secreted by the cells. Therefore, Serini *et al.* built a the computational model in which cells secrete a chemoattractant to which cells move preferentially. This model produces network-like patterns as shown in Figure 1.2**C**. Two important predictions are made based on this model. First, the model predicts an optimal cell density for the formation of stable vascular networks and second, the size of the meshes in the network depend on the diffusivity and decay rate of the chemoattractant.

The mechanical and chemical hypotheses for vascular network formation have also been combined in one mechanochemical model [37]. This continuum model hypothesizes that network formation consists of two stages. First, cells move upwards chemical gradients. Second, at higher local cell density, the cells do not sense the gradient, but the high cell density signals them to start remodeling the matrix. This then attracts cells to the high density regions. The mechanochemical model showed that these assumptions indeed lead to network formation and that chemotaxis drives the formation of networks while mechanical interactions stabilize the formed network. However, the mechanochemical model cannot reproduce all observations from both the chemical and mechanical angiogenesis models. Therefore, a more detailed description of the matrix mechanics is required that also influences early cell migration.

Clearly, multiple hypotheses can be used to explain the experimentally observed network formation. Moreover, model observations and predictions for both the mechanical and the chemotaxis model could be reproduced *in vitro* [20, 22]. The mechanical models show that matrix thickness and stiffness may be determining factors in network formation, as has been show experimentally [47]. The chemical models reproduce the VEGF dependence that has be observed *in vitro* [20] as well as a characteristic length of the networks that depends on the diffusivity of the chemoattractant [49]. Both models only produce one similar prediction; there is an optimal cell density for network formation, below this density cells disconnect and above this density cells aggregate [48]. Therefore, it remains unclear whether the two mecha-

nisms are involved in angiogenesis in different environments, or that the two mechanism act consecutive or simultaneously during angiogenesis.

The models discussed so far use a continuum description for both cells and mechanical or chemical fields, meaning that cells and fields are described as densities. This kind of description is appropriate for mechanical and chemical fields; for example, the concentration of a specific chemical can be measured at a specific position and can have any value. However, generalization of cells into cell densities ignores cell behavior, cell size and shape, and cell-cell interactions, which are often key to morphogenic processes such as angiogenesis. Therefore, cells should be the basis of an angiogenesis model. Cell-based models incorporate detailed cell-cell interactions as well as cell shape and size, which can also be measured experimentally for quantification of the parameters and the predictions of the models [9]. Dynamic cell properties and behavior can be added by extending each cell with regulation networks, such as signaling or genetic pathways. Altogether, cell-based models are a solid basis for computational angiogenesis models that can be used to explain tissue effects at the cell level [16].

Various hypotheses for vascular network formation have been modeled using cell-based models. One of these models is a hybrid cell-based model, using the cellular Potts method (CPM), which is based on the assumption that cells chemotact toward a chemoattractant that they themselves secrete [25–29]. This assumption is similar to the assumption used for the continuum chemotaxis model [20]. In this cell-based model the cells' shape, size and membrane surface are described explicitly, and chemicals are described as continuous fields. One of the main advantages of this cell-based model is the more realistic chemotactic response of cells. This cell based model can be used to simulate network formation solely by defining cell behavior and properties. When only autocrine chemotaxis is included, network formation only occurs for narrow parameter ranges: strongly adhering cells or steep chemical gradients [26, 27]. However, three alternative hypotheses are proposed that allowed network formation for a much wider range of parameters: contact inhibition [28], cell elongation [25] and ECM-chemoattractant binding [29].

The contact inhibition hypothesis proposes that cells only respond to the autocrine chemoattractants where the cell membrane is not in contact with other cells. This exclusive sensing is thought to be mediated through the dual function of VE-cadherin; it acts as a homophilic trans-membrane cell-adhesion molecule and it plays an inhibitor role in the VEGF signaling pathway [50] which increases cell motility. Therefore, cells that are surrounded by other cells do not respond to VEGF. This process appears to contribute to both network formation (Figure 1.2**D**) and sprouting angiogenesis. The reasons for this are best understood in the context of sprouting angiogenesis and will

therefore be discussed in section 1.2.2.

The cell elongation hypothesis is based on the biological observation that cells elongate during network formation. In this model, the combination of elongated cells with autocrine chemotaxis results in network formation [25]. The final network, which can be observed in Figure 1.2**E**, is similar to *in vitro* networks. When cell elongation is omitted, cells aggregate instead of forming network, indicating that cell elongation drives network formation in this model. The evolution of network properties over time, such as the number of nodes and meshes, corresponds with data from *in vitro* experiments with HUVECs on Matrigel. This suggests that cell elongation may play an important rule during network formation. In this model network formation occurs at two time-scales. First, cell elongation induces a persistent movement along the long axis of the cell. This causes the formation of thin branches of connected cells. Second, the network coarsens by fusion of branches and mesh collapse. This is driven by the chemotaxis that enables slow migration of cells along their short axis.

The ECM-chemoattractant binding hypothesis is based on binding of the chemoattractant to the ECM. VEGF is a known chemoattractant for endothelial cells and it has heparin binding domains that cause VEGF to bind to the ECM [51]. Köhn-Luque *et al.* [29] developed a model based on this hypothesis using the CPM. In this model unbound VEGF is produced everywhere and ECM molecules that bind VEGF are produced by cells. Unbound VEGF can bind to the ECM molecules resulting in bound VEGF. When cells respond more to bound VEGF than unbound VEGF, a network forms that is similar to the network that develops during the first two ours of HUVECs on Matrigel [52]. Interestingly, cells in the branches of the network elongate by themselves. This may suggest that cell elongation is a second step in network formation that drives the formation of longer branches and network coarsening.

An alternative hypothesis that is not based on chemotaxis was proposed by Szabó *et al.* [30, 31, 38]. Their experiments suggested that neither mechanical interactions nor chemotaxis are required for network formation [30] and that cells move preferential towards elongated cells. From these observation they propose that network formation is driven by the *preferential attraction to elongated structures*. This hypothesis has been used as a basis for both a particle based model [30] and a cell-based model [31, 38]. In the particle based model cells are represented by point particles that diffuse and are attracted by their neighbors. While this model lacks some key cell properties, including cell shape, it suffices as a *proof-of-concept* model for preferential attraction to elongated structures. The more detailed cell-based models are used to investigate network formation from dispersed cells [31] and sprouting from a blob of cells [38]. This model suggests that cells can indeed form networks due to short range cell-cell interactions, as is shown in Figure 1.2**F**.

Sprouts formed in these networks only become stable when they connect to other sprouts, suggesting that anastomosis stabilizes the formed network.

Because they all produce similar morphological patterns, none of the modeled hypotheses can be ruled out as a driving force for network formation. Cell-based models [25–28] suggest that autocrine chemotaxis, combined with cell properties such as contact inhibition of cell elongation, may drive angiogenesis. Other cell-based angiogenesis models [30, 31, 38] have suggested that chemotaxis may not be necessary at all. Furthermore, mechanical interactions between the cells and the matrix may facility network formation. It is likely that each of these mechanisms plays a role in vascular network formation and that it depends on the circumstances which mechanism is dominant.

1.2.2 Sprouting

Sprouting angiogenesis is the formation of new vessels by creating a sprout from the wall of the existing vessel (Figure 1.1). This form of angiogenesis is often observed in the vicinity of hypoxic tissue that secretes angiogenic factors, *e.g.,* a growing tumor, which activates and attracts endothelial cells from the existing vessels [53]. By stimulating the formation of a new vasculature, a tumor is able to grow and proliferate. The mechanisms underlying the dynamics of sprouting angiogenesis are still poorly understood. What mechanisms guide the growing sprout? How do biochemical and biomechanical interactions of the ECM with cells effect sprouting? Is proliferation required and where is proliferation located in the sprout? How are tip cells selected in the vessel and what causes sprouts to branch? Computational models have contributed to a better understanding of these issues.

Experiments in corneal angiogenesis show that migration of activated endothelial cells and initial sprouting precedes stalk cell proliferation [55] and this proliferation is necessary for sprout elongation [56]. These observations indicate that sprouts will not reach the tissue that induced sprouting when endothelial cells cells are not able to divide. A continuum model [32] describes the change in cell density over time due to cell migration driven by cell diffusion, chemotaxis and haptotaxis. The initial configuration of the simulation consists of a blood vessel at one side and a tumor at the other side of the simulation domain. This tumor secretes a chemoattractant, resulting in a gradient of chemoattractant that attracts cells towards the tumor. Haptotaxis is induced by fibronectin that the cells secrete themselves. The highest levels of fibronectin are present where the cell density is maximum. Therefore, haptotaxis and chemotaxis work in opposite directions. The continuum model suggests that, in absence of proliferation, the sprouting is restricted. The authors propose that this is caused because haptotaxis outweighs chemotaxis and increasing the number of cells would increase the chemotactic response.

A drawback of this model is that it describes cells as a density field, hence it
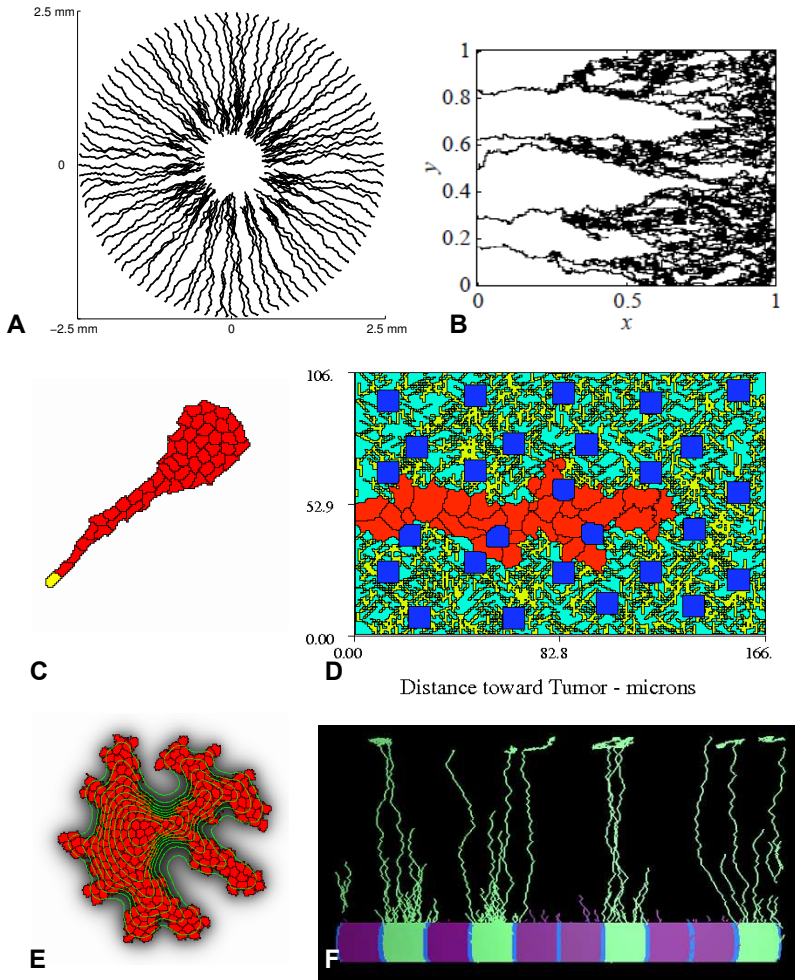
Figure 1.3: Overview of the computational models of angiogenic sprouting. **A** corneal angiogenesis as modeled in the discrete model based on tip cell elasticity and stalk cell adhesion [35]. **B** networks formed with the discrete model with chemotaxis and fibrinectin induced haptotaxis [54]. **C** sprouting induced by preferential attraction to elongated structures in a cell-based model [38]. **D** sprouting angiogenesis in a cell-based model with a heterogeneous ECM [34]. **E** sprouting induced by contact inhibition of chemotaxis [28]. **F** tip cell selection and sprouting in an agent-based model [41]. All images were reproduced with the publishers' permission.

cannot describe how the sprout breaks up due to lack of proliferation. Therefore, a discrete modeling approach has been introduced to study cell proliferation in the sprout [35]. As illustrated in Figure 1.3A, the model mimics a cornea with a lesion in the center from which VEGF is secreted. A sprout grows from the periphery and consist of multiple cell types; one leading tip cell and multiple following stalk cells. The tip cell is attracted by VEGF and therefore migrates towards the center of the cornea. Tip cell migration is limited by the elasticity of the tip cell and the strength of the adhesion between stalk cells. Adding proliferation enables unlimited sprout extension. This model suggests that basic cell properties can explain the need for proliferation in sprouting.

The previous two sprouting models only considered cell behavior and chemical fields, ignoring all ECM and stromal tissue. Anderson and coworkers [54] created a particle based, hybrid model describing sprouting angiogenesis. In this model cells are represented as point particles on a grid while the chemotactic and haptotactic fields are still described as continuum equations. This model was used to investigate how the balance of haptotaxis and chemotaxis influences branching and anastomosis. As shown in Figure 1.3**B** branching and anastomosis occur in the model, but these behaviors only occur when cells are able to move perpendicular to the chemotactic field, which is enabled by haptotaxis. When the haptotactic forces are strong enough branches can split and reconnect in order to form a functional vasculature.

Anderson *et al.*'s model [54] suggests that haptotaxis is key to branching, but it did not show how cells interact with their heterogeneous environment. A more recent, cell-based, model represents the ECM as a static, heterogeneous configuration of matrix fiber bundles, interstitial fluid and immobile tissue-specific cells [34]. The endothelial cells in the model are motile and adhere stronger to matrix fibers than to the surrounding matrix. Immobile cells act as obstacles that hinder the migration of endothelial cells. The tip cell is influenced by a chemoattractant field and it degrades ECM components. Degradation of the extracellular matrix during sprouting enables cells to migrate and branch off the main sprout as shown in Figure 1.3**D**. The model suggests that a heterogeneous composition of the matrix is necessary for the formation of branches; the inhomogeneities in the matrix enable cells to split from the main branch. Furthermore, the model suggests that the proliferation region determines sprouting dynamics but does not affect the final sprout morphology.

A follow-up model was used to investigate cell-ECM interaction in more detail [33]. In this model all cells respond to the chemoattractant and that the immobile tissue cells are removed, *i.e.*, only fibers cause matrix heterogeneity. The model suggests that sprouting only occurs in a specific range of matrix densities, which corresponds with experimental observations. Moreover, simulation results suggest that low fiber density results in cell elongation.

Similar changes were observed when the random fibers were replaced by a specific fiber pattern, for example long fibers cause cells to elongate in the same direction as the fibers. The authors propose that contact guidance, due to cell-matrix interactions, is key to role in vascular sprouting because it enables sprout branching in an inhomogeneous matrix.

All of the discussed models assumed an external source that induces sprouting. In contrast, both Szabó *et al.* [38] and Merks *et al.* [28] have proposed that cells can form sprouts in absence of external signals and in a homogeneous matrix. They supported their hypothesis with cell-based models that describe cell shape, cell membrane and cell migration in much more detail than the models discussed before.

The model by Szabó *et al.* [38] incorporates preferential attraction to elongated structures, cell polarity and self-propulsion (i.e. persistence of motion). The model also differentiates between tip and stalk cells. The tip cell is polarized, causing directed movement in the direction of the polarization vector. The results shown in Figure 1.3**C** suggest that both preferential attraction and self-propulsion are necessary to reproduce realistic sprouting behavior. Cell polarization may be regulated by cell-cell contacts and VE-cadherin may be a key player for this. Moreover, the model suggest that differential behavior at the sprout tip may drive sprout formation.

In contrast, Merks suggested that sprouting can occur in absence of matrix heterogeneity or differential cell behavior [28] (1.3**E**). The model assumes cells are attracted towards an autocrine chemoattractant, using similar rules as in chemotaxis-based network model (section 1.2.1). Contact inhibition mediated by VE-cadherin causes cells to be only sensitive to the chemoattractant at positions of the cell membrane adjacent to the ECM. Sprouting occurs in two ways. First, when cells are arranged in an aggregate, only the outer layer of cells sense the chemoattractant. These cells tend to migrate towards the center of the aggregate causing a buckling instability that induces sprouting. This effect enables cells, even those with a low motility, to move against the chemotactic gradient. Second, another mechanism may explain sprouting for highly motile cells. To move away from the parent vessel and form a sprout, cells must migrate *against* a steep gradient of self-secreted chemoattractant. Once a small sprout is created by a motile cell, the gradient around this outgrowth is less steep than the rest of the gradient, so cells within the sprout have higher motility than elsewhere, causing an instability.

Several of the previously discussed models defined the cell leading a sprout as the tip cell [34, 35, 38]. However, tip cell fate is regulated during angiogenesis via intercellular Dll4-Notch [57–60] signaling and VEGF signaling [60–63]. Bentley *et al.* [41] investigate the molecular and biophysical mechanisms driving tip and stalk cell differentiation using an agent-based, computational model [41] of a single row of endothelial cells. In this model, tip

cell fate is induced by VEGF and regulated by lateral inhibition of tip cell fate via Dll4-Notch signaling. When a cell becomes a tip cell, it starts extending long filopodia away from the blood vessel (Figure 1.3**F**). Based on this model Bentley *et al.* proposed that the balance between VEGF signaling and Dll4-Notch determines the transition from normal to abnormal sprouting [41, 42]. An extension of the same model was used to study tip cell competition in angiogenic sprouts. Time-lapse microscopy has shown how stalk cells migrate along the sprout and compete with the leading tip cell [17]. Cells that are treated such that they express higher levels of the VEGF receptor VEGFR2 are found more often at the sprout tip than wild-type cells. Blockage of Notch signaling neutralized this effect. Based on these observations Jakobsson *et al.* [17] proposed that tip cell compete for the tip position and that this is controlled by both VEGF signaling and Dll4-Notch signaling. In the computational model this hypothesis reproduced tip cell shuffling, suggesting that this mechanism may explain tip cell shuffling.

1.2.3   Predictive angiogenesis models

The models discussed so far, all isolated specific aspects of angiogenesis. To build predictive models of *in vivo* angiogenesis, we must incorporate the interactions with the rest of the body in a multi-scale model. Angiogenesis is induced by hypoxic tissue which, for example, can be a tumor or an active muscle. The change in oxygen and nutrient supply due to the new vasculature changes the signals coming from the tissue, resulting in a dynamic feedback loop between angiogenesis and the needs of the tissue. Also blood flow may be key to this feedback. Dysfunctional vessels are not able to support blood flow and do not contribute to the perfusion of the tissue. Endothelial cells change their behavior due to the shear stresses induced by blood flow [64]. The inclusion of these processes in a multi-scale angiogenesis model would be a great tool to study pathological processes either involve excessive or insufficient blood vessel growth. Such multi-scale models can be used to formalize and validate hypotheses, and to predict the effects of pro- or anti-angiogenic therapies on the vasculature and the other tissues involved.

  In order to build these multi-scale models, researchers often extend existing models. For example, the particle-based sprouting model by Anderson *et al.* [54] has been extended with blood flow [65]. This model suggested that most vessels are not perfused due to the lack of anastomosis, and thus drugs can not reach the target. More complex approaches have been used to combine more detailed angiogenesis models with blood flow and the kinetics of oxygen and VEGF [44, 66, 67]. With these models vascularization in a heterogeneous ECM [44] and in skeletal muscle [43] has been simulated.

  Also, cell-based models have been extended to include multiple tissues. Shirinifard *et al.* [68] combined cell-based models of blood vessel formation and

tumor growth to investigate how tumor growth and vascular remodeling interact. In this model the tumor induces angiogenesis in a peripheral vasculature. The new blood vessels supply the tumor with oxygen and growth factors and thereby affect the tumor development. Another example of a multi-scale, cell-based model was presented by Kleinstreuer *et al.* [40]. They modeled vasculogenesis including several types of cells and proteins in order to test the effects of various toxins on vascular development. For this they classified the effects of the toxins on the behavior of a single cell and included this in the model. The model was able reproduce the pattern formed in HUVEC cultures treated with various toxins, showing that this approach is useful to further study the effects of toxins on vascular development.

These first approaches on multi-scale, cell-based modeling of blood vessel formation indicate that this is a suitable approach for predictive modeling. However, extra steps, such as including mechanical interactions with the ECM and blood flow, subcellular signaling, and interactions between endothelial cells, perivascular and stromal cells, should be included to create reliable, predictive models of angiogenesis. Before, such effects can be included, they should be studied thoroughly in more simple, cell-based models.

1.3   Thesis outline

In this thesis we focus on the role of specialized cells in angiogenesis. This includes cells with distinctive behaviors, such as elongated cells, or cells with a specific role, such as tip cells or pericytes. These specialized cells are observed *in vivo* [15, 69–71], but *in vitro* blood vessel formation there specific properties are dispensable. Therefore, we aim to better understand the role of these specialized cell types in blood vessel formation. For this we use simple, cell-based models of vascular network formation, either via sprouting angiogenesis or vasculogenesis. In these models we focus on the cell scale and therefore we do not include the cause of the cell behaviors in the models or incorporate any high-level rules. Furthermore, we assume that the environment of the cells does not provide any structural, mechanical or chemical guidance to the cells. In this manner we build models in which we isolate cell behavior, similar to what happens in various *in vitro* models of blood vessel formation.

The cell behaviors we study in our models is not limited to the behavior that is described in the literature. Potential cell behaviors may still be undiscovered. And, often cell behavior is described at a level that is not applicable for our modeling approach. With our model we can assign any kind of behavior to the cells and study how this affects morphogenesis. In this manner we can predict the behavior of cells involved in blood vessel formation that have not been described in the literature. In order to study large ranges of cell behav-

iors with cell-based models, large parameter sweeps were necessary. Unlike classic methods, such as PDE models, no standard methods are available for this. Therefore, in chapter 5, we present a protocol for setting up, running and analyzing large scale parameter sweeps with cell-based models. In chapter 5 we demonstrate how this protocol was used to obtain the results presented in chapter 2. Furthermore, we show how the method can be applied to an alternative cell-based model.

In chapter 2 we further analyze the formation of blood vessels by elongated cells. Previously, it was shown that elongated cells form networks [25], but the precise mechanisms by which elongated form networks remained unclear. To better understand how elongated cells form networks, we quantify the alignment of cells during network formation and show that elongated cells align over time. Using these analyses we show that elongated cells align and that due to this alignment the rotation of the cells becomes limited. As a result the cells form a network-like structure that is in a state of dynamic arrest.

In chapters 3 and 4 we study how mixing of specialized cells, *i.e.* cells with different behaviors, affects vascular network formation. In chapter 3 we study how pericytes, a kind of perivascular cell, affect vasculogenesis. For this we combined *in vitro* experiments with a cell-based, computational model. With our model we studied which interactions between endothelial cells and pericytes could be responsible for the patterns observed *in vitro*. In this manner we showed that during blood vessel formation pericytes and endothelial cells may attract each other by diffusing chemoattractants. In chapter 4 we used our computational modeling approach to gain new insights in the molecular and behavioral differences between tip cells and stalk cells. With a large parameter sweep we searched for those cell behaviors that could make tip cells lead and affect network formation. In this manner we found that tip cells that respond less to an autocrine chemoattractant lead sprouts and affect network formation. This result seemed to contradict with the literature because tip cells are described as highly motile cells that respond more to chemoattractants. However, the chemoattractants to which tip cells are reported to respond more are chemoattractants secreted by hypoxic tissues, while in our model the chemoattractant is secreted by the endothelial cells. Furthermore, a literature study of tip cell gene expression in tip and stalk cells indicated that tip cells do not express the receptor for the endothelial cell chemoattractant Apelin. Blocking Apelin signaling in *in vitro* sprouting assays reduces sprouting, but only when tip cells were present in the spheroids. This support the hypothesis that the differential response of tip and stalk cells to Apelin could cause tip cells to lead sprouts.

2

Vascular networks due to dynamically arrested crystalline ordering of elongated cells

background graphic: ordering in networks formed with elongated cells and chemotaxis (Figure 2.2**B**)

Abstract

Recent experimental and theoretical studies suggest that crystallization and glass-like solidification are useful analogies for understanding cell ordering in confluent biological tissues. It remains unexplored how cellular ordering contributes to pattern formation during morphogenesis. With a computational model we show that a system of elongated, cohering biological cells can get dynamically arrested in a network pattern. Our model provides a new explanation for the formation of cellular networks in culture systems that exclude intercellular interaction via chemotaxis or mechanical traction.

2.1 Introduction

By aligning locally with one another, cells of elongated shape form ordered, crystalline configurations in cell cultures of, e.g. fibroblasts [72, 73], mesenchymal stem cells [73], and endothelial cells [74]. Initially the cells form small clusters of aligned cells; the clusters then grow and the range over which cells align increases with time [73, 75]. To study the emergence of such crystalline cellular ordering, it is useful to make an analogy with liquid crystals [73]. For example, a "cellular temperature" can be defined to describe the cell-type specific persistence (low cellular temperature) or randomness (high cellular temperature) of cell motility, where cells of high cellular temperature (*e.g.,* fibroblasts) are less likely to form crystalline configurations than cells of low temperature (*e.g.,* mesenchymal stem cells) [73]. It was similarly proposed that collective cell motion in crowded cell sheets can be understood as system approaching a glass transition [76, 77]. Although these studies provide useful insights into the ordering of cells in confluent cell layers, it remains unexplored how crystallization and glass-like dynamics contribute to the formation of more complex shapes and patterns during biological morphogenesis.

Cells' organizing into network-like structures, as it occurs for example during blood vessel development, is a suitable system to study how cellular ordering participates in pattern formation. In cell cultures after stimulation by growth factors (VEGFs, FGFs), endothelial cells elongate and form vascular-like network structures [78–80]. The mechanisms that drive the aggregation of endothelial cells and their subsequent organization into network is a subject of debate. Most models assume an attractive force between cells, either due to chemotaxis [19, 20, 25–29, 49, 81] or due to mechanical traction via the extracellular matrix [21–24, 82, 83]. *In vitro* experiments show that astroglia-related rat C6 cells and muscle-related C212 cells can form network-like structures on a rigid culture substrate [30], which excludes formation of mechanical or chemical attraction between cells. Therefore a sec-

ond class of explanations proposed that cells form networks by adhering better to locally elongated configurations of cells [30] or elongated cells [31]. Here we show that, in absence of mechanical or chemical fields such mechanisms are unnecessary: elongated cells organize into network structures if they move and rotate randomly, and adhere to adjacent cells. As the cells align locally with one another, a network pattern appears. Additional, long-range cell-cell attraction mechanisms, e.g., chemotaxis or mechanotaxis, act to stabilize the pattern and fix its wave length.
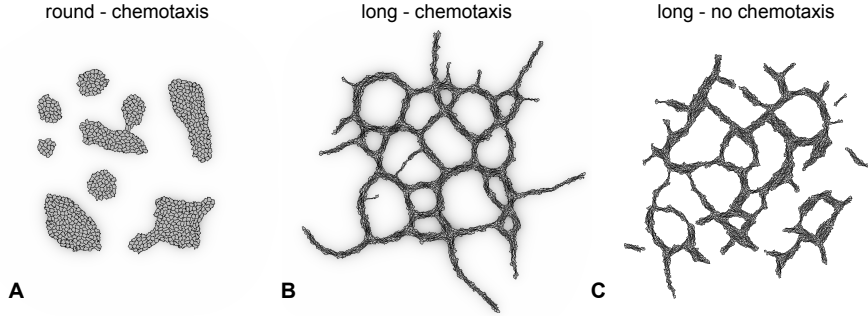
Figure 2.1: Effect of chemotaxis and cell shape on pattern formation. **A** round, chemotacting, and adhesive cells (10,000 MCS), **B** elongated, chemotacting and adhesive cells (10,000 MCS), and **C** elongated, non-chemotacting and adhesive cells (250,000 MCS). In all panels 700 cells are seeded on the center 500x500 pixels of an 800x800 lattice.

2.2 Model description

To model the collective movement of elongated cells, we use the cellular Potts method (CPM), also known as the Glazier-Graner-Hogeweg model [84, 85], a lattice-based, Monte-Carlo model that has been used to model developmental mechanisms including somitogenesis [86, 87], convergent extension [88] and fruit fly retinal patterning [89]. The CPM represents cells as connected patches of lattice sites with identical spin $\sigma \in \mathbb{N}$; lattice sites with spin $\sigma = 0$ represent the extracellular matrix (ECM). To simulate stochastic cell motility, the CPM iteratively displaces cell-cell and cell-ECM boundaries by attempting to copy the spin of a randomly selected site into a randomly selected adjacent lattice site $\vec{x}$, monitoring the resulting change ΔH of a Hamiltonian,

$$H = \sum_{(\vec{x}, \vec{x}')} J(\sigma(\vec{x}), \sigma(\vec{x}')) \left(1 - \delta(\sigma(\vec{x}), \sigma(\vec{x}'))\right) + \sum_{\sigma} \lambda_{\mathsf{A}} (a(\sigma) - A)^2 + \sum_{\sigma} \lambda_{\mathsf{L}} (l(\sigma) - L)^2 \,.$$

A copy attempt will always be accepted if $\Delta H \leq 0$, if $\Delta H > 0$ a copy attempt is accepted with the Boltzmann probability $P(\Delta H) = \exp(-\Delta H / \mu(\sigma))$, with $\mu(\sigma)$ a "cellular temperature" to simulate cell-autonomous random motility. For simplicity, we here assume that all cells have identical temperature μ. The time unit is a Monte Carlo step (MCS), which corresponds with as many copy attempts as there are lattice sites.

The first term of Equation 2.2 defines an adhesion energy, with $(\vec{x}, \vec{x}')$ a pair of adjacent lattice sites and the Kronecker delta returning a value of 1 for pairs at cell-cell and cell-ECM interfaces, or zero otherwise. In the model two contact energies are defined: $J_{\text{cell,cell}}$ for $\sigma > 0$ at both lattice sites, and $J_{\text{cell,ECM}}$ for $\sigma = 0$ at one lattice site. The second and third term are shape constraints that penalize deviations from a target shape, with A and L a target area and length, and $a(\sigma)$ and $l(\sigma)$ the current area and length of the cell; λ_A and λ_L are shape parameters. We efficiently estimate $l(\sigma)$ by keeping track of a cellular inertia tensor as previously described [25].

In a subset of simulations, we further assume that cells secrete a diffusing chemoattractant c, which we describe with a partial differential equation:

$$\frac{\partial c(\vec{x}, t)}{\partial t} = D\nabla^2 c(\vec{x}, t) + s(1 - \delta(\sigma(\vec{x}), 0)) - \epsilon\, \delta(\sigma(\vec{x}), 0),$$

with diffusion constant D, secretion rate s and decay rate ϵ. After each MCS, a forward Euler method solves Equation 2.2 for 15 steps with $\Delta t = 2$ s and zero boundary conditions. To model the cells' chemotaxis up concentration gradients of the chemoattractant, during each copy attempt from $\vec{x}$ to $\vec{x}'$ we increase ΔH with a $\Delta H_{\text{chemotaxis}} = \lambda_c\left(c(\vec{x}) - c(\vec{x}')\right)$, with λ_c a chemotactic sensitivity [90].

We use the following parameter settings, unless specified otherwise: $\mu = 1$, $J_{\text{cell,cell}} = .5$, $J_{\text{cell,ECM}} = .35$, $\lambda_A = 1$, $\lambda_L = .1$; $\lambda_c = 10$, $A = 100$ l.u.^{2}, $L = 60$ l.u.; $D = 10^{-13}$ m^{2}s^{-1}, $\epsilon = 1.8 \cdot 10^{-4}$ s^{-1}, $s = 1.8 \cdot 10^{-4}$ s^{-1}; where l.u. denotes a lattice unit which corresponds with 2 μm. Adjacent lattice sites $\vec{x}'$ are defined as the eight nearest neighbors of lattice site $\vec{x}$. Unless stated otherwise, a simulation is initialized with 175 cells randomly distributed on a 220x220 area at the center of a 400x400 lattice.

2.3   Results

As Figure 2.1 shows, and in agreement with previous reports [25], if we allow for chemotaxis, rounded cells accumulate into rounded clusters (Figure 2.1**A**) and elongated cells aggregate into networks (Figure 2.1**B**). Interestingly, however, chemotaxis is not required for network formation: cell-cell adhesion between elongated cells suffices for forming networks (Figure 2.1**B**). Movies corresponding with Figure 2.1**B** and **C** (See Supplemental Movie S1, model without chemotaxis, and Movie S2, model with chemotaxis) suggest that the

gradual alignment of cells with their neighbors is key to network formation and network evolution. To characterize this cell alignment, we define $\theta(\vec{x}, r)$ as the angle between the direction of the long axis $\vec{v}(\sigma(\vec{x}))$ of the cell at $\vec{x}$, and a local director $\vec{n}(\vec{x}, r)$, a weighted local average of cell orientations defined at radius r around $\vec{x}$:

$$\vec{n}(\vec{x}, r) = \langle \vec{v}(\sigma(\vec{y})) \rangle_{\{\vec{y} \in \mathbb{Z}^2 : |\vec{x} - \vec{y}| < r\}} \, .$$

Figure 2.2**A** and **B** depict the value of $\theta(\vec{x}, 3)$ for simulations without chemotaxis (Figure 2.2**A**) and with chemotaxis (Figure 2.2**B**), with dark gray values indicating values of $\theta(\vec{x}, 3) \rightarrow \pi/2$. Network branches are separated by large values of $\theta(\vec{x}, 3)$, indicating that within branches cells are aligned, whereas branch points are "lattice defects" in which cells with different orientations meet.

Supplemental Movies S3 and S4 ($\theta(\vec{x}, 3)$) show how the cells align gradually over time in the absence and presence of chemotaxis. To characterize the temporal development of cell alignment in more detail, we use an orientational order parameter [91]:

$$S(r) = \left\langle \cos(2\theta(\vec{X}(\sigma), r)) \right\rangle_{\sigma}$$

with $\vec{X}(\sigma)$ the center of mass of cell σ. S ranges from 0 for randomly oriented cells to 1 for cells oriented in parallel.

Figure 2.2**C** shows the evolution of the global orientational order parameter $\lim_{r \to \infty} S(r)$ and of the local orientational order parameters $S(20)$ and $S(40)$. Both with chemotaxis (dashed lines) and without (solid lines), $S(20)$ grows more quickly and reaches higher ordering than $S(40)$. The reason for this is that in cells of length $50 - 60$ l.u., $S(20)$ (covering cells up to a radius $r = 20$ from the cell's center of mass) only detects lateral alignment of cells, whereas a radius $S(40)$ also detects linear line-up of cells (Figure 2.2**D**). Thus cell-cell adhesion of long cells quickly aligns cells with the left and right neighbors, while it aligns them more slowly with those in front and behind. This results in networks with short branches of aligned cells. Interestingly, chemotaxis aligns cells more rapidly, both along the short and long sides of cells, resulting in networks with much longer branches than with adhesion alone.

Next we analyze the mechanisms that drive the orientational ordering in the cell networks. Visual inspection of the simulation movies suggests that single cells move and rotate much more rapidly than locally aligned clusters of cells. A network of locally aligned cells forms rapidly from initially dispersed cells. Merging of branches seems to be a much slower process, and potentially prevents a further evolution to global nematic order. To quantify these observations we measured the translational and rotational diffusion coefficients of cells as a function of the size of the network branch to which it
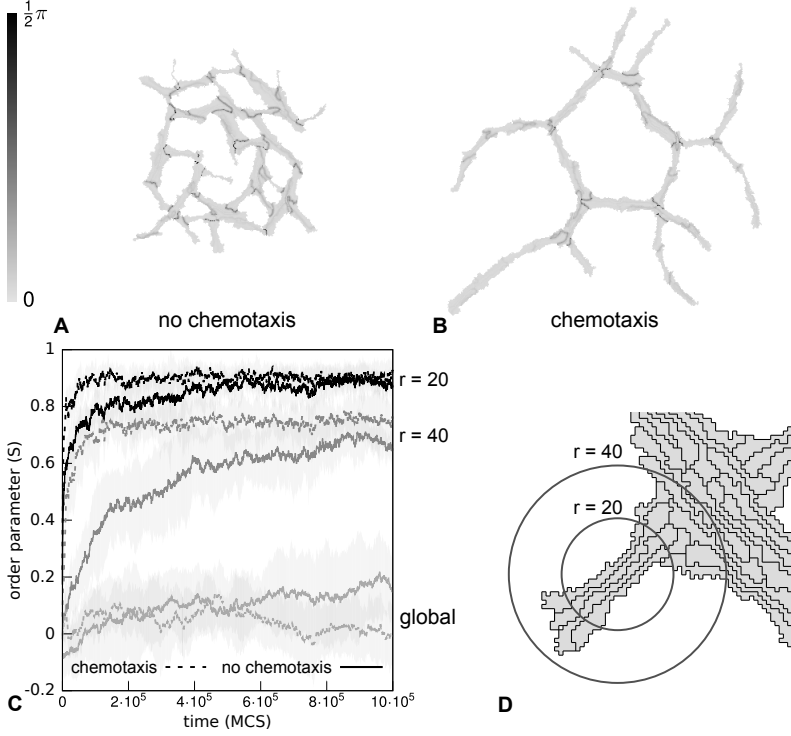
Figure 2.2: Crystalline cell ordering during network formation. **A-B** $\theta(\vec{x}, r)$ with $r = 3$ for a simulation with chemotaxis (**A**) and without chemotaxis (**B**) after 25,000 MCS. **C** Temporal evolution of orientational order parameter $S(r)$ for $r = 20$ (black curves), $r = 40$ (gray curves) and $r \to \infty$ (light gray) without chemotaxis (solid) and with chemotaxis (dashed). Order parameter is averaged over 10 simulation repeats (gray shadows represent standard deviation). **D** cells included in the order parameter with $r = 20$ and $r = 40$.

belongs. We loosely define a network branch, or *cluster* of aligned cells as a connected set of at least two cells with relative orientations $< 5°$, *i.e.*, in Figure 2.2**A** and **B** dark gray values separate the clusters. To detect clusters computationally, we first identify the connected sets for which $\theta(\vec{x}, 3) \leq 5°$, which are surrounded by lattice sites of $\sigma = 0$ or sites with $\theta(\vec{x}, 3) > 5°$. We then eliminate connected sets of fewer than fifty lattice sites. The CPM cells sharing at least 50% of their lattice sites with one of the remaining sets form a cluster. The translational diffusion coefficient, D_t, derives from the mean square displacement (MSD) of a set of cells:

$$\left\langle |\vec{X}(\sigma, t) - \vec{X}(\sigma, 0)|^2 \right\rangle_\sigma = 4D_t t.$$

Similarly, the rotational diffusion coefficient, D_r, derives from the mean square
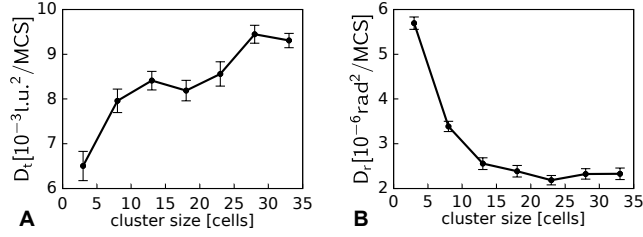
Figure 2.3: Relation between cluster size and cell displacement. Clusters are calculated for each morphology between 500 and 25,0000 MCS (100 simulation repeats), with an interval of 500 MCS; see text for details. The error bars represent the standard error of the linear fits used to estimate diffusion coefficients.

rotation (MSR) of a set of cells:

$$\langle (\alpha(\sigma, t) - \alpha(\sigma, 0))^2 \rangle_\sigma = 2D_r t,$$

with $\alpha(\sigma, t) - \alpha(\sigma, 0)$ the angular displacement of a cell between time 0 and t. During a simulation, cells may move between clusters, and clusters can merge. Therefore, to calculate D_t and D_r of cells as a function of cluster size, for 100 simulations of 250,000 MCS we measured trajectories of each individual cell with one data point per 500 MCS, and kept track of the size of the cluster it was classified into at each time point. We defined cluster size bins, with the first bin collecting all clusters consisting of two to five cells, and the next bins running from 6 to 10, 11 to 15, *etc*. We split up the trajectories into chunks of 10 consecutive data points, during which the cells stayed within clusters belonging to one bin. To calculate D_t and D_r we performed a least square fitting on the binned MSD and MSR values for these trajectory chunks.

The translational diffusion, D_t, increases slightly with cluster size (Figure 2.3A). This may reflect that the probability of hopping between small clusters will be larger than the probability of hopping between larger clusters, resulting in an overrepresentation of slow cells in the small clusters. Interestingly, the rotational diffusion D_r drops with the cluster size (Figure 2.3B), indicating that cells in large clusters rotate more slowly. These results suggest that the rotation of cells in big clusters is limited, which reduces the probability that two clusters rotate and merge into a single larger cluster. Therefore, if the size of clusters increases, their rotation speeds drop as does the probability of cluster fusion. Thus, although further alignment of clusters would reduce the pattern energy H (Equation 2.2), the pattern evolution essentially freezes.

To corroborate our hypothesis that network patterns are transient patterns that increasingly slowly evolve towards nematic order, we looked for model parameters that could speed up pattern evolution. Figure 2.4A shows the ef-
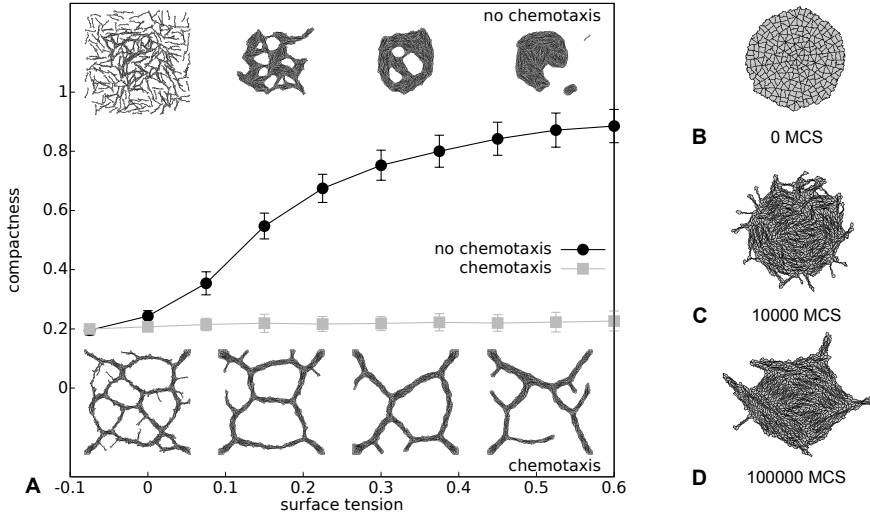
Figure 2.4: A Relation between compactness and surface tension, with and without chemotaxis. The compactness was calculated at 100,000 MCS and averaged over 100 simulations (error bars represent standard deviation). Simulations were initialized with 350 cells on 260x260 path on the center of a 420x420 lattice. **B-D** evolution of a simulation initialized with a 128-cell blob on the center of a 420x420 grid.

fect of surface tension ($\gamma_{cell,ECM}$) on the ability of cells to form networks after 100,000 MCS, as expressed by the configuration's *compactness* $C = \frac{A_{cells}}{A_{hull}}$, where A_{hull} is the area of the convex hull of the largest connected group of cells, and A_{cells} is the summed area of the cells inside the hull. A value of $C \rightarrow 1$ indicates a spheroid of cells, where for networks C would tend to zero. For values of $\gamma_{cell,ECM} = J_{cell,ECM} - \frac{J_{cell,cell}}{2} > 0$, the equilibrium pattern should minimize its surface area with the ECM. Indeed at increased surface tensions the cells settle down in spheroids or networks with only few meshes, although they initially still form network-like patterns (see Supplemental Movie S5, model without chemotaxis and $\gamma_{cell,ECM} = 0.3$). To confirm that also for $\gamma_{cell,ECM} = 0.1$ (*i.e.*, the values used in Figs. 1-3) spheroids are stable configurations, we initialized our model with a spheroid (Figure 2.4**B**). Although initially some cells sprout (Figure 2.4**C**) from the spheroid due to their elongation, they then align gradually and the cell cluster remains spherical. No network formation was detected in simulations of 100,000 MCS (Figure 2.4**D**), suggesting that spheroids represent the global minimum of the Hamiltonian. Interestingly, in presence of chemotaxis networks form for a wide range of surface tensions (inset Figure 2.4**A** and [25]).

2.4 Discussion

Our analysis suggests that in the cellular Potts model elongated, adhesive cells can form networks in a parameter regime where a spheroid pattern is the minimal energy state. The cells initially align with nearby cells, thus forming the branches of the network. In order for the pattern to evolve further towards the minimal-energy spheroid pattern, the locally aligned clusters of cells must join adjacent branches, for which they must move and rotate. Our analysis of the rotational and translational diffusion of cells in Figure 2.3 shows that this becomes more difficult for cells belonging to larger clusters. Thus the networks evolve ever more slowly to the minimal energy state, and gets dynamically arrested in a network-like configuration, a phenomenon reminiscent of the glass transition, as e.g. observed in attractive colloid systems [92], collective cell migration of biological cells *in vitro* [76, 77], and colloid rod suspensions [93] in which gels can form from clusters of parallel rods [94–96].

Figure 2.4A suggests that the cellular Potts simulations undergo a glass transition as the surface tension drops: for high surface tension the system evolves towards equilibrium, for lower surface tensions the system becomes jammed in a network-like state. Thus our model provides a new explanation for the formation of vascular networks in absence of chemical or mechanical, long-range, intercellular attraction [30]. Interestingly, intercellular attraction via chemotaxis stabilizes the formation of networks in our simulations [25] and can drive sprouting from spheroids (not shown). This suggests that networks are an equilibrium pattern of our system in presence of intercellular attraction. Nevertheless the present analysis of arrested dynamics provides new insight into the system with intercellular attraction: chemotaxis reinforces local ordering over a distance proportional to the diffusion length of the chemoattractant producing networks of a scale independent of surface tension [25].

2.A Supplementary movies

An archive containing all supplementary movies can be found at
`http://persistent-identifier.org/?identifier=urn:nbn:nl:ui:18-22535`.

Movie S1 Network formation with elongated cells that chemotact towards a chemoattractant they secrete themselves. This simulation was performed with 700 cells on a 800x800 lattice and ran for 10,000 MCS.

Movie S2 Network formation with elongation cells that do not chemotact. This simulation was performed with 700 cells on a 800x800 lattice and ran for 250,000 MCS.

Movie S3 Evolution of the alignment of elongated cells that chemotact to-

wards a chemoattractant they secrete themselves. This simulation was performed with 175 cells on a 400x400 lattice and ran for 25,000 MCS.

Movie S4 Evolution of the alignment of elongated cells that do not chemotact. This simulation was performed with 175 cells on a 400x400 lattice and ran for 25,000 MCS.

Movie S5 Pattern formation with adhesive, elongated cells, without chemotaxis. This simulations was performed with 175 cells on a 400x400 lattice and ran for 100,000 MCS.

3

Diffusive signaling between endothelial cells and pericytes can cause network collapse and subsequent sprouting

background graphic: network formed with pericytes and endothelial cells interaction via the contact-dependent signaling scenario.

Abstract

Pericytes are perivascular cells that are responsible for the stabilization of small blood vessels. However, in certain *in vivo* systems; such as the mouse retina, central nervous system and tumors; pericytes are observed in developing blood vessels. This suggest that pericytes can also play an active role in angiogenesis. How pericytes and endothelial cells interact during angiogenesis remains unclear. Therefore, we combined *in vitro* vasculogenesis assays with computational modeling to study how pericytes affect endothelial cells and vice versa. With the experiments we can find what patterns endothelial cells and pericytes form together. Then, by varying the interactions between endothelial cells and pericytes included in the model, we can test which interactions could cause *in vitro* patterns.

In the vasculogenesis assay endothelial cells and pericytes initially formed a network. This network quickly collapsed into a blob from which new sprouts extended. In our model we can reproduce the network collapse when endothelial cells attract pericytes and vice versa via chemotaxis. Furthermore, when the chemoattractant for endothelial cells is secreted by endothelial cells adjacent to pericytes instead of pericytes, sprouts extend from the blobs. Thus, our study suggests that during angiogenesis endothelial cells and pericytes attract each other via secreted chemoattractants, and pericytes may regulate the chemoattractant secretion of endothelial cells.

3.1 Introduction
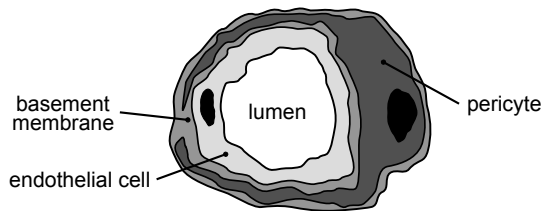
Figure 3.1: Schematic cross section of a small blood vessel.

The walls of small blood vessels, which the are arterioles, capillaries and venules, consist of endothelial cells and pericytes [97] (Figure 3.1). Endothelial cells form the inner layer of the vessel and this layer is covered with the endothelial basement membrane. Embedded in this membrane are the pericytes [98]. Pericytes are recruited to the walls of established blood vessels [99]. This pericyte recruitment is thought to stabilize blood vessels by stimulating the formation of the basement membrane [100] and inhibiting endothelial cell proliferation [101]. Several *in vivo* observations challenge the

view that pericytes are recruited to established vessels where they stabilize the vasculature. In the mouse retina and central nervous system, pericytes are integrated into the developing vessels [69, 70] and in tumor angiogenesis pericytes can lead sprouts [71], suggesting that pericytes interact actively with endothelial cells during blood vessel formation. However, most research focused on the role of pericytes in vessel stabilization and therefore the precise role of pericytes in blood vessel formation remains unclear. To clarify the role of pericytes in blood vessel formation we study how pericytes and endothelial cells interact. For this we combine *in vitro* experiments and computational modeling. By attempting to reproduce the patterns formed *in vitro* with a computational model we can reconstruct which cell behaviors could cause those patterns.

Pericytes and endothelial cells can signal over long distances via diffusive ligands, such as transforming growth factor-β (TGFβ), platelet-derived growth factor B (PDGFB), angiopoietin-1 (Ang-1), and vascular endothelial growth factor (VEGF). Juxtacrine signaling, via membrane-bound ligands and receptors, occurs for example via N-cadherin, and Jagged1 and Notch3 [97, 98, 102]. Endothelial-pericyte signaling regulates the behavior of pericytes and endothelial cells, the differentiation of pericytes and pericyte progenitors, and the maturation and stabilization of blood vessels. Because we are studying how endothelial cells and pericytes interact while forming blood vessels, we only consider the interactions that affect the migration of endothelial cells or pericytes and exclude interactions that only affect pericyte differentiation or vessel stabilization. Both the juxtacrine signaling pathways listed above are involved in vessel maturation and do not affect cell migration. This leaves the four diffusive ligands, which all affect endothelial cell or pericyte migration, as sources of endothelial-pericyte interactions. TGFβ is secreted by both pericytes and endothelial cells [103–105] in a latent form that must be chemically modified to become active [106]. This activation does not occur in pericyte or endothelial cell monocultures, but in endothelial-pericyte cocultures TGFβ is activated via an unknown mechanism [103–105]. In endothelial cells TGFβ regulates cell migration via activin receptor-like kinase (Alk)-1 and Alk-5 [98]. Alk-1 signaling promotes proliferation and migration while Alk-5 signaling inhibits these processes [107–109]. Because of the opposing effects of Alk-1 and Alk-5 signaling, the exact effect of TGFβ signaling on endothelial cell behavior remains unclear. In pericytes TGFβ signaling induces differentiation to vascular smooth muscle cells [110]. PDGFB is secreted by endothelial cells [111, 112] and is sensed by pericytes via PDGF receptor-beta (PDFGRβ) [111]. PDGFB-PDGFRβ signaling induces chemotaxis in pericytes [113] and thereby endothelial cells can attract pericytes. Ang-1 is secreted by pericytes and is sensed by endothelial cells via the receptor TIE2 [98]. This signaling induces chemotaxis in endothelial cells [114] and thereby causes pericytes

to attract endothelial cells. VEGF is sensed by endothelial cells via VEGF receptor 2 (VEGFR2) [115], which induces chemotaxis and promotes endothelial cell survival [116]. VEGF is suggested to play a role in endothelial-pericyte interactions because several studies showed that pericytes cocultured with endothelial cells secrete VEGF [117, 118]. However an alternative mechanism is suggested by Franco *et al.* [119] who showed that endothelial cells in contact with pericytes secrete VEGF. Franco *et al.* [119] proposed that VEGF secretion by endothelial cells is induced by the activation of membrane bound integrin α_V on endothelial cells by vitronectin that is secreted by pericytes. Thus, VEGF signaling attracts endothelial cells to pericytes, or to endothelial cells that are close to pericytes. Altogether, except for TGFβ, all diffusive ligands involved in endothelial-pericyte signaling induce chemotaxis in pericytes or endothelial cells.

Overall, based on the literature we propose that attraction via diffusive, secreted, ligands is a major mode of endothelial-pericyte interaction. Endothelial cells are known to secrete chemoattractants that attract pericytes, such as PDGFB, and pericytes secrete chemoattractants for endothelial cells, such as VEGF, Ang-1, and TGFβ. VEGF may be secreted by endothelial cells, in close vicinity of pericytes, instead of by pericytes. Thus, exactly via which chemoattractants pericyte and endothelial cells interact, and which cells secrete which chemoattractant remains unclear. Therefore, in this study we will use a computational model to find if attraction via chemotaxis between pericytes and endothelial cells plays a role during angiogenesis, and if so, which chemoattractant should be secreted by which cells. For this we first study pattern formation of endothelial cells and pericytes with vasculogenesis assays. Then, we try to reproduce these patterns with our computational, cell-based model. In such a model we can study how changes in cell behavior, such as chemotaxis and chemoattractant secretion, and the chemical properties of chemoattractants affect pattern formation. Thus, with our model we can search for the chemotaxis scenario that could cause the *in vitro* patterning.

3.2 Results

To study how endothelial cells and pericytes interact during blood vessel formation we used *in vitro* experiments in combination with computational models. For the *in vitro* experiments we used a standard vasculogenesis assay [45] in which cells are seeded on a substrate and the evolution of the pattern is monitored over time. We performed assays with only endothelial cells, only pericytes, or both pericytes and endothelial cells. Based on the results of the endothelial cells and pericytes monocultures we built a computational, cell-based model of endothelial cells and pericytes using the cellular Potts method and partial differential equations. The behavior of individual peri-

cytes and endothelial cells is chosen such that simulations with a single cell type correspond with the corresponding *in vitro* monocultures. Then, we used the model to study which endothelial-pericyte interactions may contribute to the patterns we observed in the *in vitro* endothelial-pericyte coculture. For this we assumed that endothelial cells and pericytes interact by secreting chemoattractants. For simplicity, we refer to the chemoattractant that endothelial cells secrete for pericytes as PDGFB, and we refer to the chemoattractant that pericytes secrete for endothelial cells as VEGF. However, these chemoattractants represent generic chemoattractants and therefore we did not use PDGFB and VEGF specific model parameters. For VEGF, it is debated whether it is secreted by pericytes [117, 118], or by endothelial cells that contact pericytes [119]. With a computational model we can simulate the tissues that develop based on each of these scenarios. For this, we set up two scenarios for endothelial-pericyte signaling: *paracrine signaling*, and *contact-dependent signaling*. In the paracrine signaling scenario, endothelial cells secrete a chemoattractant for pericytes and vice versa (Figure 3.2A). In the contact-dependent signaling scenario, we assumed that contact with pericytes induces VEGF secretion in endothelial cells [119]. Therefore, in this scenario PDGFB is secreted by all endothelial cells and VEGF is secreted by endothelial cells that are in contact with pericytes (Figure 3.2B).
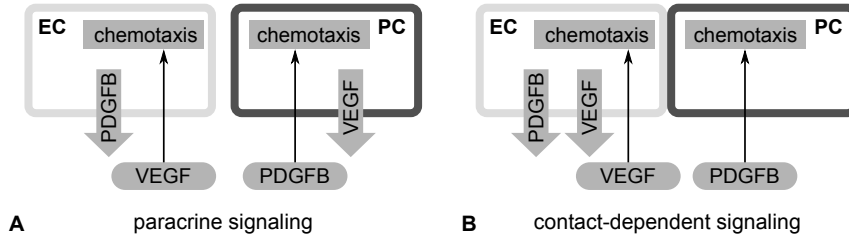
Figure 3.2: Alternative scenarios for endothelial-pericyte signaling.

3.2.1 *In vitro* patterning

We started with the *in vitro* experiments to elucidate what patterns form when endothelial cells and pericytes are seeded together. For this we seeded endothelial cells and pericytes, at a 2:1 ratio, and followed the pattern evolution. As a reference, we repeated the experiments with only endothelial cells, or only pericytes.

Figure 3.3 shows how the patterns evolved in each of the three assays. In the endothelial cell monoculture (Figure 3.3A) a network with long branches formed quickly. Between the second and eighth day the network disintegrated because the endothelial cells died. In the pericyte monoculture (Figure 3.3B)
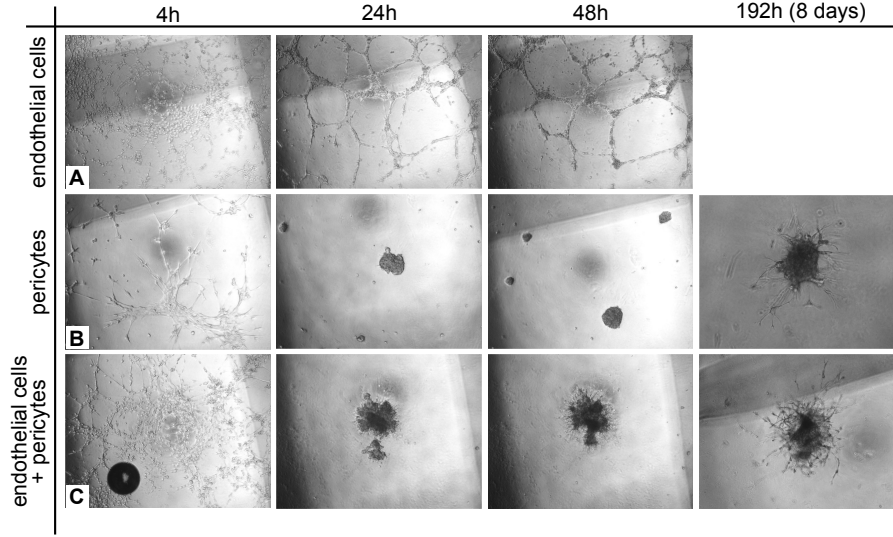
Figure 3.3: Pattern formation in vasculogenesis assays with endothelial cells (**A**), pericytes (**B**), or endothelial cells and pericytes at a ratio of 2:1 (**C**).

initially some branched structures formed that quickly collapsed into a blob. After eight days some sprouts extended from this blob. In the endothelial-pericyte coculture (Figure 3.3**C**) a network developed quickly. Within 24 hours, the network collapsed into a blob and later on sprouts extended from the blob. Comparing the evolution of a blob with only pericytes (Figure 3.3**B**) with that of a blob with pericytes and endothelial cells (Figure 3.3**C**) suggests that endothelial cells caused the sprouts to extend earlier and become longer. However, we currently lack quantitative data to support this conclusion.

Altogether, in all cultures networks formed quickly. However, when pericytes are present, the network collapsed to form a blob. Over time, sprouts extended from this blob, which seemed to be more numerous in the endothelial-pericyte coculture. These observations indicate that pericytes induce network collapse, and that endothelial cells may promote sprout formation from the cell blobs.

3.2.2 Modeling endothelial cells and pericytes

In our attempt to explain what endothelial-pericyte interactions cause the patterns observed in the *in vitro* coculture, we set out to develop a computational, cell-based model of endothelial-pericyte interactions. In this model we use the cellular Potts method (CPM) to model cells and partial differential equations (PDEs) to model chemoattractants. Cells are represented as groups of lattice sites $\vec{x} \in \mathbb{Z}^2$ on a square lattice identified by an identifier

$\sigma \in \mathbb{N}$. Each cell is associated with a type $\tau(\sigma) \in \{EC,PC,ECM\}$. To mimic cell motion the CPM iteratively attempts to move the cell membranes. Whether an attempt is accepted depends on the cell motility μ and the prescribed cell behaviors. The chemoattractant concentrations are projected on the same lattice as the cells. The concentration of a chemoattractant c at a site $\vec{x}$ is described with a PDE:

$$\frac{\partial c(\vec{x}, t)}{\partial t} = D(c)\nabla^2 c(\vec{x}, t) + \alpha(\tau(\sigma(\vec{x})), c) - \varepsilon(c);$$

with $c(\vec{x}, t)$ the concentration of c, $D(c)$ the diffusion coefficient of c, $\alpha(\tau, c)$ the secretion rate of c by a cell of type τ, and $\varepsilon(c)$ the decay rate of c. The range over which a chemoattractant has spread in steady state ($\frac{\partial c(\vec{x},t)}{\partial t} = 0$) is characterized by the diffusion length: $\ell = \sqrt{\frac{D}{\varepsilon}}$, which is the distance from the chemoattractant source, where $c(\vec{x}, t) = c_0$, at which the concentration has dropped to $\frac{c_0}{e}$. Note that, however, when a time step of the CPM is shorter than time needed for c to reach equilibrium, the chemoattractant will not diffuse as far as predicted.
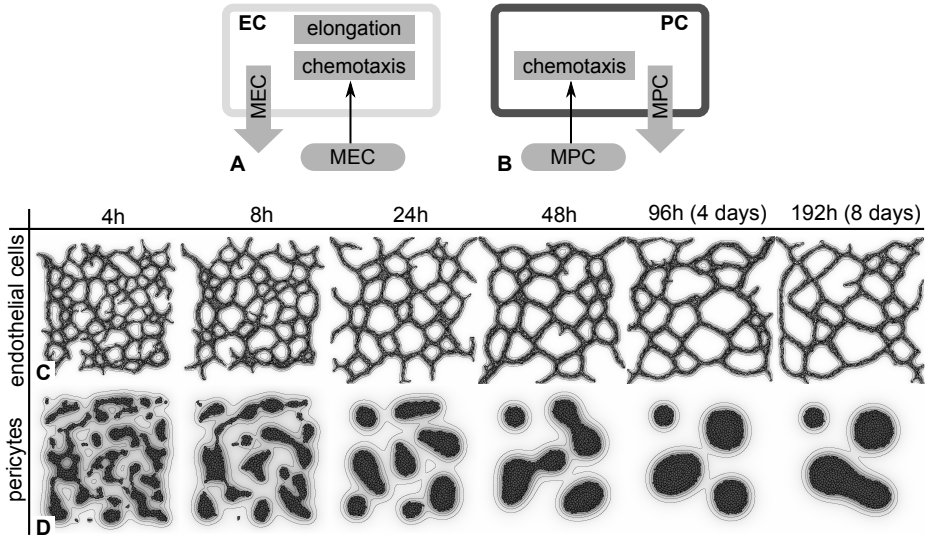
Figure 3.4: Models for endothelial cell and pericyte monocultures. **A** endothelial cells (ECs) elongate and secrete MEC that induces chemotaxis in endothelial cells. **B** pericytes (PCs) secrete MPC that induces chemotaxis in pericytes. **C-D** evolution of the pattern formed with 600 endothelial cells (**C**) or 600 pericytes (**D**).

The cell behaviors in the endothelial-pericyte model were prescribed such that a simulation with only pericytes or only endothelial cells results in a pattern similar to the pattern formed in the corresponding *in vitro* monocul-

ture. In the monoculture endothelial cells form networks with long branches. These networks are similar to the networks formed in a model with elongated cells that secrete their own chemoattractant [25]. Therefore, we modeled endothelial cells as elongated cells that secrete and chemotact towards a chemoattractant that we called "morphogen for endothelial cells" (MEC) (Figure 3.4**A**). Pericytes formed a network that quickly collapsed into a blob. This is similar to the evolution of a model with round cells that secrete their own chemoattractant [26, 28]. Thus, pericytes were modeled as round cells that secrete and chemotact towards a chemoattractant called "morphogen for pericyte" (MPC) (Figure 3.4**B**). For both endothelial cells and pericytes we fine-tuned the model parameters such that the pattern evolution was as close to the *in vitro* experiments as possible (Table 3.2), starting with the parameter values used in similar models [25, 28]. Figures 3.4**C** and **D**, and Movies S1 and S2, show the evolution of patterns formed by respectively endothelial cells and pericytes. The evolution of the pattern with endothelial cells is similar to the *in vitro* pattern evolution. The simulated pericytes initially form a network-like structure that collapses into multiple small blobs (Figure 3.4**D**). In the vasculogenesis assay a network formed and collapsed as well, but here a single blob formed (Figure 3.3**C**). Thus, our model does not exactly mimic the *in vitro* pattern formation, but it reproduces the phenomenology of the pericyte monocultures (Figure 3.3**C**).

  endothelial-pericyte signaling is incorporated in the model by adding the chemoattractants VEGF and PDFGB. For *paracrine signaling* scenario PDGFB by all endothelial cells, and VEGF is secreted by all pericytes. For the *contact-dependent signaling* scenario PDGFB is again by all endothelial cells. But, VEGF is only secreted by endothelial cells that contact pericytes. An endothelial cell contacts a pericyte when it shares at least 10% of its membrane with pericytes. We set this, arbitrary, to prevent a few pseudopod extensions from inducing VEGF secretion.

chemo-attractant	sensitivity	secretion rate [s^{-1}]	decay rate [s^{-1}]	diffusion coefficient [$m^2 s^{-1}$]
MEC	500	10^{-2}	10^{-3}	10^{-13}
MPC	500	10^{-3}	10^{-4}	10^{-13}
VEGF	500	10^{-3}	10^{-3}	10^{-13}
PDGFB	500	10^{-3}	10^{-3}	10^{-13}

Table 3.1: Parameters related to the chemoattractants.

3.2.3 The *in vitro* patterns cannot be reproduced without endothelial-pericyte signaling
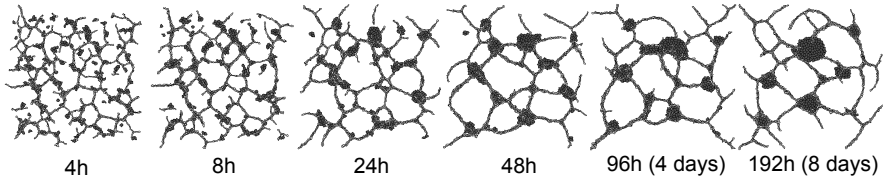
Figure 3.5: Evolution of a simulation with 400 endothelial cells (light) and 200 pericytes (dark).

Before we tested the endothelial-pericyte signaling scenarios, we first tested if any of these interactions are needed to reproduce the patterns that formed *in vitro*. Therefore, we simulated a mixture of elongated endothelial cells and round pericytes at a 2:1 ratio, which is the same ratio as used in the endothelial-pericyte cocultures. Figure 3.5 and Movie S3 show how the morphology of this mixture evolved. The first 8 hours a network develops similar to endothelial-pericyte coculture. But, after one day pericytes clustered at the branch points. This clustering continued, resulting in couple of branch points with large pericyte clusters. Thus, without signaling between endothelial cells and pericytes, a network formed quickly, but the network did not collapse as did happen in the cocultures. This suggests that additional endothelial-pericyte interactions are needed to induce a network collapse.

3.2.4 Heterotypic, chemotactic endothelial-pericyte attraction can cause network collapse
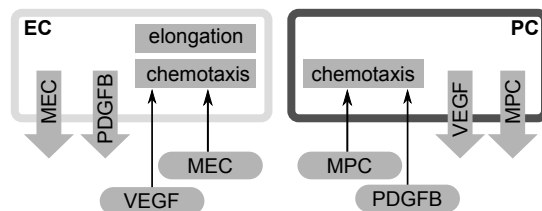
Figure 3.6: Schematic representation of paracrine signaling between pericytes (PC) and endothelial cells (EC). Pericytes secrete VEGF that attracts endothelial cells and endothelial cells secrete PDGFB that attracts pericytes.

In the previous section we combined elongated endothelial cells and round pericytes in one model without endothelial-pericyte signaling. With this model we could reproduce the network formation, but not the network collapse that

occurred in the *in vitro* coculture. This suggests that an additional mechanism is necessary for network collapse. Therefore, we added attraction between endothelial cells and pericytes via chemotaxis to the model. In this section we test the paracrine endothelial-pericyte signaling scenario. In this scenario endothelial cells secrete PDGFB, attracts pericytes, and pericytes secrete VEGF, which attract endothelial cells (Figure 3.6). How the chemoattractants affect pattern formation with endothelial cells and pericytes depends on the secretion rate and the strength of the chemotactic sensitivity of the cells, and the diffusive properties of the chemoattractants. Because VEGF and PDGFB represent generic chemoattractants that attract endothelial cells or pericytes, the values of these parameter are unknown. Therefore, we varied the values of these parameters in our model to elucidate what patterns can form.

First, we explored how the secretion rates of VEGF and PDGFB, and the diffusive properties of VEGF and PDGFB affect pattern formation of endothelial cells and pericytes. To this end we varied secretion and decay rates of VEGF relative to those for PDGFB. All other chemoattractant parameters remained unchanged and are listed in Table 3.1. By keeping the diffusion coefficients constant while varying the decay rate we aim to vary the diffusion length. However, this is only correct when the PDEs describing the concentrations are solved until equilibrium during one time step. We choose the ranges of relative secretion and decay rates such that the PDE solver produced a stable solution and no other modeling artifacts were observed. Figure 3.7**A**-**P** shows the morphologies that formed for varying ratios of secretion and decay. In this figure we recognized three patterns: 1) a network with blobs of pericytes at the nodes (Figure 3.7**A**, **B**, **E**-**G**, **I**-**K**, and **M**-**P**), 2) a nearly collapsed network (Figure 3.7**C**), and 3) cells at the lattice borders (Figure 3.7**D**, **H**, and **L**). The first pattern is similar to the patterns formed without PDGFB or VEGF. Thus, for those secretion and decay rates, PDGFB and VEGF have little effect. The second pattern shares some features with our *in vitro* observations. The cells do aggregate, but the network never fully collapsed (Figure 3.7**Q** and Movie S4). The third pattern does not represent realistic pattern formation. For these simulations the high VEGF secretion of pericytes causes endothelial cells to be more attracted to the pericytes than to other endothelial cells. Therefore, branches of aligned endothelial cells do not become stable, but endothelial cells leave the branch and migrate outwards together with the pericytes. Eventually, most of the cells become stuck at the border of the lattice.

Next, we explored the effects of the chemotactic sensitivity of pericytes to PDGFB and endothelial cells to VEGF. For this we choose a decay and secretion rate for VEGF such that the network collapsed, which are the parameter values used for Figure 3.7**C** ($\varepsilon(\text{VEGF}) = 10^{-5}\text{s}^{-1}$ and a $\alpha(\text{VEGF}) = 10^{-3}\text{s}^{-1}$). The
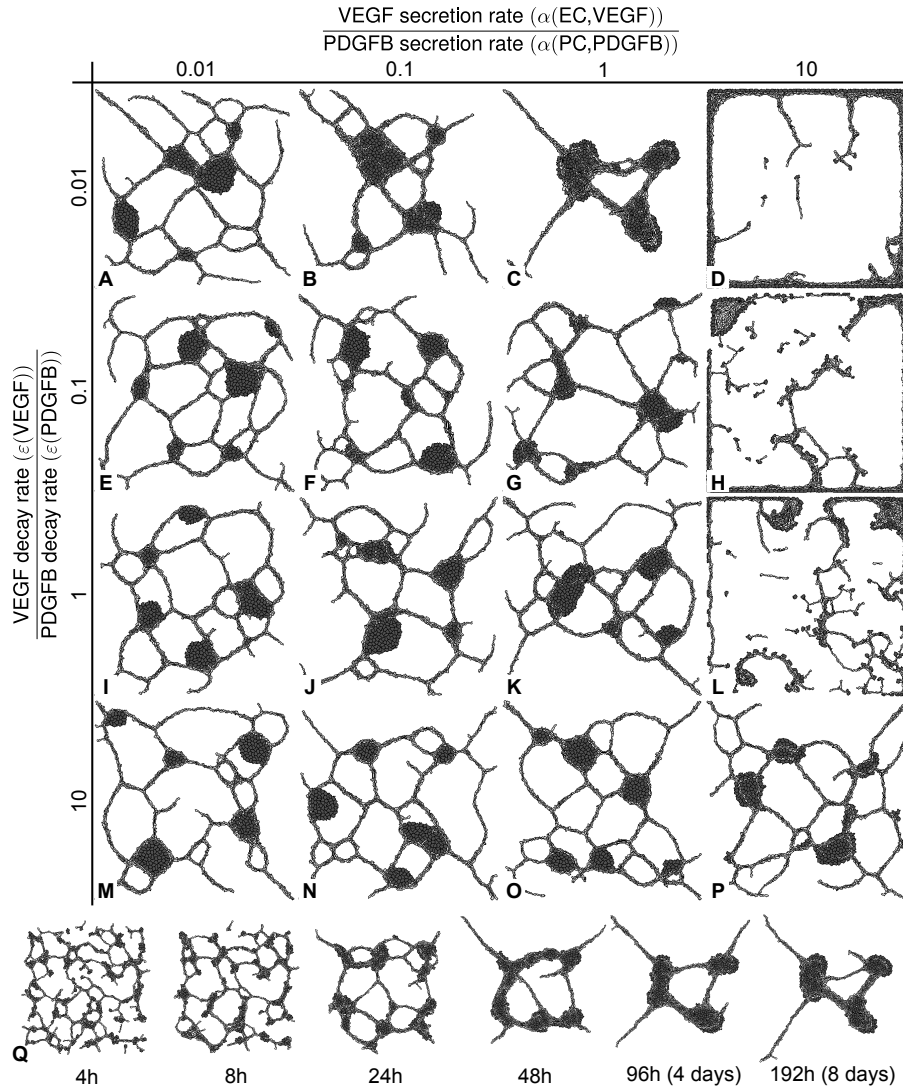
Figure 3.7: A-P Patterns formed after ∼192 hours with round pericytes (dark gray) and long endothelial cells (light gray) with varying ratios of PDGFB and VEGF secretion, and varying ratios of PDGFB and VEGF decay. Endothelial cells are attracted to VEGF that is secreted by pericytes and pericytes are attracted to PDGFB that is secreted by endothelial cells (Figure 3.6). **Q** Evolution of pattern in **C**.

range of chemotactic sensitivity was chosen such that chemotaxis affect the patterns, *i.e.* the morphologies differ from those without endothelial-pericyte signaling, and such that there are no model artifacts. Figure 3.8 shows how the final patterns formed with varying chemotactic sensitivity for PDGFB and VEGF. In this morphospace we see two different kinds of blobs: 1) blobs with pericytes on the inside and sprouting endothelial cells on the outside, and 2) blobs with endothelial cells on the inside and pericytes on the outside. The first kind of blobs are stationary, while the second kind of blobs move towards the pericytes. This happens because the chemotaxis of endothelial cells towards VEGF pushes the pericytes ahead. As a result, the cell blobs migrate to the lattice borders where they get stuck.

Altogether, we found that attraction between pericytes and endothelial cells via chemotaxis can affect the patterns these cells form. When VEGF and PDGFB are secreted at the same rate and VEGF diffuses much further than PDGFB, networks formed that collapsed into a blob with long sprouts. Varying the chemotactic sensitivity to VEGF and PDGFB did not improve this collapse. Overall, with the paracrine signaling scenario we partially reproduced the network collapse observed in the *in vitro* cocultures.

3.2.5 Endothelial cell chemotaxis towards endothelial secreted VEGF enables sprouting after network collapse

We showed that PDGFB secretion by endothelial cells and VEGF secretion by pericyte can cause partial network collapse. However, the network did not collapse completely and no new sprouts were formed, which was observed in the endothelial-pericyte cocultures. Therefore, we tested if the second signaling scenario, contact-dependent signaling, could improve network collapse and enable sprouting. In this scenario endothelial cells can secrete both VEGF, which attracts endothelial cells, and PDGFB, which attracts pericytes. PDGFB is secreted by all endothelial cells, similar to the paracrine signaling scenario. VEGF is only secreted by endothelial cells that are adjacent to pericytes (Figure 3.9). As in the previous section, we tested how the chemoattractant secretion rate and diffusive properties, and the cells' sensitivity to the chemoattractant affects the patterns that the cells form.

First, we tested how the relative decay and secretion rates of VEGF and PDGFB affected pattern formation. The ranges of relative decay and secretion rates were chosen such that there were no modeling artifacts, and such that all observed patterns were included. Figure 3.10**A**-**P** shows the patterns that formed with juxtacrine endothelial-pericyte signaling. For almost all tested secretion and decay rates networks formed with a few groups of pericytes on the networks nodes (Figure 3.10**A** and **B**, and **E**-**P**). A single pericyte cluster evolved for only one parameter setting (Figure 3.10**C** and **Q**, and Movie S5). For one other parameter setting the initial network collapsed into a few
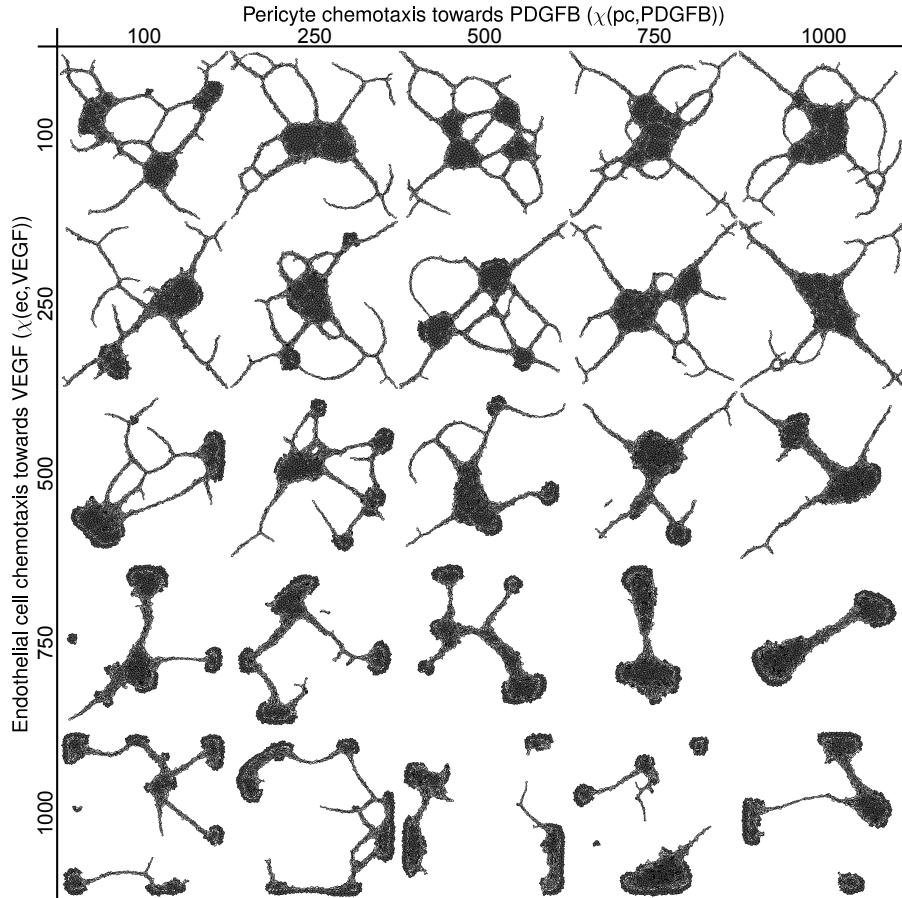
Figure 3.8: Patterns formed after ∼192 hours with 200 round pericytes (dark) and 400 long endothelial cells (light) with varying chemotaxis strengths for pericytes towards PDGFB and endothelial cells towards VEGF after ∼192 hours. Endothelial cells are attracted to VEGF that is secreted by pericytes and pericytes are attracted to PDGFB that is secreted by endothelial cells (Figure 3.6).
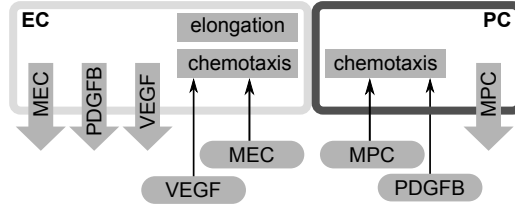
Figure 3.9: Schematic representation of contact-dependent signaling between pericytes (dark) and endothelial cells (light). Endothelial cells secrete PDGFB that attracts pericytes, and endothelial cells that are in contact with pericytes secrete VEGF that attracts endothelial cells.

blobs that later connected via long, thick branches of endothelial cells (Figure 3.10**D** and **R**, and Movie S6). Thus, compared with the paracrine signaling scenario, the contact-dependent signaling scenario did not seem to improve network collapse.

Next, we studied the effects of varying the chemotactic sensitivity of endothelial cells to VEGF and pericytes to PDGFB to test if and how this affects the formed patterns. For this we use a VEGF secretion rate of 10^{-3}s^{-1} and VEGF decay rate of 10^{-5}s^{-1} because for those settings the network partially collapsed (Figure 3.10**C**). Figure 3.11 shows the patterns that evolved after eight days for varying chemotactic sensitivity towards VEGF and PDGFB. While varying the PDGFB sensitivity of pericytes has little effect on the final morphologies, varying the VEGF sensitivity of endothelial cells had a prominent effect. For a low VEGF sensitivity, a few clusters of pericytes formed inside the network. For higher VEGF sensitivity, a single pericyte cluster formed, from which long branches extended. Interestingly, not all of these branches were part of the initial network. In some simulations new sprouts of endothelial cells extended from the blob (see Figure 3.12 and Movie S7).

Overall, as with the paracrine signaling scenario, for the contact-dependent signaling scenario a blob formed when VEGF had a large diffusion length and was secreted at the same rate as PDGFB. In contrast to the paracrine signaling scenario, here network collapse improved with a higher VEGF chemotaxis. Furthermore, with a higher VEGF chemotaxis new sprouts extended from the collapsed networks. Thus, with the contact-dependent signaling scenario the model reproduced the phenomenology of the endothelial-pericyte cocultures: network collapse and sprout formation.

3.3 Discussion

In this work we studied how pericytes may be involved in angiogenesis using *in vitro* experiments and computational modeling. By including hypothesized
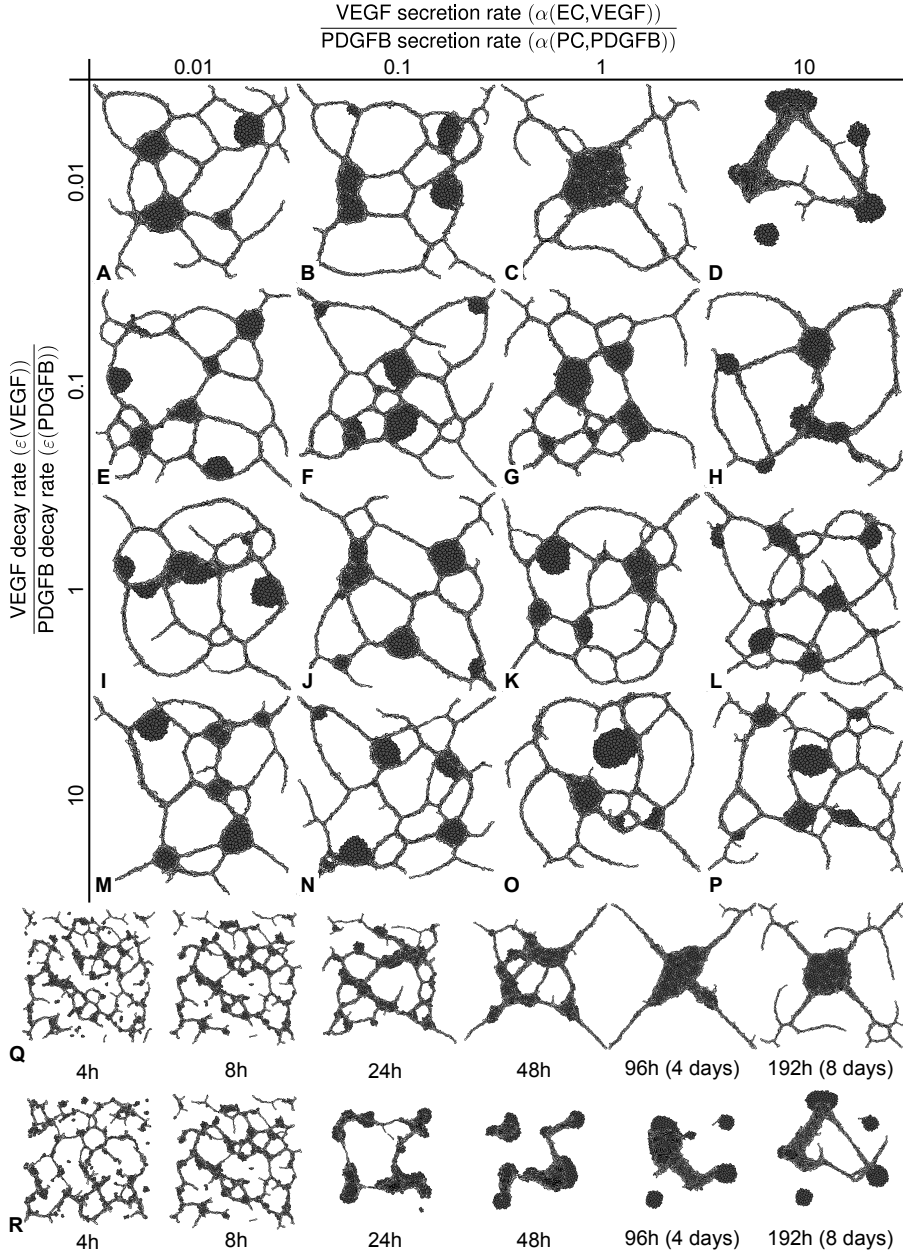
Figure 3.10: A-P Patterns formed after ∼192 hours with 200 round pericytes (dark) and 400 long endothelial cells (light) with varying ratios of PDGFB and VEGF secretion, and varying ratios of PDGFB and VEGF decay. Endothelial cells are attracted to VEGF that they secrete when they are in contact with pericytes and pericytes are attracted to PDGFB that is secreted by endothelial cells (Figure 3.9). **Q** evolution of the pattern in **C. R** evolution of the pattern in **D.**
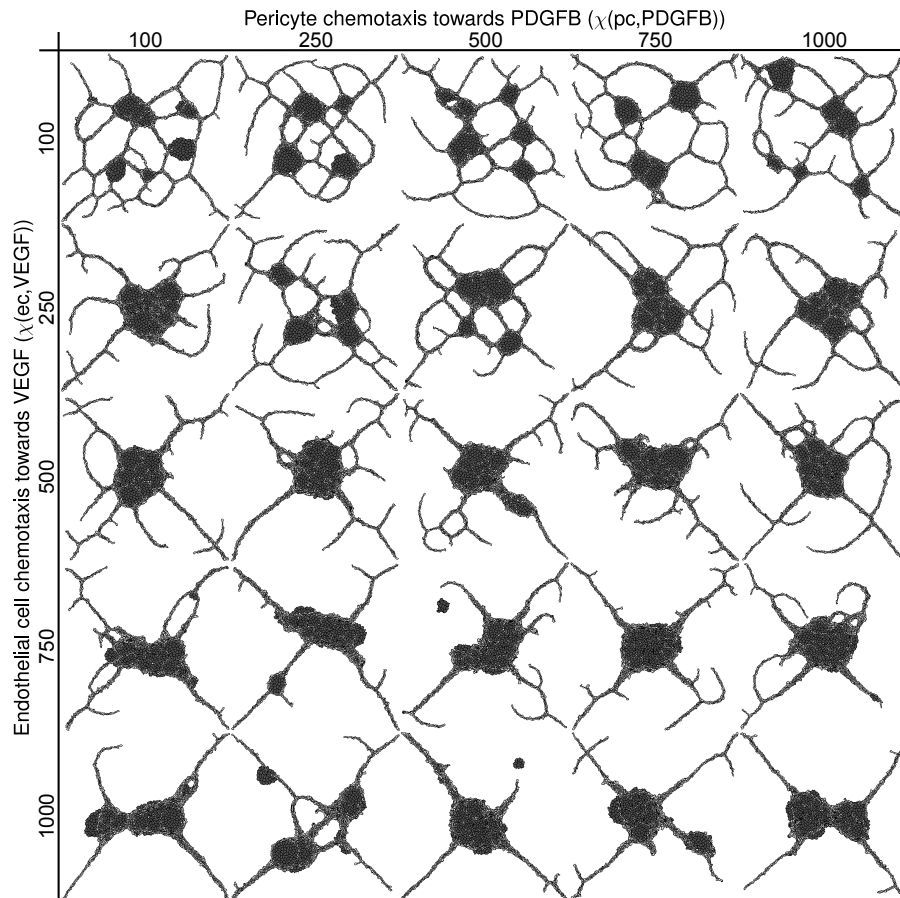
Figure 3.11: Patterns formed after ∼192 hours with 200 round pericytes (dark) and 400 long endothelial cells (light) with varying chemotaxis strengths for pericytes towards PDGFB and endothelial cells towards VEGF. Endothelial cells are attracted to VEGF that they secrete when they are in contact with pericytes and pericytes are attracted to PDGFB that is secreted by endothelial cells (Figure 3.9).

165 hours   +100 minutes   +200 minutes   +300 minutes   +400 minutes   +600 minutes
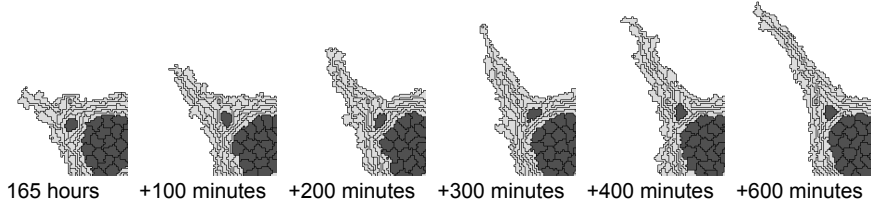
Figure 3.12: New sprout extending from a blob when VEGF is secreted by endothelial cells that are in contact with pericytes. The snapshots were obtained from a simulation with α(EC,VEGF) $= 10^{-3}$), ε(VEGF) $= 10^{-5}$, χ(EC,VEGF) $= 750$, and χ(PC,PDGFB) $= 500$) that ran with 400 endothelial cells and 200 pericytes.

endothelial-pericyte interactions in a computational, cell-based model of angiogenesis we tested which interactions could cause the patterns formed *in vitro*. The experiments showed that pericytes induce a collapse of the network formed by endothelial cells, and endothelial cells induce sprouting in a endothelial-pericyte blob. Based on endothelial-pericyte interactions described in the literature we proposed that endothelial cells and pericytes interact via chemoattractants. With the model we tested two scenarios of endothelial-pericyte signaling: paracrine signaling, and contact-dependent signaling. In the paracrine signaling scenario endothelial cells secreted a chemoattractant for pericytes and vice versa. With this scenario the model reproduced network collapse, but not sprouting. In the contact-dependent signaling scenario endothelial cells secreted a chemoattractant for pericytes, and when endothelial cells are in contact with pericytes they also secrete a chemoattractant for themselves. With this scenario the model reproduced both network collapse and sprouting. Thus, our model supports the hypothesis that endothelial cells and pericytes interact during angiogenesis by secreting chemoattractants. Furthermore, our model indicates that sprouting after network collapse could be the result of pericyte induced secretion of a endothelial cell chemoattractant by endothelial cells. This fits with the observation by Franco *et al.* [119] that endothelial cells secreted the endothelial cell chemoattractant VEGF when they are in contact with pericytes.

In the model we incorporated generic chemoattractants because there exist multiple candidates for each chemoattractant, including VEGF, PDGFB, TGFβ, and Ang-1. By varying the chemical properties of the chemoattractants, the source and rate of chemoattractant production, and the response of cells to the chemoattractants we characterized the cell behavior and chemoattractant properties needed to reproduce the patterns formed *in vitro*. We found that the endothelial cell chemoattractant should diffuse further than the chemoattractant for pericytes. Furthermore, a strong response of en-

dothelial cells to their chemoattractant improves network collapse. To link these properties to a chemoattractant we need experimental data such a diffusion length and the relative strength of chemotaxis. However, this information is scarce and not available for all the chemoattractants we discussed in the introduction. Therefore, we cannot directly link our model predictions to specific chemoattractants.

Our modeling study indicates that the patterns endothelial cells and pericytes form *in vitro* are the result of chemoattractants secreted by endothelial cells and/or pericytes. This hypothesis should be validated experimentally. Because we do not know the identity of the chemoattractants, we cannot use genetic knockouts, trap the chemoattractants, or block the receptors. Instead, we can use two alternative approaches. First, we can test if chemical gradients do indeed play a role in pattern formation. This can be tested by removing the gradients from the culture, for example by constantly tilting the cultures an by seeding the cells on a substrate to which chemoattractants cannot bind. If pattern formation remains unchanged in such cultures, chemotaxis cannot have caused the patterns. Second, we can compare if the distribution of pericytes and endothelial cells predicted by our model matches with *in vitro* observations. In our model, pericytes form the center of the blob, and endothelial cells form the outer layer and sprouts. By labeling endothelial cells and pericytes with different colors, or even by staining the cultures, the distribution of endothelial cell and pericytes can be compared to the model predictions. A difference between the distribution of cells *in vitro* and in the model indicates that the model contains incorrect assumptions, or misses vital cell behavior.

Because we could not completely reproduce the experimental observations, it is likely that the model is missing essential cell behaviors or endothelial-pericyte interactions. In our model we did not account for proliferation, apoptosis and differentiation, which are, among others, regulated by TGFβ and VEGF. TGFβ affects proliferation and differentiation in both pericytes and endothelial cells [98]. However, opposing effects are ascribed to the two TGFβ receptors Alk-1 and Alk-5. Therefore, TGFβ signaling should be understood at the single cell level before it can be added to a cell-based model. VEGF induces proliferation and inhibits apoptosis in endothelial cells [120]. If pericytes are indeed necessary for the production of VEGF, this would explain why the endothelial cells in the monoculture died. Incorporating VEGF regulation of proliferation and apoptosis in the model could result in apoptosis of endothelial cells in sprouts without pericytes and proliferation in the cell blob. Another aspect that may not be represented with sufficient detail is the shape of pericytes. In the model pericytes are modeled as round cells, while in reality pericytes have long extensions via which they contact multiple endothelial cells. Because these extension allow pericytes to interact with mul-

tiple endothelial cells and sense chemoattractants much further away from the cell body, they could play an important role in the model.

3.4 Methods

3.4.1 *In vitro* vasculogenesis assay

Pattern formation of endothelial cells and pericytes was analyzed with *in vitro* vasculogenesis assays with immortalized human umbilical vein endothelial cells (ECRF) and/or human brain vascular pericytes (HBVP). The HBVP were obtained form CellSystems (Troisdorf, Germany) and the ECRF were provided by Ruud Fontein (Academic Medical Center, Amsterdam). Suspensions of ECRF, HBVP, or ECRF and HBVP at a 2:1 ratio were seeded on Matrigel and endothelial growth media (EGM), obtained from Lonza (Breda, The Netherlands), was added. The assays were incubated at 37 °C for eight days (192 hours). At 4, 24, 48 and 192 hours images of the assays were obtained using phase contrast microscopy.

3.4.2 Cellular Potts model

The cellular Potts model (CPM) [84, 85] represents cells on a regular lattice. Each lattice site $\vec{x} \in \mathbb{Z}^2$ is associated with an index $\sigma \in \mathbb{N}$. Cells are sets of lattice sites with the same $\sigma > 0$ and the remaining lattice sites, with $\sigma = 0$, represent the extracellular matrix (ECM). Cell movement and deformation is modeled by attempts to copy the index of a randomly chosen lattice site $\vec{x}$ to one of its eight nearest neighbors $\vec{x}'$. Whether a copy attempt is accepted depends on the change in the *effective energy* (ΔH) that is associated with the copy:

$$p_{\text{accept}}(\Delta H) = \begin{cases} 1 & \text{when } \Delta H \leq 0; \\ e^{-\frac{\Delta H}{\mu}} & \text{when } \Delta H > 0; \end{cases}$$

where μ denotes the cell motility. During one time step of the CPM, called a Monte Carlo step (MCS), as many of copies are attempted as there are lattice sites.

The effective energy depends on the cell behavior that is prescribed in the model. This cell behavior is prescribed for each modeled cell type, which is identified by $\tau(\sigma) \in \{\text{ECM,EC,PC}\}$. In the standard CPM, the effective energy includes cell adhesion and area conservation:

$$H = \underbrace{\sum_{(\vec{x},\vec{x}')} J(\tau,\tau')(1 - \delta(\sigma,\sigma'))}_{\text{cell adhesion}} + \underbrace{\sum_{\sigma} \lambda_A(\tau)\left(a(\sigma) - A(\tau)\right)^2}_{\text{area conservation}}.$$

Cell adhesion depends on the cost $J(\tau,\tau')$ of an interface (x, x') between types τ and τ', with $\sigma = \sigma(\vec{x})$, $\tau = \tau(\sigma(\vec{x}))$, $\sigma' = \sigma(\vec{x}')$ and $\tau' = \tau(\sigma(\vec{x}'))$.

Area conservation is modeled by comparing the actual area $a(\sigma)$ with the target area of that cell $A(\tau(\sigma))$. How much the actual cell area fluctuates around the target area depends on the elasticity parameter $\lambda(\tau)$.

Extra cell behaviors are added by extending the *effective energy* function. For the endothelial-pericyte model we added cell elongation and chemotaxis. To model cell elongation we added a term similar to the area conservation with a target length $l(\sigma)$ an elongation strength $\lambda_L(\tau)$ [25]:

$$H_{\text{elongation}} = \sum_{\sigma} \lambda_L(\tau) \left(l(\sigma) - L(\tau) \right)^2 .$$

The cell length is estimated based on the largest eigenvalue $\lambda_b(\sigma)$ of the cell's inertia tensor: $l(\sigma) = 4\sqrt{\frac{\lambda_b(\sigma)}{a(\sigma)}}$ [121]. To model chemotaxis towards a chemoattractant c we added an extra term to the energy change associated with a copy from $\vec{x}$ to $\vec{x}'$ [90]:

$$\Delta H_{\text{chemotaxis}}(c) = -\max(\chi(\tau, c), \chi(\tau', c)) \left(c(\vec{x}') - c(\vec{x}) \right),$$

with $\chi(\tau, c)$ the chemotactic sensitivity of a cell of type τ and chemoattractant c. Because in the model each chemoattractant induces chemotaxis in one cell type, $\max(\chi(\tau, c), \chi(\tau', c))$ is identical to the chemotactic sensitivity of the cell type that responds to c. The concentration of the chemoattractant c is described as:

$$\frac{\partial c(\vec{x}, t)}{\partial t} = D(c)\nabla^2 c(\vec{x}, t) + \alpha(\tau(\sigma(\vec{x})), c) - \varepsilon(c),$$

with $D(c)$ diffusion coefficient of chemical c, $\alpha(\tau(\sigma(\vec{x})), c)$ the secretion rate of c by the cell at $\vec{x}$, $\varepsilon(c)$ the decay rate of c.

All simulations presented in this work were performed on a 400 by 400 pixel lattice, which corresponds with an area of 800 μm by 800 μm. At the start of the simulation 600 cells are randomly distributed on this lattice. For each cell type the CPM parameters as listed in table 3.2 are assigned, which our based on previous work with similar models [25, 28]. Furthermore, all chemoattractant fields are initialized at zero. During the simulation the PDEs describing the fields (Equation 3.4.2) are solved with a forward Euler solver with zero boundaries. The solver runs every MCS with 15 time steps of 2 seconds, thus an MCS corresponds to 30 seconds. To match the duration of the vasculogenesis assays, which is eight days, the simulations must run for 25 000 MCS.

Symbol	Description	Value
J(EC,PC), J(EC,EC), J(PC,PC)	cell-cell adhesion	40
J(EC,ECM), J(PC,ECM)	cell-ECM adhesion	20
A(EC), A(PC)	target area	200 μm^2
λ_A(EC), λ_A(PC)	elasticity parameter	25
L(EC)	target length	60 μm
λ_L(EC)	elongation strength	10
μ(EC), μ(PC)	cell motility	50
χ(EC,MEC), χ(PC,MPC)	chemotaxis	500
χ(EC,VEGF), χ(PC,PDGFB)	chemotaxis	500

Table 3.2: Model parameters describing the behavior of endothelial cells and pericytes.

3.A Supplementary movies

An archive containing all supplementary movies can be found at
`http://persistent-identifier.org/?identifier=urn:nbn:nl:ui:18-22536`

Movie S1 Evolution of a simulation with 600 endothelial cells (light) and no pericytes (Figure 3.4**C**).

Movie S2 Evolution of a simulation with 600 pericytes (dark) and no endothelial cells (Figure 3.4**D**).

Movie S3 Evolution of a simulation with 400 endothelial cells (light) and 200 pericytes (dark) (Figure 3.5).

Movie S4 Evolution of a simulation with paracrine signaling and a low VEGF decay rate (Figure 3.7**C**).

Movie S5 Evolution of a simulation with contact-dependent signaling and a low VEGF decay rate (Figure 3.10**C**).

Movie S6 Evolution of a simulation with contact-dependent signaling and a low VEGF decay rate and a high VEGF secretion rate (Figure 3.10**D**).

Movie S7 New sprout extending from a blob when VEGF is secreted by endothelial cells that are in contact with pericytes. This simulation was performed with 400 endothelial cells and 200 pericytes, and the following parameters: α(EC,VEGF) $= 10^{-3}$), ε(VEGF) $= 10^{-5}$, χ(EC,VEGF) $= 750$, and χ(PC,PDGFB) $= 500$).

4

Computational screening of angiogenesis model variants predicts that apelin signaling helps tip cells move to the sprout tip to accelerate sprouting

background graphic: network formed with selected tip and stalk cells, and tip cells that respond less to the chemoattractant than stalk cells.

Abstract

Angiogenesis involves the formation of new blood vessels by sprouting or splitting of existing blood vessels. During sprouting, a highly motile type of endothelial cell, called the tip cell, migrates from the blood vessels followed by stalk cells, an endothelial cell type that forms the body of the sprout. In vitro models and computational models can recapitulate much of the phenomenology of angiogenesis in absence of tip and stalk cell differentiation. Therefore it is unclear how the presence of tip cells contributes to angiogenesis. To get more insight into how tip cells contribute to angiogenesis, we extended an existing computational model of vascular network formation based on the cellular Potts model with tip and stalk differentiation, without making a priori assumptions about the specific rules that tip cells follow. We then screened a range of model variants, looking for rules that make tip cells (a) move to the sprout tip, and (b) change the morphology of the angiogenic networks. The screening predicted that if tip cells respond less effectively to an endothelial chemoattractant than stalk cells, they move to the tips of the sprouts, which impacts the morphology of the networks. A comparison of this model prediction with genes expressed differentially in tip and stalk cells revealed that the endothelial chemoattractant Apelin and its receptor APJ may match the model prediction. To test the model prediction we inhibited Apelin signaling in our model and in an in vitro model of angiogenic sprouting, and found that in both cases inhibition of Apelin or of its receptor APJ reduces sprouting. Based on the prediction of the computational model, we propose that the differential expression of Apelin and APJ yields a "self-generated" gradient mechanisms that accelerates the extension of the sprout.

4.1 Introduction

Angiogenesis, the formation of new blood vessels from existing vessels, is important in numerous mechanisms in health and disease, including wound healing and tumor development. As a natural response to hypoxia, normal cells and tumor cells secrete a range of growth factors, including vascular endothelial growth factors (VEGFs) and fibroblast growth factors (FGFs). These activate quiescent endothelial cells to secrete proteolytic enzymes, to migrate from the blood vessel and organize into an angiogenic sprout. Angiogenic sprouts are led by tip cells, a highly migratory, polarized cell type that extends numerous filopodia [15]. Tip cells express high levels of the VEGF receptor VEGFR2 [15], Delta-like ligand 4 (Dll4) [122] and, *in vitro*, CD34 [123]. The tip cells are followed by stalk cells [15], a proliferative and less migratory type of endothelial cell, which expresses low levels of Dll4 [122] and, *in vitro*, CD34 [123]

The behavior of tip and stalk cells during angiogenic sprouting has been well characterized in mouse retina models and in endothelial spheroids [17, 18]. From a mechanistic point of view, however, it is not well understood why two types of endothelial cells are involved in angiogenesis. Experimental and computational lines of evidence suggest that in absence of tip and stalk cell differentiation, endothelial cells can form blood-vessel like structures, albeit with abnormal morphological parameters. In cell cultures, endothelial cells organize into network-like structures, without obvious differentiation into tip and stalk cells [124, 125], although the individual endothelial cells were found to vary in other aspects of their behavior, e.g., their tendency to occupy the nodes of vascular networks [80]. Computational models have suggested a range of biologically-plausible mechanisms, by which populations of identical endothelial cells can self-organize into vascular network-like structures [20, 21, 25, 28, 30, 31, 126] and sprout-like structures can form in endothelial spheroids [28, 38, 126]. Experimental interference with tip and stalk cell differentiation modifies, but does not stop the endothelial cells' ability to form networks. In mouse retinal vascular networks, inhibition of Notch signaling increases the number of tip cells and produces denser and more branched vascular networks [57, 58, 60], while in gain-of-function experiments of Notch the fraction of stalk cells is increased, producing less extensive branching [57]. *In vitro*, similar effects of altered Notch signaling are observed [127–129]. Taken together, these observations suggest that differentiation between tip and stalk cells is not required for vascular network formation or angiogenic sprouting. Instead they may fine-tune angiogenesis, e.g., by regulating the number of branch points in vascular networks.

The exact mechanisms that regulate the differentiation of tip and stalk cell fate are subject to debate. Activation of the VEGFR2 by VEGF-A, which is secreted by hypoxic tissue, upregulates Dll4 expression [60–63]. Dll4 binds to its receptor Notch in adjacent endothelial cells, where it induces stalk cell phenotype [130], which includes downregulation of Dll4. The resulting lateral inhibition mechanism, together with increased VEGF signaling close to the sprout tip, may stimulate endothelial cells located at the sprout tip to differentiate into tip cells "in place". Detailed fluorescent microscopy of growing sprouts *in vitro* and *in vivo* shows that endothelial cells move along the sprout and "compete" with one another for the tip position [17, 18]. Endothelial cells expressing a lower amount of VEGFR2, and therefore producing less Dll4, are less likely to take the tip cell position, while cells that express less VEGFR1, which is a decoy receptor for VEGFR2 [131, 132], are more likely to take the tip cell position [17]. These results suggest that the VEGF-Dll4-Notch signaling loop is constantly re-evaluated and thereby tip cell fate is continuously reassigned. A series of recent observations, however, support an opposing view in which tip cells differentiate more stably. Tip cells express the

sialomucin CD34, making it possible to produce "tip cell" (CD34+) and "stalk cell" (CD34-) cultures using fluorescence-activated cell sorting (FACS) [123]. CD34+ cells have a significantly lower proliferation rate than CD34- cultures during the first 48 hours, suggesting that during this time they do not redifferentiate into stalk cells. In cultures of CD34-negative endothelial cells (stalk cells), the wild-type ratio of tip and stalk cells reestablishes only after around ten days. Thus within the time frame of *in vitro* vascular network formation of around 24 to 48 hours [45] cross-differentiation between tip and stalk cells is relatively rare. These data suggest that the differentiation between tip and stalk cells depends on a balance between (a) lateral inhibition via the Dll4-Notch pathway [57–60], and (b) a stochastically "temporary stabilized" tip or stalk cell fate, potentially correlated with CD34 expression [123].

  To develop new hypotheses on the role of tip and stalk cell differentiation during angiogenesis, we developed an explorative approach inspired by Long *et al.* [133] who used a genetic algorithm to identify the transition rules between endothelial cell behaviors that could best reproduce in vitro sprouting. Here we use a cell-based, computational model of angiogenesis [28] that is based on the Cellular Potts model (CPM) [84, 85]. We extend the model with tip and stalk cell differentiation, and systematically vary the parameters of the tip cells to search for properties that make the "tip cells" behave in a biologically realistic manner: i.e., they should move to the sprout tip and affect the overall branching morphology. We consider both a "pre-determined" model in which ECs are stably differentiated into tip and stalk cells throughout the simulation time of the model, and a "lateral inhibition" model, in which tip and stalk cells cross-differentiate rapidly via Dll4-Notch signaling. We compare the tip cell properties that our model predict with differential gene expression data, and experimentally test the resulting gene candidate in vitro.

4.2   Results

To develop new hypotheses on the role of tip cells during angiogenesis, we took the following "agnostic" approach that combines bottom-up modeling, bioinformatical analysis and experimental validation. We started from a previously published computational model of de novo vasculogenesis and sprouting angiogenesis [28]. Briefly, the model simulates the formation of sprouts and vascular networks from a spheroid of identical "endothelial cells", driven by an autocrine, diffusive chemoattractant that drives endothelial cells together (see [28] for details). In the first step, we assumed that a fraction of the cells are "tip cells" (tip cell fraction) and the remaining cells are "stalk cells", hence assuming that cross-differentiation between tip and stalk cells does not occur over the course of the simulation. We next systematically varied the model parameters of the tip cells to look for cell behavior that (a)

takes the tip cells to the sprout tips, and (b) changes the morphology of the simulated vascular networks formed in the model. The predicted differences between tip cell and stalk cell behavior were then expressed in gene ontology terms, so as to compare them with published gene expression differences between tip and stalk cells [123]. The analysis yielded a gene candidate that was further tested in an in vitro model of spheroid sprouting.

As a computational model for angiogenesis, we used our previous cell-based model of de novo vasculogenesis and sprouting angiogenesis [28]. The model assumes that endothelial cells secrete an autocrine, diffusive chemoattractant to attract endothelial cells. Due to the resulting attractive forces between the endothelial cells, the cells aggregate into a spheroid-like configuration. If the chemotactic sensitivity of the endothelial cells is restricted to the interfaces between the endothelial cells and the surrounding ECM by means of a contact inhibition mechanism, the spheroids sprout in microvascular network like configurations. Although our group [25, 126, 134] and others [19–23, 30] have suggested numerous plausible alternative mechanisms for de novo vasculogenesis and sprouting, in absence of a definitive explanatory model of angiogenesis we have selected the contact inhibition model for pragmatic reasons: It agrees reasonably well with experimental observation [28, 135], it focuses on a chemotaxis mechanism amenable to genetic analysis, and it has a proven applicability in studies of tumor angiogenesis [68], age-related macular degeneration [136], and toxicology [40].

The computational model is based on a hybrid, cellular Potts and partial differential equation method [84, 85, 90]. The cellular Potts method (CPM) represents biological cells as patches of connected lattice sites on a finite box Λ of a regular 2D lattice $\Lambda \subset \mathbb{Z}^2$ with each lattice site $\vec{x} \in \Lambda$ containing a *cell identifier* $\sigma \in \mathbb{Z}^{+,0}$ that uniquely identifies each cell. Each cell σ is also associated with a cell type $\tau(\sigma) \in \{\text{tip}, \text{stalk}, \text{ECM}\}$. To mimic amoeboid cell motility the method iteratively attempts to move the interfaces between adjacent cells, depending on the active motility of cells (expressed as a "cellular temperature" [76] $\mu(\tau)$) and a balance between the active forces the cells exert on their environment (e.g. due to chemotaxis or random motility) and the reactive adhesive, cohesive and cellular compression forces. Assuming overdamped motility, the CPM solves this force balance as a Hamiltonian energy minimization problem (see section 4.4.1 for details).

The angiogenesis model considers the following endothelial cell properties and behaviors that we will modify in tip cells: cell-cell and cell-matrix adhesion, volume conservation, cell elasticity, and chemotaxis at cell-ECM interfaces. To describe cell-cell adhesion we define a contact energy $J(\tau, \tau')$ that represents the cost of an interface between cells of type τ and τ'. We assume that cells resist compression and expansion by defining a resting area $A(\tau)$. In practice the cells fluctuate slightly around their resting area depending on

the elasticity parameter $\lambda(\tau)$. The cells secrete a diffusive chemoattractant c at a rate $\alpha(\tau)$, with $\frac{\partial c}{\partial t} = D\nabla^2 t - \epsilon(\tau)c + \alpha(\tau)$, where D is a diffusion coefficient, ϵ is a degradation rate, which is zero inside cells, and $\alpha(\text{ECM}) = 0$. Chemotaxis at cell-ECM interfaces is incorporated by biasing active cell extension and retractions up chemoattractant with a factor $\chi(\tau)$, which is the chemoattractant sensitivity. Table 4.1 lists the values used for these parameters, yielding the baseline collective cell behavior shown in Figure 4.1A.

Table 4.1: Parameter values for the angiogenesis and tip cell selection model. Underlined parameters are varied in the screen for tip cell behavior

Symbol	Description	Value
$\underline{\mu(\text{tip}),\mu(\text{stalk})}$	cell motility	50
$\underline{J(\text{tip,stalk})}$		
$J(\text{tip,tip})$	cell-ECM adhesion	20
$J(\text{stalk stalk})$		
$\underline{J(\text{tip,ECM})}$	cell-ECM adhesion	20
$J(\text{stalk,ECM})$		
$A(\text{tip})$, $A(\text{stalk})$	target area	100 pixels
$\underline{\lambda(\text{tip})}$, $\lambda(\text{stalk})$	elasticity parameter	25
$\underline{\chi(\text{tip})}$, $\chi(\text{stalk})$	chemoattractant sensitivity	500
$\underline{\alpha(\text{tip})}$, $\alpha(\text{stalk})$	chemoattractant secretion rate	10^{-3} s^{-1}
$\underline{\epsilon(\text{ECM})}$	chemoattractant decay rate in ECM	10^{-3} s^{-1}
$\epsilon(\text{tip})$, $\epsilon(\text{stalk})$	chemoattractant decay rate below cells	0
D	chemoattractant diffusion coefficient	10^{-13} m^{2}s^{-1}

4.2.1 Computational screening for putative tip cell behavior

We next set up a screen for differences in the parameters of tip cells and stalk cells that affect the outcome of the model. In particular, we looked for models in which tip cells lead sprouts in such a way that the network morphology is affected. In the angiogenesis model, a fraction (F_{tip}) of the endothelial cells is assumed to be the "tip cell", $\tau(\sigma) = \text{tip}$, and the remaining fraction $1 - F_{\text{tip}}$ is set to $\tau(\sigma) = \text{stalk}$. We assigned the baseline parameters used previously [28], and which are shown in Table 4.1, to "tip cells" ($\tau(\sigma) = \text{tip}$) and "stalk cells" ($\tau(\sigma) = \text{stalk}$). We varied the underlined parameters in Table 4.1 to change the behavior of "tip cells" and ran the simulation for 10 000 time steps for a series of tip cell fractions and a series of parameters. Figure 4.1B illustrates a typical range of morphologies, or *morphospace*, that we obtained in this way. We analyzed the position of tip cells in each mor-
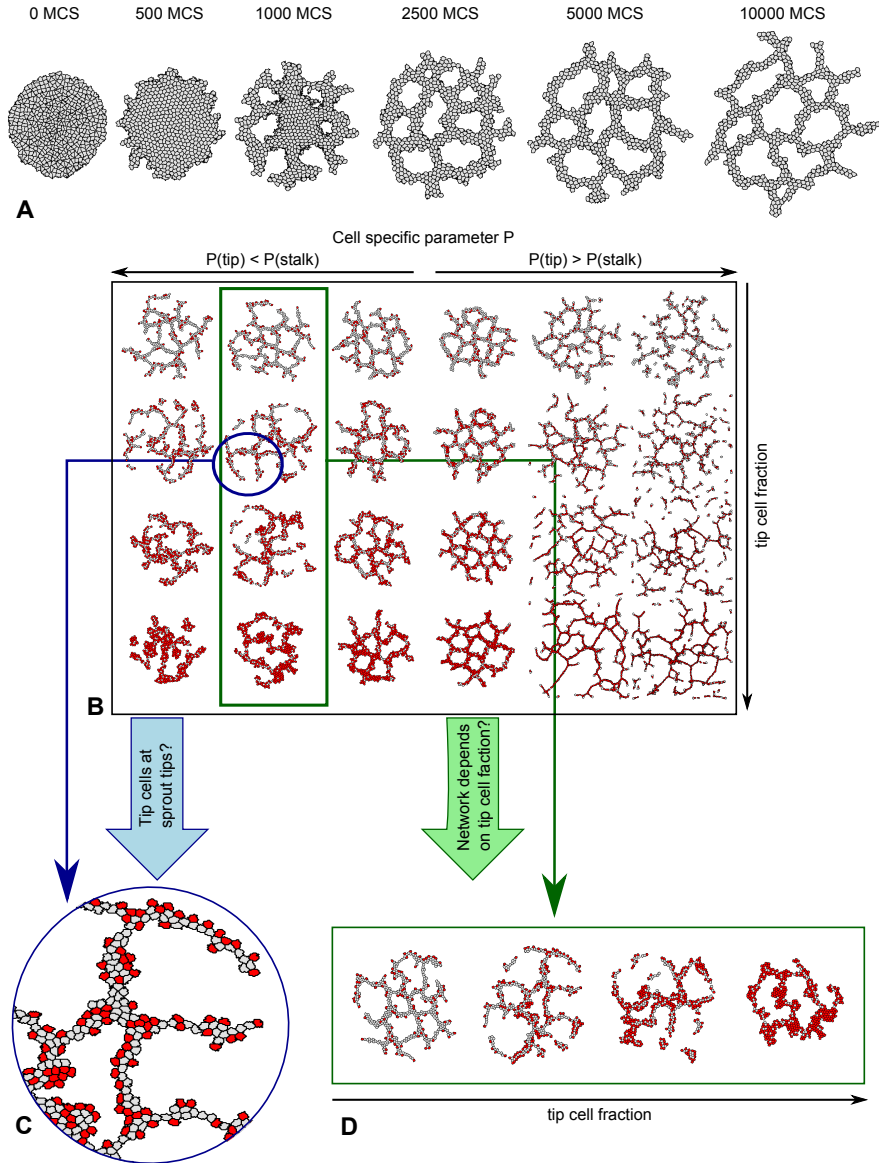
Figure 4.1: Overview of the angiogenesis model and the parameter search. **A** Time-lapse of angiogenesis model behavior **B** For each parameter P that is tested in the parameter search a morphospace is created to compare the different parameter values for different tip cell fractions. **C** Each morphology is studied in detail to see if the sprout tips are occupied by tip cells (red). **D** Each row of morphologies is studied to find rows in which the morphologies change, indicating that network formation depends on the tip cell fraction.

phology (Figure 4.1**C**) and analyzed the morphology of the vascular network in function of the tip cell fraction, F_{tip}.

To evaluate whether tip cells occupy sprout tips we simulated the model with a tip cell fraction of $F_{tip} = 0.2$ and automatically detected sprouts with tip cells on the tip and counted the percentage of sprouts with at least one tip cell at the sprout tip. If more sprout tips were occupied by a tip cell than in the control experiment with identical tip and stalk cells, the parameter values were retained for further analysis. Details on the automatic detection of tip cells on the sprouts tips are given in section 4.4.4.
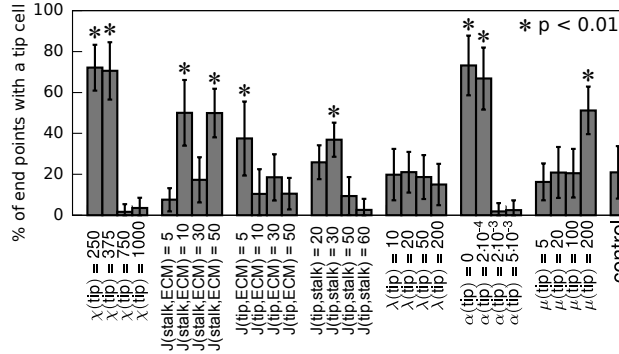
Figure 4.2: Differences in cell properties can enable cells of one type to occupy sprout tips. The percentage of sprout tips occupied by at least one tip cell was calculated at 10 000 MCS and averaged over 50 simulations (error bars depict the standard deviation). In each simulation 20% of the cells were predefined as tip cells. For each simulation one tip cell parameter was changed, except for the control experiment where the baseline parameters were used for both tip and stalk cells. p-values were obtained with a one sided Welch's t-test for the null hypothesis that the number of tip cells at the sprout tips is not larger than in the control simulation.

Figure 4.2 shows the percentage of sprouts tips occupied by one or more tip cells for all parameters tested. More sprouts are occupied by tip cells that: (a) are less sensitive to the autocrine chemoattractant than stalk cells ($\chi(tip) < \chi(stalk)$), (b) adhere more strongly to the ECM than stalk cells ($J(tip,ECM) < J(stalk,ECM)$), (c) adhere stronger to stalk cells than stalk cells to stalk cells ($J(tip,stalk) < J(stalk,stalk)$), (d) secrete the chemoattractant at a lower rate than stalk cells ($\alpha(tip) < \alpha(stalk)$), or (e) have a higher active motility than stalk cells ($\mu(tip) > \mu(stalk)$). Surprisingly, tip cells also move to the sprout tip if stalk cells adhere stronger to the ECM than tip cells while previous studies with the CPM showed that cells with the strongest ECM adhesion engulf other cells [85]. In the angiogenesis model stalk cells only surrounded tip cells when stalk cells adhere much stronger to the ECM than tip cells (Supplementary Figure S1A). Otherwise, chemotaxis prevented engulf-

ment and groups of tip cells occupied the sprout tips (Supplementary Figure S1**B**). Because such grouping of tip cells does not correspond with experimental observations [15], we omitted reduced stalk-ECM adhesion in our further analysis.

Out of the cell behaviors that turned out to make cells move to the sprout tips, we next selected cell behaviors that also affect network morphology. We quantified network morphology using two measures. The *compactness*, $C = A_{cluster}/A_{hull}$ is the ratio of the area of the largest cluster of connected cells, $A_{cluster}$, and the area of the convex hull enclosing the connected cluster, A_{hull} [28]. It approaches $C = 1$ for a disk and tends to $C \rightarrow 0$ for a sparse network. We also counted the number of "gaps" in the network, or lacunae, $N_{lacunae}$. For details see section 4.4.3.

Figure 4.3**A**-**F** plots the compactness C (black curves) and the number of lacunae $N_{lacunae}$ (blue curves) as a function of tip cell fraction, and compares them with 'baseline' simulations containing only 'stalk cells' (as in Figure 4.1**A**). Closed symbols indicate a significant difference with the baseline simulations (Welch's t-test, $p < 0.05$, $n = 10$). Cell behaviors that affected network morphologies for at least half of the tip cell fractions tested were kept for further analysis. The screening thus selected three putative tip cell behaviors: reduced chemoattractant sensitivity (χ(tip) $< \chi$(stalk); see Figure 4.3**A**), reduced chemoattractant secretion by tip cells (α(tip) $< \alpha$(stalk); see Figure 4.3**E**), and increased tip-ECM adhesion (J(stalk,ECM) $> J$(tip,ECM); see Figures 4.3**B**-**C**). Among the latter two (panels **B** and **C**) it turned out that for J(tip,ECM) $= 5$ (Figure 4.3**C**) networks could not form with too many tip cells (see Supplementary Movie S1). For this reason we will model increased ECM adhesion for tip cells by reducing the adhesion of stalk cells with the ECM (J(stalk,ECM)).

To estimate how much tip cell behavior may differ from stalk cell behavior in our model, we repeated the screening for additional values of χ(tip), α(tip), and J(stalk,ECM) (Supplementary Figure S2) . The screening showed that for each behavior there is a range of parameter values for which tip cells occupy the sprout tips and affect network formation, with two exceptions: (1) When the chemoattractant sensitivity of tip cells became 100 or less, the networks disintegrated (Supplementary Figure S2**J**) (2) If the adhesion between of tip cells became too strong because the adhesion energy between stalk cells and ECM (J(stalk,ECM)) became 70 or more, they spread out over the stalk cells, covering the whole network (Supplementary Figure S2**K**). Because the values of the parameters associated with chemotaxis were estimated in absence of experimental values, we repeated the screening for three alternative sets of baseline parameter values for which network formation was not affected. The results of these extra screenings were similar to those of the screening with the baseline parameters (Supplementary Figures S3 and S4).
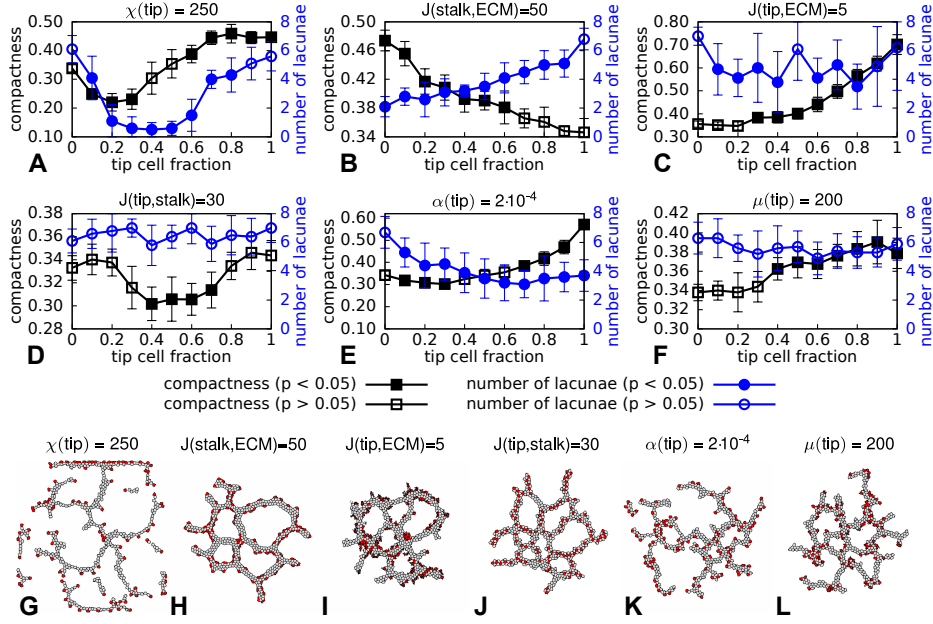
Figure 4.3: Effects of different tip and stalk cell properties on network morphology. **A–F** Trends of compactness (black rectangles) and number of lacunae (blue circles) calculated with the morphologies at 10 000 MCS. For each data point 10 morphologies were analyzed and the error bars represent the standard deviation. p-values were obtained with a Welch's t-test for the null hypothesis that the mean of the sample is identical to that of a reference with the baseline parameters listed in Table 1. For **B** this reference is the data for tip cell fraction 1 and for all other graphs this is the data for tip cell fraction 0. **G-L** Morphologies after 10 000 MCS for each tested parameter value with $F_{tip} = 0.2$.

Altogether, the computational screening presented in this section identified three tip cell parameters that affect tip cell position in the sprout and the morphology of the networks formed in our computational model: reduced secretion of the chemoattractant, reduced sensitivity to the chemoattractant, and increased tip-ECM adhesion. It is possible, however, that these effects are due to spatial or temporal averaging of tip and stalk cell parameters, not due to interaction of two different cell types. The next section will introduce a control for such effects.

### 4.2.2 Comparison with control model selects "reduced chemotactic sensitivity" model for further analysis

The computational screening highlighted three tip cell parameters that both affected the position of tip cells in the sprouts and affected network morphology: increased tip-cell ECM adhesion, reduced chemoattractant secretion by tip cells, and reduced chemoattractant sensitivity of tip cells. Because it was unsure whether these effects were due to (a) the differential cell behavior of tip and stalk cells, or (b) due to temporal or spatial averaging of the parameters differentially assigned to tip and stalk cells, we compared the results against a control model with a uniform cell type with "averaged" parameters, $P(\text{cell}) = (1 - F_{\text{tip}}) \cdot P(\text{stalk}) + F_{\text{tip}} \cdot P(\text{tip})$, with $P(\text{tip})$ the tip cell parameter value and $P(\text{stalk})$ the stalk cell parameter value.

  For each of the three parameters identified in the first step of the computational screening, we compared the morphologies formed in the control model after 10000 MCS with the morphologies formed in the original model with mixed cell types (Figure 4.4). With increased ECM adhesion, the morphologies resulting from the model with mixed cell types (Figure 4.4**A**) did not appear visually different from the control model (Figure 4.4**B**). Although small differences were observed in the compactness values (Figure 4.4**E**), the morphometric measures for branching did not differ significantly between the control and 'mixed' model (Figure 4.4**C**-**D**). Next, we compared the model with reduced chemoattractant secretion rates in tip cells with the averaged control. Visual comparison of the results and suggested that the model with mixed cell types produces similar morphologies as the control model (Figure 4.4**F**-**G**). This observation was confirmed by all three morphometric measures (Figure 4.4**H**-**J**). Finally, we compared the results of the mixed and control model for tip cells with reduced chemoattractant sensitivity. The networks formed with mixed cells had larger lacunae and thinner branches, and were less regular than those formed by the control model (Figure 4.4**K**-**L**), and observation that was confirmed by the morphometrics for almost all tip cell fractions (Figure 4.4**M**-**O**). From these results we concluded that among the tip cell parameters that we have tested in our model, only in the reduced chemoattractant sensitivity model the position of the tip cells affected the morphology. We thus retained only this model for further analysis.

4.2.3 Local tip cell selection regularizes network morphology

In the parameter screenings presented in the previous sections, to first approximation we assumed that a subpopulation of endothelial cells are "predetermined" to become tip cells, e.g., due to prior expression of CD34 [123]. It is likely, however, that tip cell fate is continuously "re-evaluated" in a Dll4-Notch-VEGFR2 signaling loop [57–60]. Tip cells express Dll4 on their cell
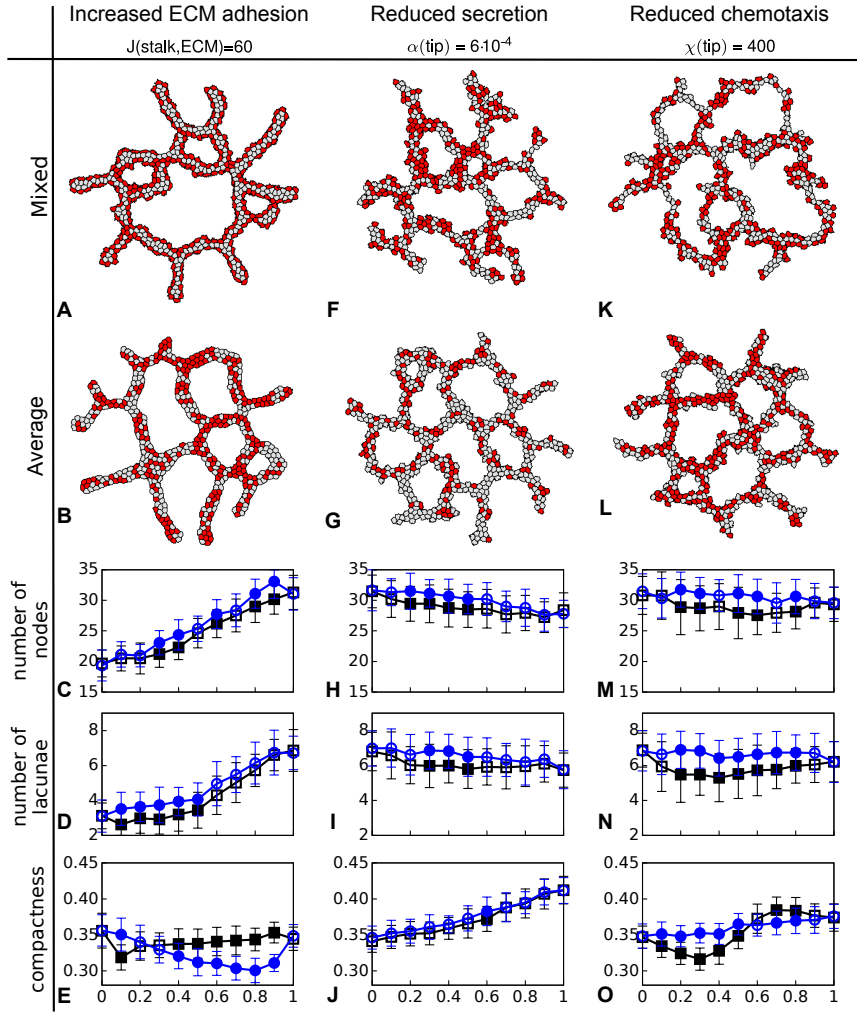
Figure 4.4: Comparison of networks formed with mixed cells and cells with average properties. **A, F,** and **K** morphologies for mixed tip (red) and stalk (gray) cells ($F_{tip} = 0.5$). **B, G,** and **L** morphologies for averaged cells ($F_{tip} = 0.5$). **C-E, H-J,** and **M-O** morphometrics for a range of tip cell fractions for both the control and mixed model. The morphometrics were calculated for 50 simulations at 10 000 MCS (error bars represent the standard deviation). p-values were obtained with a Welch's t-test for the null hypothesis that the mean of mixed model and the control model are identical.

membranes [122], which binds to the Notch receptor on adjacent cell membranes. This leads to the release of the Notch intracellular domain (NICD), activating the stalk cell phenotype [57, 59]. Via this lateral inhibition mechanism, cells adjacent to tip cells tend to differentiate into stalk cells. To simulate such "dynamic tip cell selection", a simplified genetic regulatory network (GRN) model of Dll4-Notch signaling was added to each simulated cell, as described in detail in section 4.4.2. Briefly, the level of NICD in each cell is a function of the amount of Dll4 expressed in adjacent cells, weighed according to the proportion of the cell membrane shared with each adjacent cells. If the NICD level in a cell exceeds a threshold, Θ_{NICD}, it differentiates into a stalk cell, otherwise it becomes a stalk cell [57–59].

Figure 4.5 shows the behavior of the initial 'static model' (Figures 4.5**A**-**F**) in comparison with the 'dynamic tip cell selection' model (Figures 4.5**G**-**L**). In the dynamic model the tip cell fraction was set using the values of Θ_{NICD}, such that the exact tip cell fractions depended on the local configurations. In comparison with the initial, 'static' model (Figure 4.5**A**-**F**), the model with 'dynamic' selection (Figure 4.5**G**-**L** and Supplementary Movie S3) seems to form more compact and regular networks. To quantify this difference in network regularity, we determined the variation of the areas of the lacunae of the networks at the final time step of a simulation. Figure 4.5**M** shows this measurement averaged over 50 simulations for a range of tip cell fractions. Lacunae in networks formed from mixtures of stalk cells and 10% to 60% 'static' tip cells have more variable sizes than lacunae in networks formed by the 'dynamic tip cell' model.

To further analyze how dynamic tip cell selection regularized network morphologies in our model, we studied in detail how tip cells contributed to network formation in the 'static' and 'dynamic' tip cell models. Figure 4.5**N**-**Q** shows the evolution of a part of a network formed with 20% 'static tip cells'. At first, some tip cells locate at sprout tips and others are located adjacent to or within the branches (Figure 4.5**N**). The chemoattractant gradually accumulates 'under' the branches, with a curvature effect producing slightly higher concentrations at the side of the lacunae. This attracts the stalk cells (Figure 4.5**O**), 'squeezing' the tip cells out of the branch and away from the lacuna, due to their reduced chemoattractant sensitivity (Figure 4.5**P** and Supplementary Movie S2). The resulting layered configuration with tip cells at the outer rim drives a drift away from the lacuna (Figure 4.5**Q**): Due to their stronger chemotactic sensitivity, the stalk cells attempt to move to the center of the configuration, pushing the tip cells away, thus leading to directional migration driven by a "self-generated gradient" mechanism [137].

In the 'dynamic tip cell selection' mechanism, such migration directed by self-generated gradients will occur only at the sprout tips, where tip cells are selected. The model thus suggests that tip cells could assist in produc-
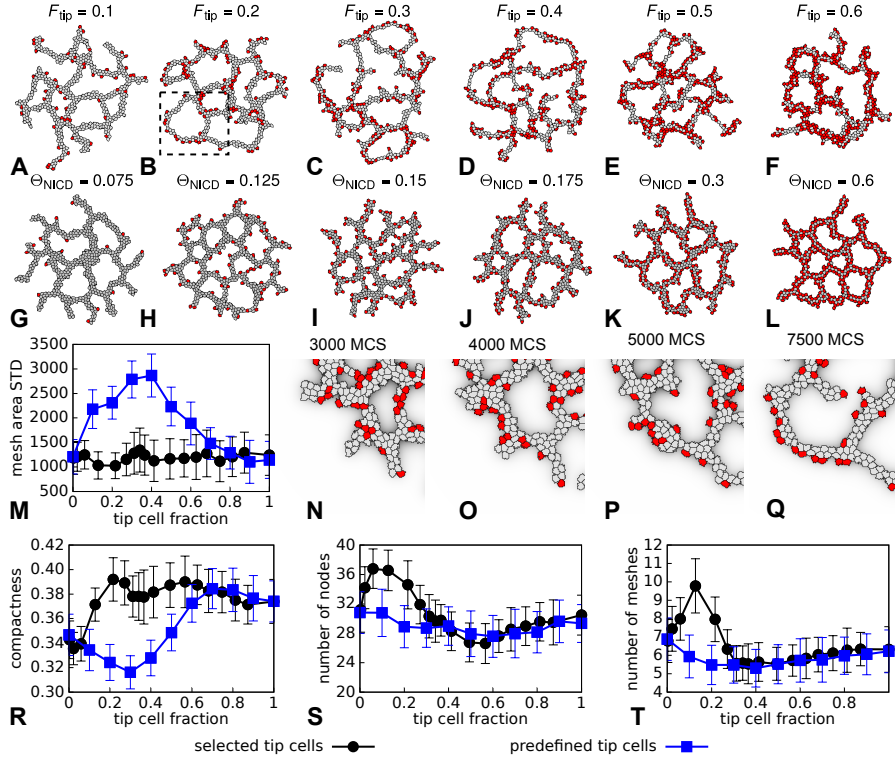
Figure 4.5: Effects of tip cell selection on network formation. **A-F** Networks formed with varying fractions of predefined tip cells (F_{tip}) with $\chi(tip) = 400$ at 10 000 MCS. **F-L** Networks formed with selected tip cells for varying NICD thresholds (Θ_{NICD}) at 10 000 MCS. **M** Standard deviation of lacuna area in a network after 10 000 MCS. **N-Q** Close up of the evolution of a network with 20% predefined tip cells (marked area in **B**). **R-T** Comparison of the morphometrics for networks formed with predefined and selected tip cells with reduced chemoattractant sensitivity ($\chi(tip) = 400$) and network at 10 000 MCS. For the simulations with tip cell selection, the average tip cell fraction was calculated for each NICD threshold. For all plots (**M** and **R-T**) the values were averaged over 50 simulations and error bars depict the standard deviation.

ing a local, self-generated gradient mechanism that directs the migration of sprouts, a mechanism that requires tip cells to differentiate only at sprout tips. For tip cells to "drag" just the sprouts, only a limited number of tip cells must be present in the network. To test this idea, we compared network morphologies for the 'dynamic' and the 'static' tip cell models for a range of tip cell fractions (Figure 4.5**R**-**T**). Indeed, the network morphologies were practically identical for high tip cell fractions, whereas they differed significantly for all three morphometrics for tip cell fractions between 0.1 and 0.3: In the dynamic selection model the networks become more disperse (Figure 4.5**R**) and formed more branches (Figure 4.5**S**) and lacunae (Figure 4.5**T**) than in the 'static' model.

 To validate the 'dynamic' tip cell model, we compared the effect of the tip cell ratio on network morphology with published experimental observations. The in vivo, mouse retinal angiogenesis model is a good and widely used model for tip/stalk cell interactions during angiogenesis [17, 18, 57, 58, 60, 61, 138–140]. Networks formed with an increased abundance of tip cells become more dense and form a larger number of branches [57, 58, 60, 61] than wild type networks. Our computational model is consistent with this trend for tip cell fractions between 0 and up to around 0.2 (Figure 4.5**R**-**T**), but for tip cell fractions > 0.2 the vascular morphologies become less branched (Figure 4.5**S**-**T**). To investigate in more detail to what extent our model is consistent with these experimental observations, we tested the effect of the tip cell fraction in the 'dynamic' tip cell selection model in more detail. In particular we were interested in how the difference in chemotactic sensitivity between tip and stalk cells affected network morphology. Figure 4.6 shows the effect of the NICD threshold (increasing the NICD threshold is comparable to inhibiting Dll4 expression or Notch signaling, and hence controls the tip cell fraction) for a range of tip cell chemotactic sensitivities. When the difference in the chemotactic sensitivity between tip and stalk cells is relatively small ($\chi(\text{tip}) \geq 300$)), increasing the NICD threshold results in the formation of denser network with fewer lacunea. In contrast, when the difference in chemotactic sensitivity between tip and stalk cells is larger ($\chi(\text{tip}) \leq 200$), there exists an intermediate state in which the networks are both compact an d have a large number of branch points (Figure 4.6**A4** and 4.6**B4**). This intermediate state resembles the dense, highly connected networks that are observed when tip cells are abundant in the mouse retina [57, 58, 60, 61]. Thus, when the difference in the chemotactic sensitivity of tip and stalk cells is sufficiently large, the model can reproduce both normal angiogenesis and the excessive angiogenic branching observed for an abundance of tip cells [57].
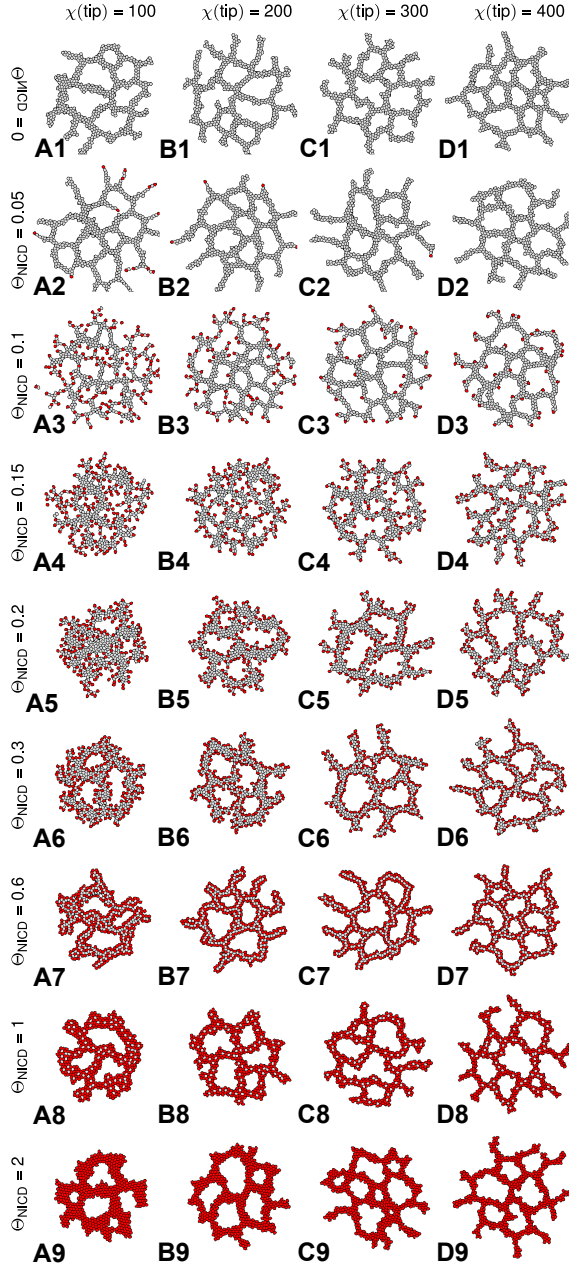
Figure 4.6: Effects of reducing tip cell chemoattractant sensitivity for varying NICD thresholds. Morphospace of the final morphologies (10 000 MCS) with varying tip cell chemoattractant sensitivities ($\chi(\text{tip})$) and NICD thresholds (Θ_{NICD}).

4.2.4 Survey for chemoattractant receptors reduced in tip cells reveals Apelin as candidate

The comparative, computational model analysis of the role of tip cells in angiogenesis, predicted that–among the models tested–a model where tip cells show reduced sensitivity to an autocrine chemoattractant best matches tip cell phenomenology: The tip cells lead the sprouts, and facilitate the formation of vascular networks of regular morphology for tip cell fractions of up to around 0.2. Could a chemoattractant with these, or very similar properties be involved in vascular development? To answer this question, we evaluated four comparative studies of gene expression in tip and stalk cells [123, 141–143]. These studies identified three receptors involved in endothelial chemotaxis that were differentially expressed in tip cells and stalk cells: VEGFR2, CXCR4, and APJ. VEGFR2 is upregulated in tip cells [123, 140, 141]. VEGFR2 is a receptor for the chemoattractant VEGF that is secreted by hypoxic tissue [116]. Whether or not VEGF is secreted at sufficiently high levels to act as an autocrine chemoattractant between ECs has been under debate [28, 119, 144], with the emerging being that it is most likely a long-range guidance cue of angiogenic sprouts secreted by hypoxic tissues ([15]; reviewed in Geudens and Gerhardt 2011 [145]). The chemokine CXCL12 and its receptor CXCR4 [146] are both upregulated in tip cells [123, 141, 143], suggesting that tip cells would have higher, not lower sensitivity to CXCL12 signaling than stalk cells. Interestingly, CXCL12 and CXCR4 are key components of a self-generated gradient mechanism for directional tissue migration in the lateral line primordium mechanisms [137]. Because of the key role of CXCL12/CXCR4 in angiogenesis (see, e.g., [147]) it is therefore tempting to speculate that CXCL12/CXCR4 may be part of a similar, self-generated gradient mechanism during angiogenesis. However, because CXCL12 expression is upregulated in tip cells relative to stalk cells, not downregulated, we will focus here on a third receptor/ligand pair differentially expressed in tip and stalk cells: APJ and Apelin. APJ is a receptor for the endothelial chemoattractant Apelin [148–150] that is secreted by endothelial cells [149, 150]. Apelin expression is upregulated in tip cells [123, 142, 143], whereas its receptor APJ is not detected in tip cells [142]. Thus the expression pattern of Apelin and its receptor APJ fits with our model prediction: Apelin is an endothelial chemoattractant that is secreted by endothelial cells and tip cells are less responsive to Apelin than stalk cells. In our model the chemoattractant is secreted at the same rate by tip and stalk cells, whereas Apelin is preferentially expressed in tip cells. The next section will therefore add preferential secretion of Apelin by tip cells to the model, and test if and how this changes the predictions of our model.

4.2.5 Model refinement to mimic role of Apelin/APJ more closely
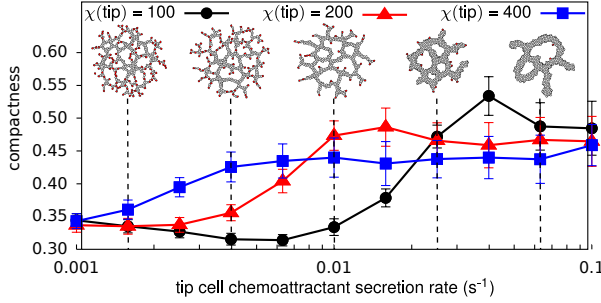
Figure 4.7: Effects of increasing tip cell Apelin secretion rate for varying levels of tip cell chemotaxis. Average compactness of the final network (10 000 MCS) with the morphologies for $\chi(\text{tip}) = 100$ for tip cell Apelin secretion rates of $\alpha(\text{tip}) = 1.6 \cdot 10^{-3}, \alpha(\text{tip}) = 4.0 \cdot 10^{-3}, \alpha(\text{tip}) = 1 \cdot 10^{-2}, \alpha(\text{tip}) = 1.6 \cdot 10^{-2}$, and $\alpha(\text{tip}) = 4.0 \cdot 10^{-2}$ as insets. Except for $\alpha(\text{tip})$, all parameters have the values listed in Table 4.1. Data points show average values for $n = 50$ simulations with error bars giving the standard deviation.

The computational analyses outlined in the previous sections suggest that Apelin and its receptor APJ might act as an autocrine chemoattractant in the way predicted by our model: Both stalk cells and tip cells secrete Apelin and APJ [149, 150] and the tip cells do not express the APJ receptor [142]. Gene expression analyses [123, 142] also suggest that tip cells secrete Apelin at a higher rate than stalk cells. We therefore tested if the simulation results still held if we changed the model assumptions accordingly: In addition to a reduced chemotactic sensitivity in tip cells ($\chi(\text{tip}) = 100$), we assumed tip cells secrete chemoattractant at a higher rate than stalk cells: $\alpha(\text{tip}) > \alpha(\text{stalk})$. Although the absence of APJ expression in tip cells suggests that tip cells are insensitive to the chemoattractant, $\chi(\text{tip}) = 0$, to reflect the phenomenological observation that ECs are attracted to one another, we set $\chi(\text{stalk}) > \chi(\text{tip}) > 0$. Such intercellular attraction could, e.g., be mediated by cell-cell adhesion, by alternative chemoattractant-receptor pairs (e.g., CXCR4-CXCL12 [151]), or by means of mechanical EC interactions via the extracellular matrix[152]. Figure 4.7 shows how the Apelin secretion rate in tip cells ($\alpha(\text{tip})$) affects the morphology of the vascular networks formed in our model, as expressed by the compactness. For tip cell secretion rates of up to around $\alpha(\text{tip}) = 0.01$ the model behavior does not change. The networks became more compact for tip cell chemoattractant secretion rates of $\alpha(\text{tip}) > 0.01$, in which case stalk cells were attracted to tip cells and laterally inhibited tip cells. Except for those cases, after correcting the model to better mimic the expression pattern of Apelin and APJ, it formed vascular-like networks similar to those formed in the original model with only reduced tip cell chemotaxis.
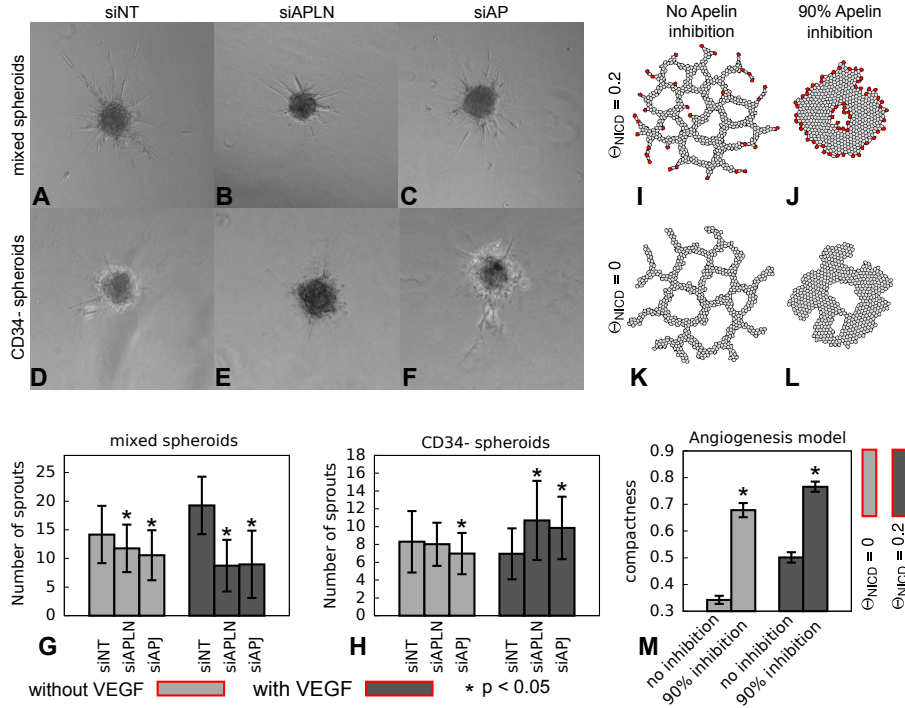
4.2.6 Apelin or APJ silencing inhibits sprouting in vitro and in silico

To validate the possible role of Apelin signaling in angiogenic sprouting predicted by our model, we asked if and how silencing of Apelin signaling affects angiogenic sprouting from endothelial spheroids *in vitro*. Previous studies have shown that Apelin promotes angiogenesis of retinal endothelial cells seeded on Matrigel [149], as well as in *in vivo* systems such as the mouse retina, xenopus embryo, and chick chorioallantoic membrane [153]. Furthermore, *in vivo* inhibition of Apelin or APJ reduced sprouting in xenopus embryos [153], zebrafish [154], and the mouse retina [142, 155]. These results suggest that Apelin signaling indeed regulates angiogenic sprouting, but they do not imply a relation between Apelin signaling and tip cell driven angiogenesis. To assess the relation between tip-stalk cell interaction and Apelin signaling, we inhibited Apelin signaling in an in vitro model of angiogenic sprouting in which the fraction of CD34- ("stalk") cells could be controlled. Spheroids of immortalized human microvascular endothelial cells (HMEC-1s) were embedded in collagen gels and in collagen enriched with VEGF. After culturing the spheroids for 24 hours at 37 degrees Celcius under 5% CO_2, the cultures were photographed and the number of sprouts were counted using the semi-automated image analysis software ImageJ. We compared sprouting in a "mixed" spheroid of HMEC-1s with a population enriched in "stalk cells", i.e., a population of CD34- HMEC-1s sorted using FACS. To inhibit Apelin signaling, the spheroids were treated with an siRNA silencing translation of Apelin (siAPLN) or of its receptor (siAPJ).

Figure 4.8A-**F** and **K**-**L** show how the spheroid morphology is affected by the silencing RNA treatments. Relative to a control model with non-targeting siRNA (siNT), mixed spheroids treated with siAPLN or siAPJ formed fewer (Figure 4.8 **A**-**C** and **G**, Supplementary Figure S5, and Supplementary Table S1). The effects of siAPJ and siAPLN on the average sprout length are inconclusive because of large variations in the results of the duplicate experiments. In CD34- spheroids these different effects were observed (Figure 4.8**D**-**F** and **H**). siRNA treatments interfering with Apelin treatments slight improved sprouting in some experiments and reduced it in others (Supplementary Figure S5, and Supplementary Table S2). Thus in spheroids containing a wild-type mix of CD34+ and CD34- inhibition of Apelin signaling reduced sprouting, whereas results for spheroids enriched in CD34- cells were variable.

We next asked if the observed reduction of sprouting associated with inhibition of Apelin-signaling also occurred in the computational model. To mimic application of siAPLN in the computational model, we reduced the secretion of the chemoattractant both in tip and stalk cells to $\alpha(\text{tip}) = 10^{-3}$ and $\alpha(\text{stalk}) = 10^{-4}$. To mimic wild-type spheroids we used $\Theta_{\text{NICD}} = 0.2$, which yields a mix of CD34+ and CD34- cells. To mimic spheroids enriched

Figure 4.8: Effects of Apelin or APJ silencing in spheroid sprouting assays. **A-F** Microscopy images of the WT and CD34- spheroids in VEGF-enriched collage after 24 hours. **G-H** Number of sprouts after 24 hours for spheroids with mixed cells and CD34- spheroids. These metrics are the average of all successfully cultured spheroids in all duplicate experiments with the error bars depicting standard deviation. The * denotes $p < 0.05$, see section 4.4.6 for details of the statistical analysis. **I-L** Comparison of final morphologies (10 000 MCS) formed by the computational angiogenesis model without and with inhibited Apelin-signaling. **M** Average compactness of the final morphology (10 000 MCS) for 50 simulations with the error bars depicting the standard deviation. The * denotes $p < 0.05$ and the p-values where obtained with a Welsh' t-test.

in stalk cells reduced the NICD-levels to $\Theta_{NICD} = 0$, for which all cells are stalk cells. Figure 4.8**I-M** shows how the model responds to the inhibition of Apelin-signaling: For both the NICD thresholds, inhibition of Apelin-signaling reducing sprouting (appearing as an increased compactness and visible in Supplementary Movie S4), as in the experiment with wild-type mixtures of CD34+ and CD34- endothelial cells. Because the CD34- spheroids may contain a few tip cells, we repeated the simulations with an NICD threshold that allows for a few tip cells ($\Theta_{NICD} = 0.05$), which yielded results similar to those for $\Theta_{NICD} = 0$.

4.3 Discussion

In this work we asked how and by what mechanisms tip cells can participate in angiogenic sprouting. We employed a suitable computational model of angiogenic network formation [28], which was extended with tip and stalk cell differentiation. In the extended model, the behavior of tip and stalk cells could be varied independently by changing the model parameters. Instead of testing preconceived hypotheses on tip and stalk cell behavior, we took a "reversed approach" in which we could rapidly compare series of alternative hypothesis: We systematically searched for parameters that led tip cells to occupy the sprouts tips, and that changed the morphology of the angiogenic networks relative to a baseline set of simulations in which tip and stalk cells have identical behavior. We studied two cases, reflecting the two extremes in the range of known molecular mechanisms regulating tip and stalk cell differentiation. In the first case, we assumed that endothelial cells are differentiated stably between a tip and stalk cell phenotype within the characteristic time scale of angiogenic development (approximately 24 to 48 hours). In the second case, we assumed a much more rapidly-acting lateral inhibition mechanism, mediated by Dll4 and Notch. Here endothelial cells can switch back and forth between tip and stalk cell fate at time scales of the same order of cell motility. Our analysis showed that in a model driven by contact-inhibited chemotaxis to a growth factor secreted by ECs, tip cells that respond less to the chemoattractant move to the tips of the sprouts and speed up sprout extension. Under the same conditions, more regular and more dense networks formed if ECs switched between tip and stalk cell fate due to lateral inhibition. This change in morphology occurred because without tip cell selection tip cells can be present anywhere in the network, whereas with tip cell selection tip cells are limited to growing sprouts. Therefore, with tip cell selection a "self-generated gradient mechanism" [137] drives extension of the sprout at the right position: only at the tips of growing sprouts. We next asked if a growth factor with the predicted properties is involved in angiogenic sprouting. To this end we looked for matching, differential gene expression patterns in published data sets of gene expression in tip and stalk cells. In particular the Apelin-APJ ligand-receptor pair turned out to be a promising candidate. Because Apelin is a chemoattractant for endothelial cells that is secreted by endothelial cells and the receptor APJ is only detected in stalk cells. We then included the expression pattern of Apelin and APJ in the model and predicted that inhibition of Apelin signaling inhibits sprouting. In agreement with those model predictions, *in vitro* experiments on endothelial spheroids showed that inhibition of Apelin or its receptor APJ reduced *in vitro* spheroid sprouting. Thus the reversed bottom-up simulation approach employed in this study, combined with an analysis of published, top-down gene expression studies here helped identify a candidate molecule mediating the interaction

between tip and stalk cells during angiogenesis.

Our approach was inspired by a recent study that used a computational model to identify what cell behavior changed when endothelial cells were treated with certain growth factors [133]. This study used an agent-based, 3D model of angiogenesis in which sprouts extend from a spheroid. With a genetic algorithm the parameters for which the model reproduces experimental results are derived. In this way Long *et al.* [133] could hypothesize what changes in cell behavior the growth factors caused and successfully derived how certain growth factors affect cell behavior in 3D sprouting assays. Here, we used a similar approach to study what behavior makes tip cells lead sprouts and affect network formation, using high-throughput parameter studies instead of objective optimization approaches. Tip-stalk cell interactions have been studied before with several hypothesis-driven models where specific behavior was assigned to the tip cells based on experimental observations, and tip cells were either defined as the leading cell [33–35, 156–158] or tip cell selection was modeled such that the tip cell could only differentiate at the sprout tip [40, 44, 159]. These models have been used to study how extracellular matrix (ECM) density [156], ECM degradation [156], ECM inhomogeneity [33, 34], a porous scaffold [157, 158], cell migration and proliferation [35, 44], tip cell chemotaxis [159] and toxins [40] affect sprouting and angiogenesis. Thus these studies asked how a specific hypothesis of tip cell behavior and tip cell position affected the other mechanisms and observables in the simulation. Our approach aims to develop new models for the interaction between tip and stalk cells that can reproduce biological observation. These new hypotheses can be further refined in hypothesis-driven model studies, as we do here, e.g., in Figure 4.7.

In order to make this "reversed" approach possible, we have simplified the underlying genetic regulatory networks responsible for tip-stalk cell differentiation. These molecular networks, in particular Dll4-Notch signaling, have been modeled in detail by Bentley *et al.* [41, 42]. Their model describes a strand of endothelial cells, and was used to study how lateral inhibition via Dll4-Notch signaling in interaction with VEGF signaling participates in tip cell selection. With this model Bentley and coworkers predicted that the shape of the VEGF gradient determines the rate of tip cell selection, and that for very high levels of VEGF the intracellular levels of Dll4 and VEGFR2 oscillate. Based on their experimental observations that tip cells migrate within a sprout, cell movement has been added to model by allowing cells to switch positions along the sprout [17]. Bentley and coworkers reproduced tip cell migration in the sprout and showed that the VEGFR2 levels in a cell determine the chance of that cell to become a tip cell. The migration of tip cells in a sprouts was further studied using a model that included a cell migration model [140]. Bentley and coworkers [140] thus showed that the differences

in VE-cadherin expression between tip and stalk cells could cause tip cell migration to the sprout tip. Altogether, these models gave useful insights in the role of Dll4-Notch signaling and VEGF signaling in tip cell selection in a growing sprout. Here, instead of focusing at single sprouts, we focused on the scale of a vascular network. By combining a tip cell selection model with a cell based model of angiogenesis, we showed that tip cell selection can aid the development of dense networks by limiting the destabilizing effects of tip cells.

The model prediction that tip cells respond less to a chemoattractant secreted by all endothelial cells fits with the expression pattern of the chemoattractant Apelin, which is secreted by all endothelial cells and of which the receptor is not detect in tip cells. Previous studies indicated that Apelin induces angiogenesis *in vitro* [149, 150]. Apelin-APJ signaling is necessary for vascular development *in vivo* systems such as in the mouse retina [155], frog embryo [150, 153], and chicken chorioallantoic membrane [153]. Furthermore, high levels of vascularization in human glioblastoma are correlated with high expression levels of Apelin and APJ [150]. Based on these observations Apelin is considered to be a pro-angiogenic factor. Similar to other pro-angiogenic factors such as VEGF [160], Apelin is expressed near areas where blood vessels develop and Apelin expression is induced by hypoxia [154]. The pro-angiogenic role of Apelin is linked to its role as a chemoattractant [153, 154] and mitogenic factor [153, 154]. However, the role of Apelin in proliferation may be disputed because Apelin did not promote proliferation in a series of sprouting assays with human umbilical vein endothelial cells, human umbilical arterial endothelial cells, and human dermal microvascular endothelial cells [150]. In this work we show that Apelin can promote angiogenesis if we assume that Apelin is an autocrine chemoattractant and that its receptor APJ is only expressed in stalk cells. Thus our model suggests that chemotaxis towards Apelin can induce angiogenesis independent of Apelin-induced proliferation.

In line with our model prediction, inhibition of Apelin signaling does inhibit sprouting in our 3D sprouting assays. This inhibition of sprouting is manifested as a decrease in the number of sprouts. As mentioned above, Apelin may promote proliferation, and thus inhibition of Apelin signaling may results in a reduced proliferation rate. A reduced proliferation rate would cause the sprouts to shorten, but no tot decrease the number of sprouts. This indicates that the mechanism that drives sprouting is affected by the inhibition of Apelin signaling. However, whereas in the model inhibition of Apelin signaling inhibits sprouting for all tested cases, in the experimental assays the effects of Apelin or APJ inhibition depended on the fraction of tip cells and the environment. In mixed spheroids, Apelin and APJ inhibition reduced sprouting in both plain and VEGF-enriched collagen. In CD34- spheroids, i.e., spheroids

enriched in stalk cells, Apelin or APJ inhibition slightly inhibited sprouting in plain collagen, whereas it enhanced sprouting in VEGF-enriched collagen matrices. This suggests that, in a VEGF rich environment, Apelin-APJ signaling inhibits sprouting by stalk cells. VEGF has been shown to induce tip cell fate [139, 161], as well as APJ expression [162, 163]. However, it remains unclear how the combination of a VEGF rich environment and Apelin signaling could inhibit sprouting.

  The importance of VEGF in our validation experiments suggests that we cannot ignore VEGF in our tip cell selection model. Dll4-Notch signaling and VEGF signaling interact directly in two ways. First, Dll4 is upregulated by signaling between VEGF and VEGF receptor 2 (VEGFR2) [139, 161]. Second, Dll4-Notch signaling downregulates VEGFR2 [58, 128, 141, 164] and upregulates VEGF receptor 1 (VEGFR1) [141, 165], which acts as a decoy receptor for VEGF [166]. Because *in vivo* VEGF acts as an external guidance cue for angiogenesis, the interplay between VEGF signaling and Dll4-Notch signaling could promote tip cell selection in the growing sprouts. The expression levels of VEGFR2 also directly reduce adhesion between cells because VEGFR2-VEGF binding causes endocytosis of VE-cadherin [167]. This reduced adhesion may enable cells with high VEGFR2 levels, such as tip cells, to migrate to the sprout tip [140]. Because of this complex interplay between between cell behavior and Dll4, Notch, VEGF, and the VEGF receptors, future studies will replace the simplified tip cell selection model for a tip cell selection model with explicit levels of Dll4, Notch, VEGF, VEGFR1 and VEGFR2, and link those levels directly to tip and stalk cell behaviors. Furthermore, future studies should include explicit levels of Apelin and APJ to study if and how VEGF-induced Apelin secretion affects network formation. Such an extended model will provide more insight into how the interaction between stalk cell proliferation [15, 168], ECM association of VEGF [169], and pericyte recruitment and interaction [102, 168], which all have been linked to Apelin signaling and/or VEGF signaling, affects angiogenesis.

4.4   Materials and methods

4.4.1   Cellular Potts model

In the cellular Potts model [84, 85] cells are represented on a finite box $\Lambda \subset \mathbb{Z}^2$ within a regular square lattice. Each lattice site $\vec{x} \in \Lambda$ is associated with a cell identifier $\sigma \in \mathbb{Z}^{\{+,0\}}$. Lattice sites with $\sigma = 0$ represent the extracellular matrix (ECM) and groups of lattice sites with the same $\sigma > 0$ represent one cell. Each cell σ has a cell type $\tau(\sigma) \in \{\text{ECM,tip,stalk}\}$. The balance of adhesive, propulsive and compressive forces that cells apply onto one another is de-

scribed using a Hamiltonian,

$$H = \underbrace{\sum_{(\vec{x},\vec{x}')} J(\tau, \tau')(1 - \delta(\sigma, \sigma'))}_{\text{cell adhesion}} + \underbrace{\sum_{\sigma} \lambda(\tau(\sigma))\left(a(\sigma) - A(\tau(\sigma))\right)^2}_{\text{area constraint}},$$

with $(\vec{x}, \vec{x}')$ a set of adjacent lattice sites, $\tau = \tau(\sigma(\vec{x}))$ and $\tau' = \tau(\sigma(\vec{x}'))$, $\sigma = \sigma(\vec{x})$ and $\sigma' = \sigma(\vec{x}')$, $J(\tau, \tau')$ the contact energy, the Kronecker delta: $\delta(x, y) = \{1, x = y; 0, x \neq y\}$, the elasticity parameter $\lambda(\tau)$, and the target area $A(\tau)$. To mimic random pseudopod extensions the CPM repeatedly attempts to copy the state $\sigma(\vec{x})$ of a randomly chosen lattice site $\vec{x}$, into an adjacent lattice site $\vec{x}'$ selected at random among the eight nearest and next-nearest neighbors of $\vec{x}$. The copy attempt is accepted with probability,

$$p_{\text{accept}}(\Delta H) = \begin{cases} 1 & \text{if } \Delta H \leq 0; \\ e^{\frac{-\Delta H}{f(\tau, \tau')}} & \text{if } \Delta H > 0; \end{cases}$$

with

$$f(\vec{x}, \vec{x}') = \begin{cases} \min(\mu(\tau), \mu(\tau')) & \text{if } \sigma > 0 \text{ and } \sigma' > 0; \\ \max(\mu(\tau), \mu(\tau')) & \text{otherwise.} \end{cases}$$

Here is $\mu(\tau)$ is the cell motility and $\tau = \tau(\sigma(\vec{x}))$ and $\tau\prime = \tau(\sigma(\vec{x}\prime))$ are short-hand notations. One Monte Carlo step (MCS) - the unit time step of the CPM - consists of $|\Lambda|$ random copy attempts; i.e., in one MCS as many copy attempts are performed as there are lattice sites in the simulation box.

The endothelial cells secrete a chemoattractant at rate $\alpha(\tau)$ that diffuses and decays in the ECM,

$$\frac{\partial c(\vec{x}, t)}{\partial t} = D\nabla^2 c(\vec{x}, t) + \alpha(\tau(\sigma(\vec{x})))(1 - \delta(\sigma(\vec{x}), 0)) - \varepsilon\delta(\sigma(\vec{x}), 0)c(\vec{x}, t),$$

with c the chemoattractant concentration, D the diffusion coefficient, and ε the decay rate. After each MCS equation 4.4.1 is solved numerically with a forward Euler scheme using 15 steps of $\Delta t = 2$s with absorbing boundary conditions ($c = 0$ at the boundaries of Λ); thus one MCS corresponds with 30 seconds. Chemotaxis is modeled with a gradient dependent term in the change of the Hamiltonian [90] associated to a copy attempt from $\vec{x}$ to $\vec{x}'$:

$$\Delta H_{\text{chemotaxis}} = -\chi(\tau, \tau') \left(\frac{c(\vec{x}')}{1 + sc(\vec{x}')} - \frac{c(\vec{x})}{1 + sc(\vec{x})} \right),$$

with $\chi(\tau, \tau')$ the chemoattractant sensitivity of a cell of type τ towards a cell of type τ' and vice versa, and s the receptor saturation. In the angiogenesis model we assumed that chemotaxis only occurs at cell-ECM interfaces (contact-inhibited chemotaxis; see [28] for detail); hence we set $\chi(\tau) = 0$ if $\tau \neq$ ECM and $\tau' \neq$ ECM. For the remaining, non-zero chemoattractant sensitivities we use the shorthand notation $\chi(\tau)$.

4.4.2   Tip cell selection model

The differentiation between tip and stalk cells is regulated by a simplified tip and stalk cell selection model. The model is based on lateral inhibition via Dll4-Notch signaling: If Dll4 binds to Notch on a adjacent cell it causes the dissociation of Notch, resulting in the release of Notch intracellular domain (NICD) [170]. We assume that tip cells express Notch at a permanent level of $\mathcal{N}(\text{tip})$ and Delta at a level of $\mathcal{D}(\text{tip})$; stalk cells express Delta and Notch at permanent levels of $\mathcal{N}(\text{stalk})$ and $\mathcal{D}(\text{stalk})$. The level of NICD in a cell, $\mathcal{I}(\sigma)$, is given by,

$$\mathcal{I}(\sigma) = \frac{\mathcal{N}(\tau(\sigma))}{a(\sigma)} \sum_{n \in \text{neighbors}} \mathcal{D}(\tau(n)) L_{\sigma \cap n},$$

in which $\mathcal{N}(\tau)$ and $\mathcal{D}(\tau)$ are the levels of Notch and Delta in a cell of type τ, and $L_{\sigma \cap n}$ is the length of the interface between cells σ and n. To model differentiation between the stalk and tip cell type in response to the release of NICD [57, 59] the cell type is a function of the cell's NICD level,

$$\tau(\sigma) = \begin{cases} \text{tip} & \text{if } \mathcal{I}(\sigma) \leq \Theta_{\text{NICD}}; \\ \text{stalk} & \text{if } \mathcal{I}(\sigma) > \Theta_{\text{NICD}}, \end{cases}$$

with Θ_{NICD} threshold representing the NICD-level above which the cell differentiates into a stalk cell. To prevent rapid cell type changes, we introduced a hysteresis effect by setting the Notch levels to: $\mathcal{N}(\text{tip}) = 0.3$ and $\mathcal{N}(\text{stalk}) = 0.5$. The Dll4 levels are set according to the experimental observation that tip cells express more membrane bound Dll4 than stalk cells [122]: $\mathcal{D}(\text{tip}) = 4$ and $\mathcal{D}(\text{stalk}) = 1$.

4.4.3   Morphometrics

To quantify the results of the sprouting simulations we calculated the compactness of the morphology and detect the lacunae, branch points and end points. The compactness C is defined as $C = A_{\text{cell}}/A_{\text{hull}}$, with A_{cell} the total area of a set of cells and A_{hull} the area of the convex hull around these cells. For the compactness we used the largest connected component of lattice sites with $\sigma > 0$. This connected component was obtained using a standard union-find with path compression [171]. The convex hull around these lattice sites is the smallest convex polygon that contains all lattice sites which is obtained using the Graham scan algorithm [172].

Lacunae are defined as connected components of lattice sites with $\sigma(\vec{x}) = 0$ (ECM) completely surrounded by lattice sites with $\sigma(\vec{x}) > 0$. These areas are detected by applying the *label* function of Mahotas on the binary image $\{\vec{x} \in \Lambda, 1_{\sigma(\vec{x})=0}\}$, i.e., the image obtained if medium pixels are set to 1 and

all other pixels are set to 0. The number of labels areas in this image is the number of lacuna, and the number of lattice sites in a labeled area is the area of a lacuna.

To identify the branch points and end points, the morphology is reduced to a single pixel morphological skeleton [173]. For this, first the morphology is obtained as the binary image $\left\{ \vec{x} \in \Lambda, 1_{\sigma(\vec{x})>0} \right\}$. Rough edges are removed from the binary image by applying a morphological closing [174] with a disk of radius 3. Then, 8 thinning steps are performed in which iteratively all points that are detected by a hit-and-miss operator are removed from the image [174]. In the skeleton, pixels with more than two first order neighbors are branch points and pixels with only one first order neighbor are end points. The skeleton may contain superfluous nodes. Therefore, all sets of nodes that are within a radius of 10 lattice units are collected and replaced by a single node at: $\vec{n}_{\text{merged}} = \langle \vec{x} \rangle_{\{\vec{x} \in \text{nodes}: |\vec{n} - \vec{x}| < 10\}}$.

All morphological operations are performed using the Python libraries Mahotas [175] and Pymorph [176]. Mahotas implements standard morphological operations, except for the closing and thinning operations required for skeleton generation. For these we use Pymorph, that implements a more complete set of morphological operation than Mahotas. However, as it is implemented in pure Python it is computationally less efficient than Mahotas.

4.4.4 Tip cell detection

Cells at the sprout tips were automatically detected in two steps: (1) detection of the sprouts in the network; (2) detection of the cells on the sprout tip. For the first step, detecting sprouts, a sprout is defined as a connection between a branch point, $\vec{B}$, and an end point, $\vec{E}$. To find the branch point $\vec{B}$ that is connected to end point $\vec{E}$, all nodes, except $\vec{E}$, are removed from the morphological skeleton (Figure 4.9**B**). In the resulting image one part of the skeleton is still connected to $\vec{E}$, this is the branch. Then, all nodes are superimposed on the image with the branch (Figure 4.9**C**) and the node connected to $\vec{E}$ is the branch point $\vec{B}$. Next, we search for the cells at the tip of the sprout, which are the cells in the sprout furthest away from σ_B. To find these cells we use a graph representation of the morphology. In this graph, $G(v, r)$, each vertex v represented a cell and vertices of neighboring cells shared an edge (Figure 4.9**D**). Now, we calculate the shortest path between each vertex v and the vertex belonging to the cell at the branch point v_B using Dijkstra's algorithm [177]. Then, we iteratively search for vertices with the longest shortest path to v_B starting at the vertex associated to σ_E (v_E). To limit the search to the a single sprout, the search is stopped when v_B is reached. When the search is finished, the node or nodes with the longest shortest path to v_B represent the cells or cells that are at the sprout tip.
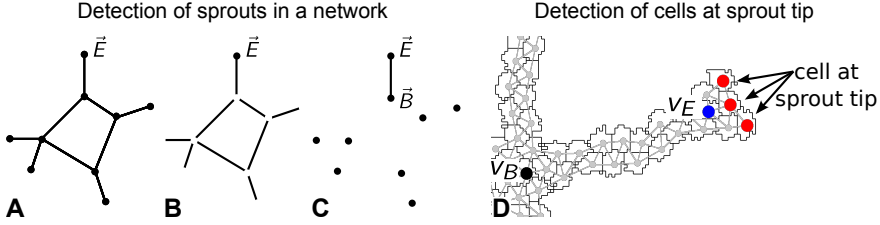
Figure 4.9: Detection of cells at the tips of sprouts. **A-C** detection of sprouts in a network. **A** Skeleton with branch points and end points. **B** Skeleton from which all nodes except $\vec{E}$ are removed. **C** The union of the nodes and the connected component in **B** that contains $\vec{E}$. The node that, in **C**, is part of the same connected component as $\vec{E}$ is the branch point $\vec{B}$. **D** detection of cells at the sprout tip (red vertices), which are farthest away from the branch point v_B (black vertex).

4.4.5 Model implementation and parameter sweeps

The simulations were implemented using the cellular Potts modeling framework *CompuCell3D* [178] which can be obtained from `http://www.compucell3D.org`. The simulation script is deposited in Supplementary File S1. File S1 also includes two extensions to *CompuCell3D*, called steppables, which we developed for the simulations presented in this paper. Steppable *RandomBlobInitializer* is used to initialize the simulations with a blob of cells, and steppable *TCS* contains the tip cell selection model. To efficiently set up, run and analyze large parameters sweeps including the ones presented in this paper, we have developed a pipeline to set up, run, and analyze large numbers of simulations of cell-based models on parallel hardware using software like *CompuCell3D*, described in detail elsewhere [179]. Briefly, the pipeline automatically generates simulation scripts for a list of parameters values, runs the simulations on a cluster, and analyzes the results using the morphometric methods described in sections 4.4.3 and 4.4.4.

4.4.6 *In vitro* sprouting assay

Immortalized human dermal endothelial cells (HMEC-1s) were cultured in 2% gelatin-coated culture flask at 37 °C under 5% CO_2 with a M199 medium (Gibco, Grand Island, NY, USA) supplemented with 10% foetal calf serum (Biowhittaker, Walkersvillle, MD, USA), 5% human serum and 1% Penicillin-streptomycin-glutamine (Gibco). The HMEC-1 cells used in this study were a kind gift of Prof. Dr. P. Hordijk (Sanquin, Amsterdam, the Netherlands). Cell suspensions were obtained from the cultures by TrypLE (Gibco) treatment of adherent endothelial cell monolayers. After the cells were extracted from the culture they were seeded in methylcellulose (Sigma-Aldrich) containing me-

dium to allow spheroid formation [180]. After 18 hours, the spheroids were embedded in a collagen gel containing human serum. In the period that these experiments were performed, the lab had to change collagen gels because of availebility issues. Therefore, the following three gels were used: Purecol bovine collagen (Nutacon, Leimuiden, the Netherlands), Nutacon bovine collagen (Nutacon, Leimuiden, the Netherlands), and Cultrex rat collagen I (R&D Systems, Abingdon, United Kingdom). The gels may be supplemented with VEGF-A (25 ng/ml). After 24h images of the sprouts were obtained using phase-contrast microscopy. Using ImageJ [181] with the NeuronJ plugin [182] the number of sprouts and the length of the sprouts in the image were counted.

To study sprouting in absence of tip cells, CD34 negative HMEC-1s [123] were extracted using Fluorescence-activated cell sorting (FACS). For this the cells were washed in PBS containing 0.1% bovine serum albumin. Cells were incubated with anti-CD34-phycoerythrin (anti-CD34-PE; clone QBend-10) and analyzed by flow cytometry on a FACSCalibur (Becton Dickinson, Franklin Lakes, NJ, USA) with FlowJo 6.4.7 software (Tree Star, San Carlos, CA, USA).

To inhibit Apelin signaling HMEC-1s were transfected with a silencing RNA (siRNA) against Apelin (siAPLN) or against the Apelin receptor APJ (siAPJ), and a non-translating siRNA (siNT) was used as a control. For each siRNA the HMEC-1s were transfected with 25 nM siRNA (Dharmacon, Lafayette, CO, USA) final concentration and 2.5 nM Dharmafect 1 (Dharmacon) for 6 hours using the reversed transfection method [183]. Transfection efficiency was evaluated with qPCR and a knockdown of RNA expression above 70% was considered as an effective transfection. The significance of each treatment was analyzed in a two-step procedure. First, groups in which the means differ significantly were identified with analysis of variance (ANOVA). Second, for the groups with different means, the results of the siAPJ and siAPLN treatments are compared to the results of the siNT treatment using Tukey's range test [184, 185].

4.A Supplemtentary movies

An archive containing all supplementary movies can be found at
`http://persistent-identifier.org/?identifier=urn:nbn:nl:ui:18-22537`.

Movie S1 Cells aggregate instead of forming a network with 20% predefined tip cells and $J(\text{tip,ECM}) = 5$.

Movie S2 Close up of tip cells on the side of a branch that cause network expansion. For this simulation the 20% of the cells were predefined as tip cells with $\chi(\text{tip}) = 400$.

Movie S3 Selected tip cells do not pull apart the network in a simulation with $\Theta_{\text{NICD}} = 0.1$ and $\chi(\text{tip}) = 200$.

Movie S4 Sprouting is strongly inhibited for $\Theta_{\text{NICD}} = .2$ and 90% inhibition of Apelin secretion ($\alpha(\text{tip}) = 10^{-3}\text{s}^{-1}$ and $\alpha(\text{stalk}) = 10^{-4}\text{s}^{-1}$).

Movie S5 When the model is adapted for Apelin, 'predefined' tip cells get surrounded by stalk cells. For this simulation 10% of the cells were predefined as tip cells with $\chi(\text{tip}) = 400$ and $\alpha(\text{tip}) = 0.01$.

4.B Supplementary files

File S1 Simulation script and code needed to run the simulations in the CPM modeling framework *CompuCell3D* [178]. The simulation script (angiogenesis.xml) can be used when the two CC3D steppables, RandomBlobInitializer and TCS, are compiled and installed. RandomBlobInitializer is needed to initialize a simulation with a circular blob and this steppable may be replaced with CC3D's BlobInitializer. TCS is the steppable that runs the Dll4-Notch genetic network and should be omitted to run simulations with predefined tip cells. This file can be found at `http://persistent-identifier.org/?identifier=urn:nbn:nl:ui:18-22538`.

4.C Supplementary tables

	Exp. 1	Exp. 2	Exp. 3	Exp. 4	Pooled
siAPLN	up	no effect	down	down	down
siAPJ	no effect	down	down	down	down
siAPLN+VEGF	down	down	down	down	down
siAPJ+VEGF	down	no data	down	down	down

Table S1: Overview of the effects of siAPJ and siAPLN on sprouting of spheroids with mixed cells for each individual experiment. Effects considered to be significant if $p < 0.05$, see section 4.4.6 for details of the statistical analysis.

	Exp. 1	Exp. 2	Exp. 3	Exp. 4	Exp. 5	Pooled
siAPLN	down	down	no effect	up	up	no effect
siAPJ	down	no effect	down	no effect	no effect	down
siAPLN +VEGF	up	up	up	up	no effect	up
siAPJ +VEGF	no effect	up	up	up	up	up

Table S2: Overview of the effects of siAPJ and siAPLN on sprouting of spheroids with CD34- cells for each individual experiment. Effects considered to be significant if $p < 0.05$, see section 4.4.6 for details of the statistical analysis.

4.D   Supplementary figures
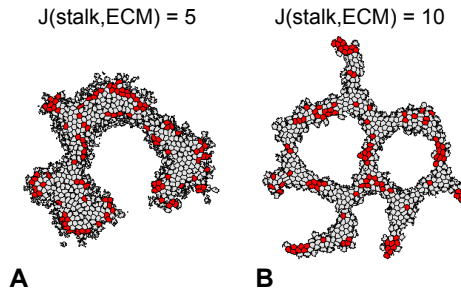
Figure S1: Effects of increasing ECM adhesion for stalk cells. **A** stalk cells that adhere more strongly to the ECM than tip cells will engulf tip cells. **B** stalk cells that adhere slightly more to the ECM than tip cells do engulf tip cells, because chemotaxis has the same effect on tip and stalk cells. **A-B** are the results of a simulation of 10 000 MCS with 20% tip cells.
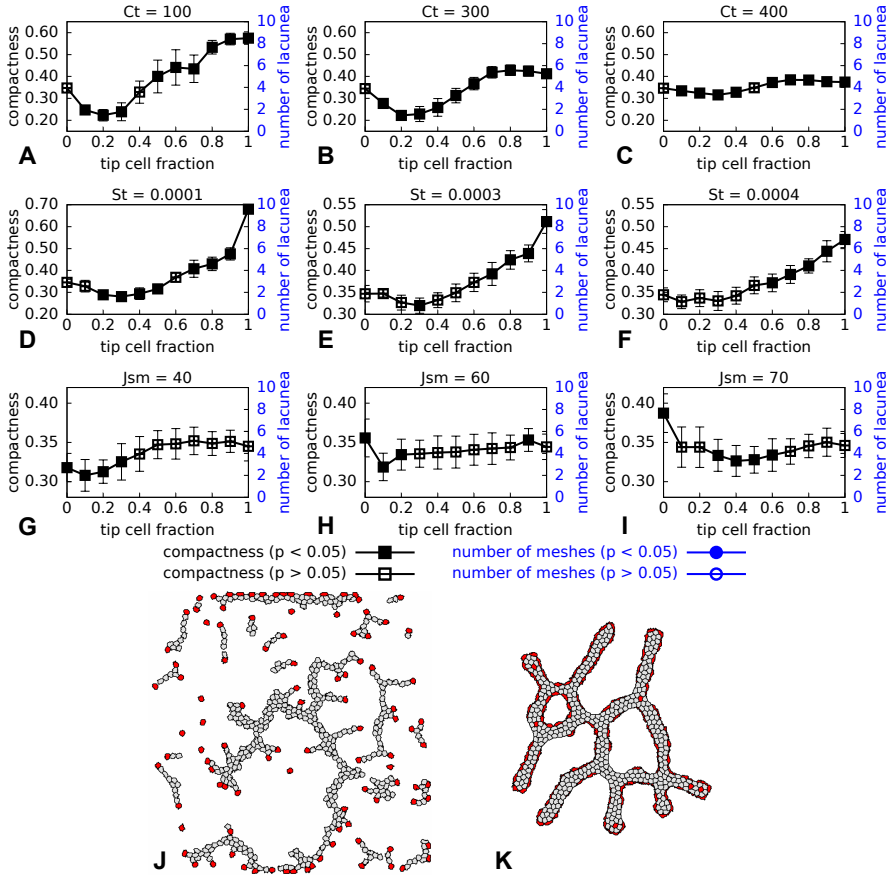
Figure S2: Effects of varying tip cell chemotaxis (**A**-**C**), tip cell chemoattractant secretion rate (**D**-**F**) and stalk-ECM adhesion (**G**-**I**). The morphometrics were obtained after 10 000 MCS and are the average of 50 simulations (error bars represent standard deviation). p-values were obtained with a Welch's t-test for the null hypothesis that the mean of the sample is identical to that of a reference where all cells have the default properties. **J** the network disintegrates with $\chi(\text{tip}) = 100$) and 20% tip cells. **K** tip cells over the network for $J(\text{stalk,ECM}) = 70$ and 20% tip cells.
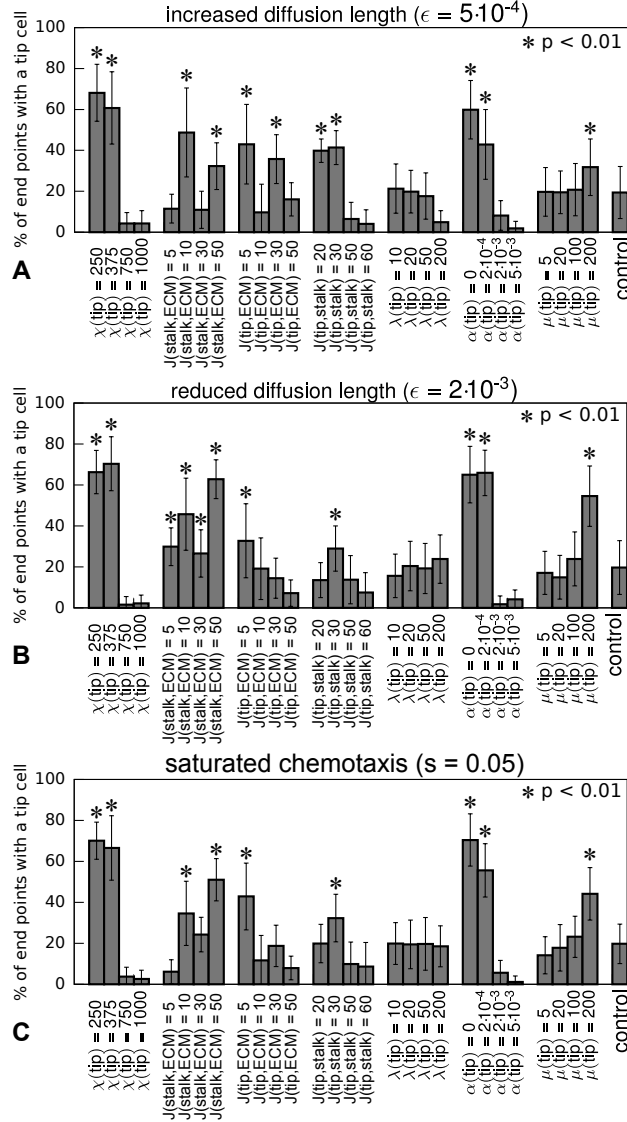
Figure S3: Differences in cell properties can enable cells of one type to occupy sprout tips for three alternative parameter sets. For **A** the decay rate was reduced, for **B** the decay rate was increased and for **C** receptor saturation was included in the model. The percentage of sprout tips occupied by at least one tip cell was calculated at 10 000 MCS. Error bars show the standard deviation over 50 simulations. In each simulation 20% of the cells were predefined as tip cells. For each simulation one tip cell parameter was changed, except for the control experiment where the baseline parameters were used for both tip and stalk cells. p-values were obtained with a one sided Welch's t-test for the null hypothesis that the number of tip cells at the sprout tips is not larger than in the control simulation.
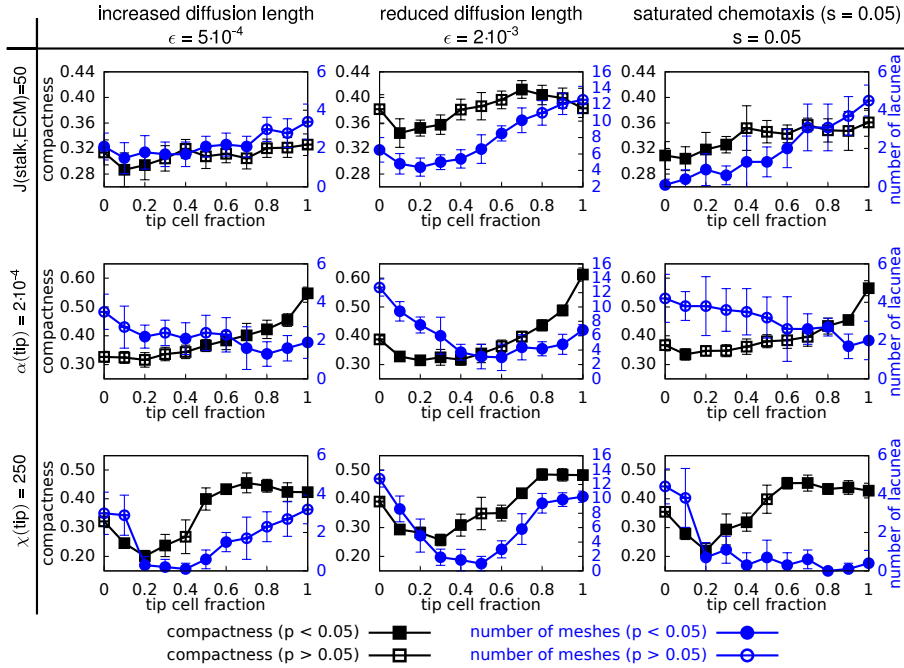
Figure S4: Effects of tip cells with $J(\text{stalk,ECM}$ (**A-C**), $\alpha(\text{tip})$ (**D-F**) or $\chi(\text{tip})$ (**G-I**) on the network morphology for the three alternative parameter sets. The morphometrics were obtained after 10 000 MCS and are the average of 10 simulations (error bars represent standard deviation). p-values were obtained with a Welch's t-test for the null hypothesis that the mean of the sample is identical to that of a reference sample in which all cells have the default properties.
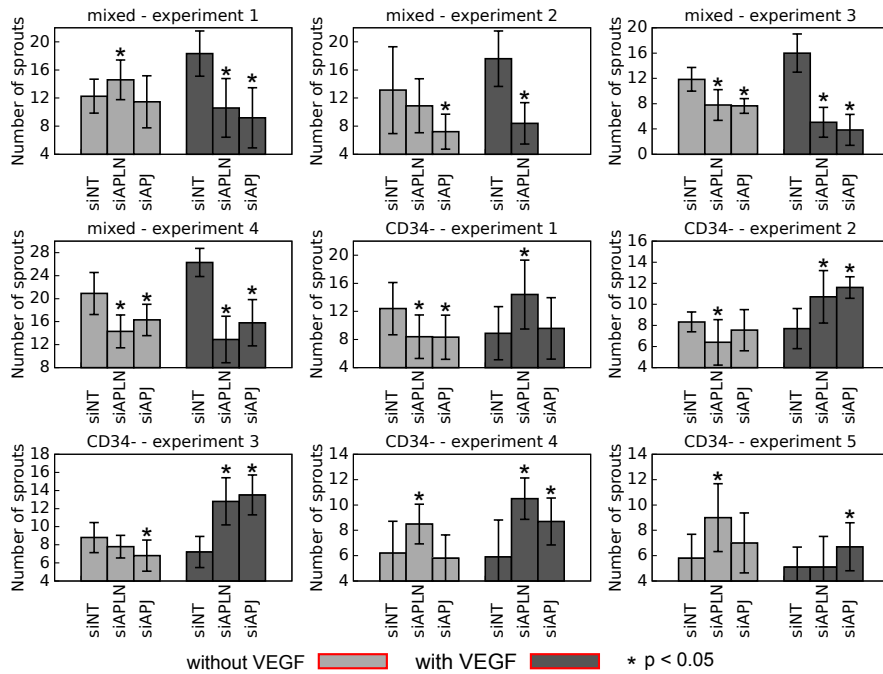
Figure S5: Effect of siAPJ and siAPLN on sprout lengths for all experiments. These metrics are the average of all the successfully cultured spheroids per experiments with the error bars depicting the standard deviation. The * denotes $p < 0.05$, see section 4.4.6 for details of the statistical analysis. Note that the experiments are done with different collagen gels: Purecol collagen (**A,E**), Nutacon collagen (**B, F, G**), and Cultrex rat collagen (**C, D, H, I**).

5

Large-scale parameter studies of cell-based models of tissue morphogenesis using *CompuCell3D* or *VirtualLeaf*

Abstract

Computational, cell-based models, such as the cellular Potts model have become a widely-used tool to study tissue formation. Most cell-based models mimic the physical properties of cells and their dynamic behavior, and generate images of the tissue that the cells form due to their collective behavior. Due to these intuitive parameters and output, cell-based models are often evaluated visually and the parameters are fine-tuned by hand. To get better insight into how in a cell-based model the microscopic scale (e.g., cell behavior, secreted molecular signals, and cell-ECM interactions) determines the macroscopic scale, we need to generate morphospaces and perform parameter sweeps, involving large numbers of individual simulations. This chapter describes a protocol and presents a set of scripts for automatically setting up, running and evaluating large-scale parameter sweeps of cell-based models. We demonstrate the use of the protocol using a recent cellular Potts model of blood vessel formation model implemented in *CompuCell3D*. We show the versatility of the protocol by adapting it to an alternative cell-based modeling framework, *VirtualLeaf*.

5.1 Introduction

To study the mechanisms of tissue morphogenesis, it is often useful to see a tissue as a swarm of interacting cells that follow a set of stereotypic or stochastic rules, which would be determined ultimately by their genome. The decisions of the cells are then guided by present and past interactions with adjacent cells and the micro-environment. In this view, tissue morphogenesis is a problem of collective cell behavior, in which tissues emerge, sometimes via non-intuitive mechanisms, from stereotypic or stochastic rules that the individual cells follow.

A useful computational tool for studying collective cell behavior is *cell-based modeling* [16, 186]. The inputs to a cell-based model are the behavioral rules that cells follow. The output of a cell-based model is the tissue morphogenesis that follows indirectly from the collective behavior of the individual cells. Cell-based models have been applied to a wide range of problems in developmental biology, including somitogenesis [87] , tumor development [187–190] liver regeneration [191], plant development [192, 193], epithelial branching [194], cystogenesis [195] and angiogenesis and vasculogenesis [25, 28, 33, 34, 40, 81]. In many cell-based models cell behavior is described at a phenomenological level, based on experimental observations. More recent approaches have introduced detailed models of genetic networks guiding cell behavior, see e.g. [87, 196]. These studies demonstrate the utility of cell-based modeling for elucidating the mechanisms of development.

Because most cell-based simulations cannot be solved analytically, insight into their behavior must be obtained using computer simulation. Individual simulations with visual output can give some initial intuition about the behavior and parameter sensitivity of the model. To obtain a more systematic overview of the range of behaviors the model can exhibit, and its sensitivity to parameters, it becomes necessary to rerun the simulation many times for different parameters, and, in case of stochastic models, to obtain statistical measures of the model results by rerunning many random instantiations of the model. If values for the model parameters cannot be determined experimentally, we must test the model for a range of experimentally plausible parameter values [28, 197]. And where parameter values are partly known, systematic parameter studies help predict the response of the system to pharmaceutical treatments [40, 81] or evaluate the behavior of a tissue. Thus, systematic parameter studies are a central tool for analyzing cell-based modeling.

As cell-based models become more complex and take longer to run, performing such parameter studies can become a challenging problem both in terms of computational power and in terms of data management. Here, we describe a protocol and release a set of Python scripts to automatically set up, run and analyze large parameter sweeps of cell-based models on desktop machines, computational clusters, or in the cloud. Although the protocol and parts of the scripts can be used with any kind of simulation tool that can be started from the command line, we illustrate the protocol in detail with a simulation of vasculogenesis (blood vessel formation; [25, 134]), developed using the cell-based simulation package *CompuCell3D* [178]. *CompuCell3D* is an implementation of the Cellular Potts Model (CPM) [84, 85], a widely used cell-based simulation method. The CPM is lattice-based technique that simulates the stochastic, amoeboid motility of biological cells in response to local cues from adjacent cells and diffusive signals, in this way making predictions on collective cell behavior. To illustrate that the parameter sweep can be applied to any kind of simulation tool with a command-line interface, we also show how to adapt the Python scripts to set up, run and analyze a parameter sweep for *VirtualLeaf* [192], which is an alternative cell-based modeling technique. Furthermore, we show how the protocol was adapted to set up parameter sweeps as part of a collaborative study of *in vitro* and *in silico* tumor growth.

5.2 Materials

The following materials and prior knowledge are required for using and extending the code provided in this protocol.

5.2.1 Python

To use *CompuCell3D*, and to run the *CompuCell3D* extensions and parameter sweep scripts presented in this chapter, you will use the programming language Python.

1. Download and install the latest version of the Python 2.x branch (see note 1 in section 5.A) from `http://www.Python.org/download/`. Alternatively, Linux users can install Python using their package manager.
2. Familiarize yourself with Python (see note 2 in section 5.A). We recommend `http://en.wikibooks.org/wiki/Non-Programmer's_Tutorial_for_Python_2.6` for readers with no programming experience and `http://docs.Python.org/2/tutorial` for readers with programming experience in other programming languages.

5.2.2 Cloud computing

Because cell-based simulation models typically take dozens of minutes to hours to complete, depending on the technique you use and the complexity of the model, we recommend using a computer cluster or a cloud computing service to run multiple simulations in parallel. You can acquire access to a computing cluster via your institute or use online services, like *Amazon Webservices* (`http://aws.amazon.com`). If you want to use a computer cluster, familiarize yourself with its usage.

5.2.3 *CompuCell3D*

CompuCell3D [178] offers an easy-to-use graphical user interface for setting up and running simulations. *CompuCell3D* is designed as a modular framework and can therefore easily be extended, either using Python or C++.

1. The Python scripts provided in this chapter require the most recent Numpy version. Download Numpy from `http://sourceforge.net/projects/numpy/files/`and install it (see note 3 in section 5.A) before installing *CompuCell3D*. This will prevent *CompuCell3D* from installing an older release of Numpy.
2. Download a suitable *CompuCell3D* installer from `http://www.compucell3d.org/SrcBin`. Currently installers are available for: Ubuntu Linux 64bit (10.04 and 12.04), OS X (10.5.8, 10.6 and 10.8) and Windows. If there is no installer for your operating system, build *CompuCell3D* from source: `http://www.compucell3d.org/CompilingCC3D` (see note 4 in section 5.A). When

you are installing *CompuCell3D* on a cluster, you may also need to compile *CompuCell3D* because of the absence of suitable installers or because you are not allowed to run an installer from your account. During the installation of *CompuCell3D* you must specify the installation directory, in the remainder of this chapter we will refer to this directory as CC3DPATH.

3. Familiarize yourself with the CPM [84, 85] and with *CompuCell3D*. A step-by-step tutorial explaining the CPM and how to set up and run simulations with *CompuCell3D* can be found in [178] and an overview of the functions of *CompuCell3D* functions can be found in the reference manual [198]. The *CompuCell3D* installation includes a variety of example models, which can be found in the directory "Demos" located in the installation directory of *CompuCell3D*.

5.2.4 *CC3DSimUtils*

As supplementary material to this book chapter, we provide a Python module *CC3DSimUtils*. This module can be used to visualize and analyze simulation results, and to set up simulations with *CompuCell3D*.

1. Create a project directory at any location. In this directory we will store all code, simulation scripts and results. We will refer to the path of this directory as PROJECTPATH.
2. Create a directory named "src" in PROJECTPATH.
3. Download and extract CC3DSimUtils.zip to the "src" directory. Make sure that the directory containing *CC3DSimUtils* is named "CC3DSimUtils". In the subdirectory "doc" of "CC3DSimUtils" you will find the documentation of *CC3DSimUtils* ("html/CC3DSimUtils.html").
4. Tell Python about the location of *CC3DSimUtils*. For a Python script that will be executed from the root of PROJECTPATH, insert the following commands to the beginning of the Python script:

```
import sys
sys.path.append("src/")
```

5. Alternatively, experienced users can add the path to *CC3DSimUtils* to the system variable PYTHONPATH.
6. Install the following packages, which are required for *CC3DSimUtils* (see note 5 in section 5.A):
   - **Scipy**: http://sourceforge.net/projects/scipy/files/ (see note 3 in section 5.A)
   - **Python imaging library (PIL)**: www.pythonware.com/products/pil/
   - **Mahotas**: http://luispedro.org/software/mahotas (see note 6 in section 5.A)
   - **Pymorph**: http://luispedro.org/software/pymorph.

Installation instructions for these packages can be found at their websites. Alternatively, use a Python package manager, such as setup_tools or pip. For example:

```
>> pip install pymorph
```

5.3   Methods

We illustrate the use of *CC3DSimUtils* using a model of vascular network formation based on the Cellular Potts model, which is implemented in *CompuCell3D*. The model is described in detail elsewhere [25, 134]. Briefly, the model captures the self-organization of endothelial cells into vascular network-like structures, based on the following assumptions: (a) endothelial cells have an elongated shape, they (b) adhere to one another, and (c) they move and rotate randomly [134]. In a variant of the model, chemotaxis speeds up network formation and increases the stability of the networks [25, 134].

  Overall, the presented workflow is as follows. We first organize the project directory with several subdirectories that will hold all code, simulation scripts, simulation data, images and analysis results. We then run the model once and analyze the dynamics of network formation. Next, we use this model as the basis for a parameter study: We show how to set up, perform and evaluate a parameter study using *CompuCell3D* and *CC3DSimUtils*. Finally, we illustrate the versatility of the parameter sweep protocol by adapting the Python scripts to the alternative cell-based modeling framework *VirtualLeaf* [192].

5.3.1   Organize Project directory

To organize the simulations, we create a project directory in which you store simulation and analysis scripts, raw simulation data, simulation images and analysis results. The structure of this directory is based on the structure suggested by Noble [199].

1. Create a project directory at any location, if you have not yet done so in section 5.2.4. From now on we will refer to the path to the project directory with PROJECTPATH. This directory will be used for all examples in this section.
2. Create the following subdirectories:
   - "src": holds all non-executable code, such as the *CC3DSimUtils* module;
   - "bin": holds all executable code, such as analysis scripts;
   - "scripts": holds all simulation scripts that will be used with *CompuCell3D*;
   - "log": holds text files that list parameter values and random seeds for automatically generated simulations;
   - "data": holds all raw simulation data;

- "images": holds all images that show the configuration of cells resulting from a simulation;
- "results": holds all data files and images resulting from analysis methods.

5.3.2 Run the *CompuCell3D* model from the command line

We run a simulation of the blood vessel formation model using the command line interface of *CompuCell3D*. By running *CompuCell3D* from the command line we can bypass the graphical user interface, which reduces simulation time. Furthermore, using the command line enables us to use a computer cluster, because clusters are usually unable to run a graphical interface. All commands provided in this section are designed to be executed from the root of the PROJECTPATH. When we refer to directories, we refer to subdirectories of PROJECTPATH.

1. Download the file "steppables.zip" from the supplementary materials and extract it to the "src" directory.
2. Download "longcells_chem.zip" from the supplementary materials and extract it to the "scripts" directory. The zip-file contains three files: a CC3DML file (".xml"), and Python file (extension ".py") and a "*CompuCell3D*" file (extension ".cc3d"). Together, these three files specify a single *CompuCell3D* simulation. Change the variable projectpath on line 5 of "longcells_chem.py" (in subdirectory "longcells_chem" of the "scripts" directory) to your PROJECTPATH. Windows users can either use the slash (/) or two backslashes (\\) in path definitions.
3. Run the simulation by typing the following in a terminal emulator (Linux and OS X) or Command Prompt (windows) (see notes 7 to 9 in section 5.A):
4. Linux and OS X

```
>> CC3DPATH/runScript.sh --noOutput -i PROJECTPATH/
    scripts/longcells_chem.cc3d
```

5. Windows

```
>> CC3DPATH\runScript.bat --noOutput -i PROJECTPATH\
    scripts\longcells_chem.cc3d
```

6. This may take up to ∼45 minutes.
7. Next we plot the simulation results, and combine the images for a number of time steps in a single figure. Download "longcells_chem_draw.py" and "default.ctb" from the supplementary materials. Save "longcells_chem_draw.py" in the "bin" directory and "default.ctb" in your PROJECTPATH. Run "draw_longcells_chem.py" (see note 10 in section 5.A):

```
>> python bin/longcells_chem_draw.py
```

93

| 00500 | 02000 | 05000 | 10000 |
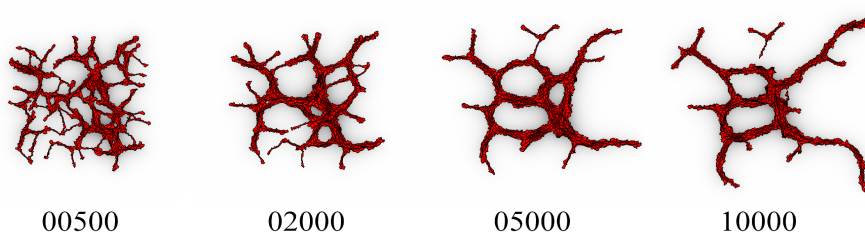
Figure 5.1: Morphologies at 500, 2000, 5000, 10 000 time steps, for a simulation with "longcells_chem".

The directory "longcells_chem" (subdirectory of "images") contains the morphologies of consecutive time steps, and the "results" directory contains a collage similar to Figure 5.1 ("longcells_chem.png") of the morphologies for 500, 2000, 5000 and 10 000 simulations steps combined. The morphologies are created with the function makeImages from *CC3DSimUtils*. This function draws images using the data files generated by the simulation. The function stackImages from *CC3DSimUtils* can be used to combine any set of images of the same size. See the *CC3DSimUtils* documentation for further details.

5.3.3 Analyzing a single *CompuCell3D* simulation

Now we have a set of simulation results and images. We next present a series of methods to quantify these simulation results.

1. Calculate the compactness of the vascular network simulations. The compactness is defined as: $\frac{A_{cells}}{A_{hull}}$; with A_{cells} the total area of the largest connected component and A_{hull} the area of the convex hull. The convex hull can be seen as the smallest "gift wrapping" around an object. Download "longcells_chem_compactness.py" from the supplementary materials, save it in the "bin" directory and run with:

```
>> python bin/longcells_chem_compactness.py
```

   The "results" directory will contain a tab-separated text file, "longcells_chem_compactness.data", which lists the compactness for every time step measured. A plot of this data should look similar to Figure 5.2.

2. Analyze where the elongated cells align with one another and where defects in alignment occur. To do so, we first quantify and visualize the relative orientations of the cells. Calculate an angle θ between the cell at a pixel $\vec{x}$ and the average orientation in the neighborhood of $\vec{x}$. The orientation of a cell, $\vec{v}$, is the orientation of the long axis of that cell. Assuming
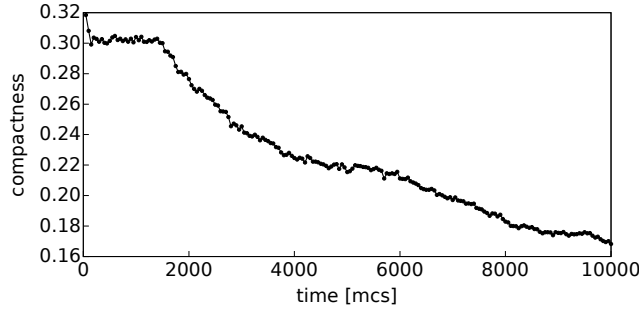
Figure 5.2: Time evolution of the compactness for a single simulation of "long-cells_chem".

that cells are close to elliptic, we can approximate $\vec{v}$ by the orientation of the eigen-vector corresponding to the largest eigen-value of the cell's inertia tensor. For a cell C, defined as the set of pixels with coordinates $\vec{x} = (x_1, x_2)$ that the cell occupies, the inertia tensor is defined as:

$$I(C) = \begin{pmatrix} \sum_{\vec{x} \in C} x_2^2 & -\sum_{\vec{x} \in C} x_1 x_2 \\ -\sum_{\vec{x} \in C} x_1 x_2 & \sum_{\vec{x} \in C} x_1^2 \end{pmatrix}.$$

The average cell orientation within a disk of radius r centered on $\vec{x}$ is called the *director*:

$$\vec{n}(\vec{x}, r) = \langle \vec{v}(\sigma(\vec{y})) \rangle_{\{\vec{y} \in Z^2 : |\vec{x} - \vec{y}| < r\}}.$$

The angle θ between the cell orientation $\vec{v}$ and the director $\vec{n}$ is a measure for local cell alignment:

$$\theta(\vec{x}, r)_{raw} = \cos^{-1} \left(\frac{|\vec{n}(\vec{x}, r) \cdot \vec{v}(\sigma(\vec{x}))|}{|\vec{n}(\vec{x}, r)||\vec{v}(\sigma(\vec{x}))|} \right).$$

Download "longcells_chem_alignment.py" from the supplementary materials, save it to the "bin" directory, and then run with:

```
>> python bin/longcells_chem_alignment.py
```

This script calculates θ for $r = 3$ at each pixel and plots it on the morphology. The script stores the resulting images in the subdirectory "long-cells_chem" of "images". It also creates a collage similar to Figure 5.3 ("longcell_chem_reldir_r=3.png" in "results"), which combines plots of θ for $r = 3$ at time steps 500, 2000, 5000 and 10 000.

3. The 2D nematic order parameter $S(r) = \langle \cos(2\theta(\vec{X}(\sigma), r)) \rangle_\sigma$, with $\vec{X}(\sigma)$ the center of mass of cell σ, quantifies the degree of local alignment in a morphology with a number between 0 and 1. $S(r) \to 1$ for cells aligning with

| 00500 | 02000 | 05000 | 10000 |
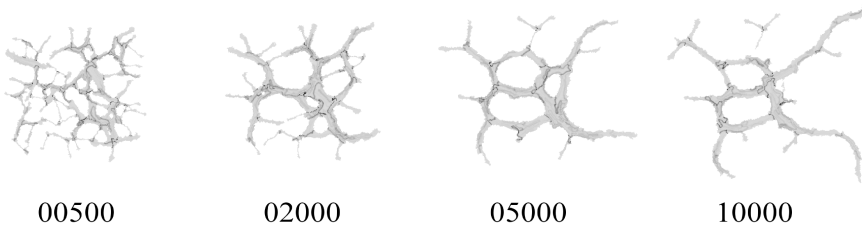
Figure 5.3: Angle θ between cells and the local director (for $r = 3$) mapped on the morphologies at 500, 2000, 5000, 10 000 time steps, for a simulation with "longcells_chem".

one other on overage over a distance r, and $S(r) \to 0$ for cells with random orientations. Download "longcells_chem_orderparameter.py" from the supplementary materials and save it in the "bin" directory. Run the script with:

```
>> python bin/longcells_chem_orderparameter.py
```

This script produces a file, named "longcells_chem_orderparameter.data", in the "results" directory that contains the order parameter for radii 20, 40 and 600 for every 250th time step. Note that radius $r = 600$ the disk covers the whole 400x400 simulation domain, so $S(600)$ becomes a *global order parameter*. Plotting the evolution of the order parameters should result in an image similar to Figure 5.4.
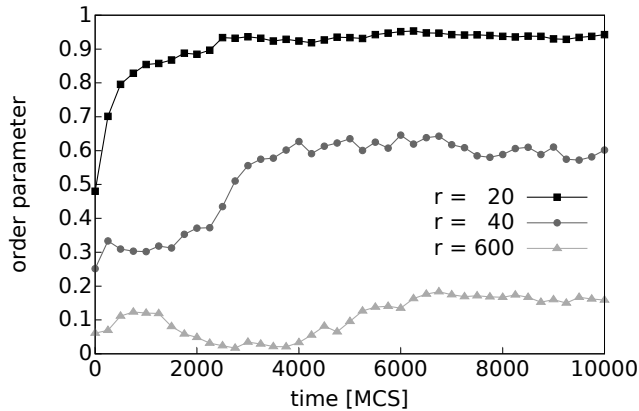
Figure 5.4: Time evolution of the order parameter for radii 20, 40 and 600 (global). for a single simulation of "longcells_chem".

5.3.4 Setting up and running a parameter sweep with CompuCell3D

We showed how to set up, run and analyze a single simulation using *CompuCell3D* and *CC3DSimUtils*. To gain insight into how specific parameters affect the model behavior, a model should be simulated repeatedly with different parameter values. In case of a stochastic model, such as the CPM, the simulation for each parameter value should be repeated multiple times to obtain good statistics. Here we show how to set up and run such a parameter sweep. First, we create a *driver* script that runs and analyzes a single simulation. Next, we show how to automatically create the simulation scripts for each parameter value and simulation repeat. In this example we vary the surface tension and turn chemotaxis on or off.

1. Download "driver.py" from the supplementary materials and save it a subdirectory of PROJECTPATH called "bin". The driver script runs a simulation (section 5.3.2) and analyzes the simulation results (section 5.3.3). Change the variables `projectpath` and `cc3dpath` in "driver.py" such that `projectpath` points to your PROJECTPATH and `cc3dpath` points to your CC3DPATH. For example, to run the driver script for "longcells_chem.cc3d" run the driver script with:

```
>> python bin/driver.py longcells_chem
```

   The concept of collecting all operations concerning a single simulation in one driver script can be applied to any modeling method that can be invoked from the command line.

2. (for cluster users) When a driver script is used on a cluster, you may also include commands to compress and pack the data to facilitate data transfer to your desktop machine. The command system in the Python module "os" can call the compression utilities from your driver script. To create a compressed archive containing all files starting with "longcells_chem_001-1" and ending with ".data", append the following line to the driver script:

```
os.system("tar -czf data_longcells_chem_001-1.tar.gz
    longcells_chem_001-1*.data")
```

3. To automatically set up the simulation, we use template simulation scripts. Download "templates.zip" from the supplementary materials and extract it in the root of PROJECTPATH. This will create a new folder named "templates" and in it you find four files: "longcells_chem.py", "longcells_chem.xml", "longcells_nochem.py" and "longcells_nochem.xml". The first two files serve as templates for the simulations with chemotaxis and the second two files serve as templates for the simulations without chemotaxis.

4. Automatically generate the scripts needed to run a *CompuCell3D* simulation. Download "preprocess.py" from the supplementary materials, save it

in the "bin" folder and run with:

```
>> python bin/preprocess.py
```

For each parameter value specified in 'preprocess.py' this script creates for each repeat: a *CompuCell3D* script, and a directory containing a CC3DML script and Python script in the "scripts" directory. For each simulation repeat a unique random seed is generated to ensure that each simulation is different (see note 11 in section 5.A). Each simulation is identified by an automatically generated simulation name, constructed as: [description]_[number]-[repeat]. We use the [description] to differentiate between simulations with and without chemotaxis: "longcells_chem" and "longcells_nochem". The three-digit simulation [number] is used to link a simulation to a parameter value. The [repeat] is a number that is used to set apart the simulation repeats. Besides the scripts for *CompuCell3D,* "preprocess.py" also generates log files (in the directory "log") that store the parameter values ("longcells_1-10.sim") and the random seeds ("longcells_1-10_10x.seed"). "preprocess.py" is specific for changing the surface tension in a set of templates. For other *CompuCell3D* models and/or other parameter sets, adapt "preprocess.py" using the functionality in the *Experiment* class of *CC3DSimUtils*. See the *CC3DSimUtils* documentation for more details.

5. (for cluster users) The simulations become faster if you save the simulation results on a section of the file system local to the node you are running on (often called *scratch space,* and move the data to your home directory when the simulation is finished. Point the variable datapath in "preprocess.py" to the scratch space, and add commands to the driver to copy the data back to your home directory. For this we recommend using the Python standard library modules *os* and *shutil*.

6. (for cluster users). The script "preprocess_cluster.py" automatically generates the job scripts needed to schedule the simulations on cluster using PBS [200]. Download "preprocess_cluster.py" from the supplementary materials to the "bin" directory, create a directory "clusterscripts" in PROJECTPATH, and run "preprocess_cluster.py":

```
>> python bin/preprocess_cluster.py
```

After running the script, there will be a number of PBS scripts in the "clusterscripts" directory and should look like:

```
#PBS -S /bin/bash
#PBS -lnodes=1:cores8:ppn=8
#PBS -lwalltime=8:00:00
cd \$HOME
python driver.py longcells_chem_001-1 > log/
    longcells_chem_001-1.out 2> log/longcells_chem_001
```

```
    -1.err &
...
python driver.py longcells_chem_001-8 > log/
    longcells_chem_001-8.out 2> log/longcells_chem_001
    -8.err &
wait
```

Submit the job script with "qsub" to add the run to the queue on the cluster. Each PBS script contains 8 jobs and requests an 8-core node (see Note 12 in section 5.A) . To change these parameters, change the variables cores and ppn in "preprocess_cluster.py". You may also need to modify the function createPBS in "CC3DPipeline.py" in *CC3DSimUtils* to fit the hardware and scheduling software of the cluster you are using.

7. When all simulations are finished we have a collection of raw data files, data analysis results and images. For each simulation all data files should be located in the "data" directory, in a subdirectory with the simulation name, for example: "PROJECTPATH/data/longcells_chem_001-1/". Similarly, the images are expected to be in a subdirectory with the simulation name in the directory "images": "PROJECTPATH/images/longcells_chem_001-1/". If this is not the case, move your data files and/or images to these locations.

5.3.5   Analyzing a *CompuCell3D* parameter sweep

After running the parameter sweep we have raw data, data analysis results and images for each simulation. Here we show how to collect and present this data.

1. Create a *morphospace*, a collage of simulated morphologies as a function of one or two simulation parameters. Download "postprocess_morphospace.py" from the supplementary materials, save it to the "bin" directory, and run it with:

```
>> python bin/postprocess_morphospace.py
```

Now, you should find an image named "longcells_1-10_morphospace_100000.png" in the "results" folder, which should look similar to Figure 5.5. The morphospace is created with the function morphImages, from *CC3DSimUtils*. See the *CC3DSimUtils* documentation for more details.

2. Calculate the compactness as function of the surface tension. Download "postprocess_compactness.py" from the supplementary materials and save it in the "bin" directory. Run it with:
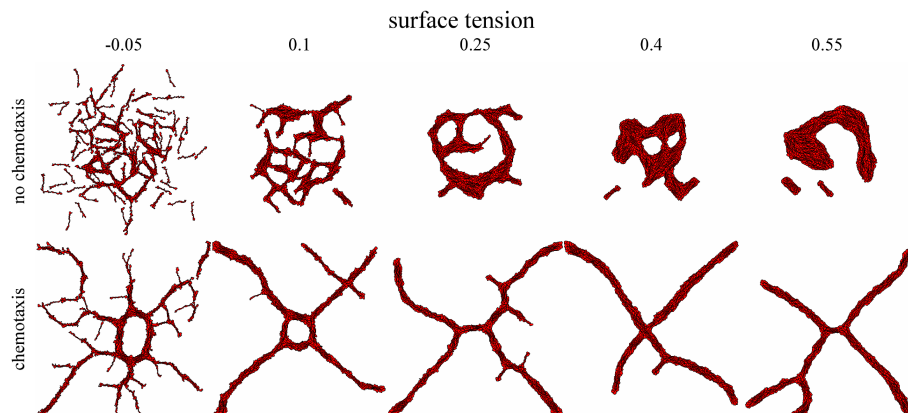
Figure 5.5: Morphospace showing the effects of varying surface tensions with and without chemotaxis.

```
>> python bin/postprocess_compactness.py
```

The script collects the compactness at the last time step of each simulation repeat for each tested parameter value and it calculates the mean and standard deviation over the simulation repeats. The results can be found in "longcells_chem_1-10_10x_compactness.data" (simulations with chemotaxis) and "longcells_nochem_1-10_10x_compactness.data" (simulations without chemotaxis) in the "results" directory. Plotting this data should result in a plot similar to Figure 5.6.
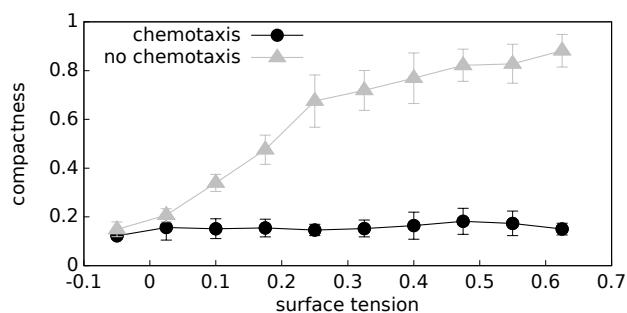
Figure 5.6: Compactness for simulations with and without chemotaxis, plotted against the surface tension. The compactness was calculated at 100 000 time steps, and for each parameter the simulation was repeated 10 times (error bars represent standard deviation).

3. Quantify the degree of cell alignment by calculating the mean and standard deviation of the order parameter. Download "postprocess_orderparameter.py" from the supplementary materials, save it into the "bin" directory and run the script with:

```
>> python bin/postprocess_orderparameter.py
```

This script calculates the mean and standard deviation the order parameter $S(r, t)$ as a function of time for radii $r = 20$ and $r = 40$, and the global order parameter ($r = 600$) for all simulation repeats of one surface tensions. The results can be found in "longcells_chem_003_10x_order parameter.data" and "longcells_nochem_003_10x_orderparameter.data", in the "results" directory. With the data in these files we generated the plot in Figure 5.7 for simulations of 1 000 000 time steps. Note that to reduce simulation time the scripts presented in this chapter produce only 100 000 time steps.
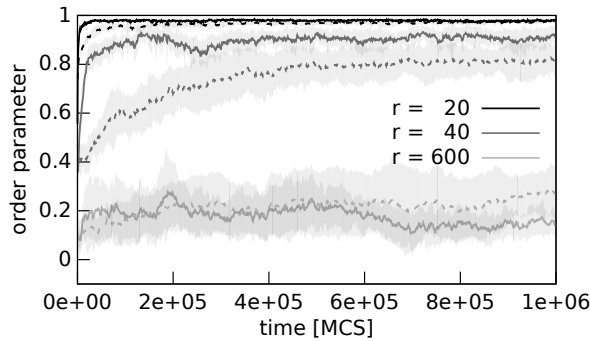
Figure 5.7: Time evolution of the order parameter for radii 20, 40 and 600 (global) for simulations with (solid) and without (dashed) chemotaxis. Each line represents the average order parameter of 10 simulations and the gray areas represent the standard deviation.

4. To relate cell motility to the degree of cell alignment, we detect clusters of aligned cells in the morphology. We loosely define a "cluster" as a set of cells aligned with the local director, $\theta(\vec{x}, r) < \theta$, with θ a threshold value. Clusters are separated from other clusters by regions with values of $\theta(\vec{x}, r) > \theta$ (dark gray regions in Figure 5.3). More formally, clusters are detected as follows:
   a) Define a binary matrix B of dimensions equal to the simulation domain.
   b) Assign a value of $B(\vec{x}) = 1$ to all cell pixels $\vec{x}$ for which $\theta(\vec{x}, r) < \theta$, with θ a threshold value and $B(\vec{x}) = 0$ for all other pixels.
   c) In B detect all connected components larger than 50 pixels. A set of cells forms a cluster if each cell overlaps with the same connected component in B for 50% of its area or more.

101

5. To study how aggregation of aligned cells in clusters affects cell behavior we measured the translation and rotation of the cells as a function of cluster size. The translational diffusion coefficient D_t quantifies the translational motility of cells. It is derived from the *mean squared displacement* (MSD) of a cell: $\langle|\vec{X}(\sigma, t) - \vec{X}(\sigma, 0)|^2\rangle_\sigma = 4D_t t$. The rotational diffusion coefficient D_r is derived from the *mean squared rotation* (MSR) of a cell: $\langle(\alpha(\sigma, t) - \alpha(\sigma, 0))^2\rangle_\sigma = 2D_r t$.

6. Calculate the translational and rotational diffusion coefficients. Download "postprocess_diffusion.py" from the supplementary materials, save it in the "bin" directory and run the script with:

```
>> python bin/postprocess_diffusion.py
```

This script creates time series of the MSD and the MSR of each cell as a function of the cluster size and uses those time series to calculate the translational and rotational diffusion coefficients. First, cells are binned according to cluster size for each time step, with a bin size of 5 cells and the first bin running from 2 to 5 cells. Then, the MSD and MSR of each cell are split into chunks of 10 consecutive time steps, during which that cell belonged to the same cluster size bin. Using these binned chunks the translational and rotational diffusion coefficients are calculated with a least square fit of respectively the MSD and MSR. The diffusion coefficients, together with the standard error of the estimate of the fit, are stored in "longcells_nochem_003_10x _diffusion.data" in the "results" directory. In Figure 5.8 we plot the translational and rotational diffusion coefficients calculated using data from time step 500 to 250 000 (similar to our previous work [134]). As mentioned before, the scripts presented in this chapter only produce 100 000 time steps in order to reduce simulation time.
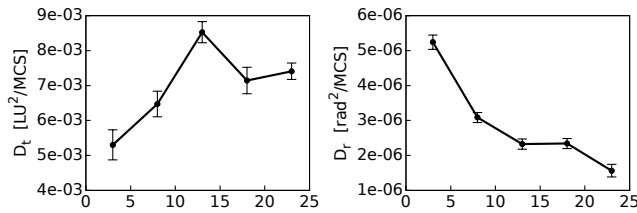
Figure 5.8: Diffusion coefficients as a function of the cluster size. **A.** translation diffusion coefficient and **B.** rotational diffusion coefficient. These diffusion coefficients were calculated from 10 simulations of 250 000 time steps. The error bars represent the standard error of the estimates of the least square fit.

5.3.6   Adapting the protocol to *VirtualLeaf*

The scripts described in sections 5.3.4 and 5.3.5 can be adapted to any sim-
ulation package that is 1) invoked from the command line and 2) for which
model parameters are specified in a text file. As an example, we show how
to use the scripts used in section 5.3.4 and 5.3.5 to set up, run and analyze
for the cell-based, vertex-based modeling framework *VirtualLeaf* [192, 201].
A model in the *VirtualLeaf* is defined by a so-called *plugin* and the model pa-
rameters are defined in a so-called *leaf* file. With the *leaf* file and the *plugin*,
VirtualLeaf can be invoked from the command line. Thus, *VirtualLeaf* meets
both of the requirements of the parameter sweep protocol.

1. Create a project directory for your *VirtualLeaf* project (as described in sec-
   tion 5.3.1).
2. Adapt "driver.py" to run and analyze *VirtualLeaf* simulations.
   a) To run the simulation, "driver.py" uses the function os.system (on line
      26), which attempts to execute its argument on the command line. For
      example, for a *VirtualLeaf* model defined in "plugin.cpp" and the pa-
      rameters defined in "leaf.xml", this argument must be (see note 13 in
      section 5.A):

```
/path/to/VirtualLeaf/bin/VirtualLeaf -b -l leaf.xml
    -m libplugin
```

   Assign the path to the VirtualLeaf executable to execpath (line 7) and
   assign the executable name, *i.e.*, "VirtualLeaf" to executable (lines 10-
   11) . Next, define a new variable named plugin, before line 26, that
   points to the plugin in which your model is defined (*e.g.*, 'libplugin').
   Now, change line 26 to:

```
os.system('execpath'+'/'+executable+' -b -l '+
    projectpath+'/scripts/'+id+'.xml -m '+plugin)
```

   b) Remove the commands on line 28 and further, and replace them with
      calls to your own analysis functions.
3. Create a template *leaf* file for your model that contains the default param-
   eter values for your model.
4. Create a new Python script to automatically generate *leaf* files, based on
   "preprocess.py".
   a) Copy line 1 of "preprocess.py" to import the necessary Python libraries.
   b) Create a function buildLeafFile to change specific parameter values
      in a template *leaf* file. Because *leaf* files are based on XML, you can
      use "Experiment.py" as an example on how to adapt an XML file using
      Python. Besides changing specific parameter values, buildLeafFile
      also assigns a random seed, sets the intervals at which the simulation
      generates graphical and numerical output, and it sets the file names

and location of the output. As with the *CompuCell3D* simulations, model output files should be identified by the simulation description, simulation number and repeat number: description_number-repeat, and be stored in a directory with the same name in the "data" directory of PROJECTPATH.

c) Define a variable projectpath (see line 47 of "preprocess.py"):

```
projectpath = [PROJECTPATH]
```

replacing [PROJECTPATH] for your PROJECTPATH.

d) Define the parameters of the parameter sweep. These are simname for the simulation description, offset for the first simulation number, repeats for the number of repeats, and rep0 for the first repeat number (see lines 51-58 of "preprocess.py"). For example:

```
simname = 'leaf'
offset = 1
repeats = 10
rep0 = 1
```

e) Set the simulation time (simtime) and the frequency at which output is generated (savefreq) (see lines 59-62 of "preprocess.py"). For example:

```
simtime = 1000
savefreq = 25
```

f) Create a list of parameter values, named par, that will be tested in the parameter sweep (see line 64 of "preprocess.py").

g) Create output files for simulation settings and seeds, and write the file headers (see lines 70-76 of "preprocess.py"):

```
runid = simname+'_'+str(offset)+'-'+str(offset+len(
    par)-1)
# open log file for parameter values
out = open('log/'+runid+'.sim','w')
out.write('\#id\tPARAMETERNAME')
# open log file for random seeds
sout = open('log/'+runid+'_'+str(repeats)+'x''.seed
    ','w')
sout.write('\#id\tseed')
```

h) Iterate over the parameters and the simulation repeats (see lines 79-101 of "preprocess.py"). The outer loop is used to write the tested parameter values to the log files. In the inner loop the random seed is generated and the *leaf* file is created:

```
seeds = []
for i,p in enumerate(par):
  out.write('\n'+name+'_'+string.zfill(i+offset,3)+
      '\t'+str(p)+'\n')
  for n in range(rep0,repeats+rep0):
    simid = name+'_'+string.zfill(i+offset,3)+'-'+
        str(n)
    seed = random.randint(1,10**9)
    # check if seed is unique
    while seed in seeds:
      seed = random.randint(1,10**9)
    seeds.append(seed)
    sout.write('\n'+simid+'\t'+str(seed))
    #--- Create leaf file ---\#
    buildLeafFile(...)
```

5. Adapt "preprocess_cluster.py" to create a set of scripts for the PBS job
   scheduler.
   a) Change numlist (line 7) such that it represents the ranges from the
      lowest simulation number to the highest simulation number.
   b) Change replist (line 9) such that it represents the range from the
      lowest repeat number to the highest repeat number.
   c) Replace basename (line 13) with your simulation description.
   d) Change cores (line 17), ppn (line 19) and runtime (line 21) to fit the
      type of node, number of processors per node and simulation time you
      will request on the cluster.
   e) Replace line 25 with:

```
joblist = [name+'_'+string.zfill(num,3)+'-'+str(n)
           for name in simnames
           for num in numlist for n in replist]
```

6. Depending on the analysis performed in the driver script, create your own
   set of post-process scripts. For this, you can use post-process scripts from
   section 5.3.5 as examples:
   • "postprocess_morphospace.py" can be used as an example for creating
     morphospaces;
   • "postprocess_compactness.py" can be used as an example to collect
     values for one time point per simulation, and mapping that data on pa-
     rameter values;
   • "postprocess_orderparameter.py" can be used as an example on how to
     collect time course data for multiple simulations.

5.4 Case study - Mammary epithelial spheroid morphogenesis

We applied the protocol described in this chapter in a collaborative, computational study on the growth of epithelial spheroids *in vitro*. These spheroids develop from mammary epithelial cells and are used as a model for breast cancer development. Wild-type mammary epithelial cells (WT) form a small spheroid by dividing randomly (Figure 5.9**A**-**B**) [202]. The cells on the inside of the spheroid stop dividing, while the cells on the outside keep on dividing (Figure 5.9**C**). The outside cells may become polarized cells that only divide perpendicular to the spheroid surface, while the other cells on the spheroid surface keep on dividing in random randomly (Figure 5.9**D**) [203]. Eventually, the cells on the inside die, resulting in a lumen (Figure 5.9**E**-**F**) [203], and the polarized cells stop dividing, stabilizing the spheroid [204]. When mammary epithelial cells overexpress human epidermal growth factor receptor 2 (HER-2), large spheroids with a minimal lumen develop [202–204]. The aim of the study is to find how the probabilities of proliferation, polarization and apoptosis is changed in HER-2 cells in comparison to wild-type cells. To this end we developed a cell-based model that reproduces epithelial spheroid formation with WT epithelial cells. Then, try to identify the differences between WT and HER-2 cells by varying the proliferation, polarization and apoptosis probabilities in the model.

  In this section we describe the model and quantification methods. Then, we show how we adapted our protocol to set up a parameter sweep that is used to setup the spheroid formation model for WT cells. An extensive discussion of the results and description of the further steps in this study are outside the scope of this section.
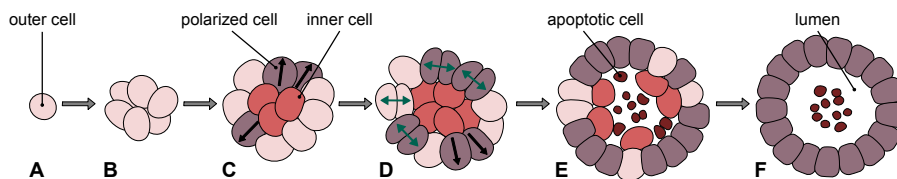
Figure 5.9: Development of an epithelial spheroid. **A**-**B** a single outer cell (pink) divides to form a cluster of outer cells. **C** outer cells that lose contact with the ECM become inner cells (red) and outer cells may become polarized cells (purple-gray). **D** outer cells divide in random directions, while the polarized cells divide perpendicular to the spheroid surface. **E**-**F** inner cells may enter apoptosis (burgundy cells) resulting in the formation of a lumen, and polarized cells become stabilized cells that do not divide. (This image is adapted from an image that was kindly provided by Floriane Lignet.)

5.4.1 Model of epithelial spheroid formation

The development of epithelial cell spheroids is modeled using the cellular Potts method [84, 85]. In this method the different cellular phenotypes that manifest during spheroid development are modeled explicitly, as well as transitions between the types and proliferation. The cell types involved in the spheroid development are: *outer, inner, polarized, stabilized* and *apoptotic*. Besides these biological cell types, two extra tissue types are added to represent *ECM* and *lumen*. All cells, except stabilized cells, can transition into another cell type, or proliferate (Figure 5.10). Outer cells can become inner cells or proliferate. Polarized cells can also become inner cells and proliferate, and they can become stabilized cells. Inner cells can become apoptotic cells and apoptotic cells die and become lumen. Both the type transitions and proliferation occur with a probability *p*, but only if the cells' environment fits a set of conditions. For this the environment of a cell, identified by σ, is characterized by the fraction of cell membrane M the cell shares with certain cell types:

$$\mathrm{M}(\sigma, \mathrm{types}) = \sum_{\tau \in \mathrm{types}} \frac{P_{\sigma \cup \tau}}{P(\sigma)}$$

with $P_{\sigma \cup \tau}$ is the length of the perimeter that cell σ shares with cells of type τ and $P(\sigma)$ is the total perimeter of cell σ. In the model there are three of these fractions defined: the fraction of the membrane shared with ECM ($\mathrm{M}(\sigma, \{\mathrm{ECM}\})$), the fraction of the membrane shared with lumen ($\mathrm{M}(\sigma, \{\mathrm{lumen}\})$), and the fraction of membrane shared with cells ($\mathrm{M}(\sigma, \mathrm{cells})$ with cells={outer, inner, polarized, stabilized, apoptotic}). Figure 5.10 shows the criteria for $\mathrm{M}(\sigma, \{\mathrm{ECM}\})$, $\mathrm{M}(\sigma, \{\mathrm{lumen}\})$, and $\mathrm{M}(\sigma, \mathrm{cells})$ for each transition and proliferation.

5.4.2 Quantification of spheroid morphology

To quantitatively compare the morphologies formed by the model with *in vitro* spheroids we compute several *shape indexes*: solidity, cell to hull ratio, and core factor. The solidity *s* measures how similar the shape of the spheroid is to a circle. For this we divide the radius (r_A) of a circle with the area of the spheroid (A) by the radius (r_P) of a circle with the perimeter of the spheroid (P):

$$s = \frac{r_A}{r_P} \quad \text{with} \quad r_A = \frac{A}{\pi} \quad \text{and} \quad r_P = \frac{P}{2\pi}.$$

The cell to hull ratio (CTH) measures the convexity of the spheroids; the higher the CTH the more convex the spheroid. For this we compute the ratio of the spheroid area (A) and the area of the convex hull around the spheroid
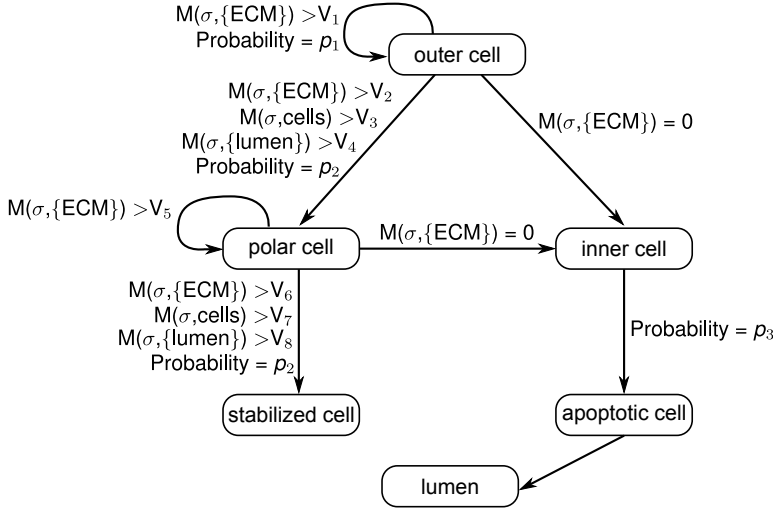
Figure 5.10: Flowchart of the cell type transitions.

(A_{hull}).

$$c = \frac{A}{A_{hull}}$$

The core factor is used to quantify the relative size of the lumen by computing the ratio of the lumen area (A_{lumen}) and the spheroid area (A).

$$f = \frac{A_{lumen}}{A}$$

All of these metrics were computed with Matlab and the Image Processing Toolbox.

5.4.3 Parameter identification

To identify the transition conditions for which the model reproduces experimental observations we performed a parameter sweep. There are 4 transition rules with eight transition parameters: $V = \{V_1, V_2, V_3, V_4, V_5, V_6, V_7, V_8\}$. Because each V represents a fraction of the cell membrane, the sum of V's in one transition condition (Figure 5.10) can never be larger than one. From these we derive the following limitations for V:

$$
\begin{aligned}
V_1 &\leq 1 \\
V_2 + V_3 + V_4 &\leq 1 \\
V_5 &\leq 1 \\
V_6 + V_7 + V_8 &\leq 1
\end{aligned}
$$

For the parameter sweep we generate 10 000 sets V. Each value was randomly drawn from a uniform distribution on the interval $[0, 1]$, and sets that did not obey Equation 5.4.3 were disregarded and replaced by a newly generated set. For each set of V ten simulations are preformed with different random seeds.

Because the model is implemented in *CompuCell3D*, with *Python* steppables for the type transitions, proliferation and apoptosis, we can easily adapt the scripts used in section 5.3.4. In our previous work the number of simulations was limited to a couple of hundreds and therefore creating simulation files for each simulations was not an issue. In contrast, here we have 100 000 simulations and therefore we chose to adapt the protocol to generate simulation scripts on the fly. For this we automatically generate a list of 10 000 sets V and use each line as an input for the driver script. The driver script then finds and replaces the parameter values in the simulations scripts. Besides generating simulation scripts on the fly, the protocol for setting up and running the simulations was similar to those previously described in section 5.3.4. For the morphological analysis we did not use *CC3DSimUtils*, but instead we used a Matlab script. Because it is quite complicated to run Matlab code on the cluster we used, the analysis was done for all simulations at once when all data was retrieved from the cluster.

Next, we visualize the results of the parameter sweep using scatter plots, which is typical first step in parameter identification [205]. Figure 5.11 shows these scatter plots in which each point represents the mean of the ten simulation repeats. Based on these graphs the effects of each parameter on the shape of the spheroid and the size of the lumen can be assessed. For example, V_5 seems to have the strongest influence on the lumen area: the higher V_5, the less lumen forms. More complex sensitivity analysis techniques [205] may be used to further analyze the results and find the best values for V. Then, this process can be repeated for the transition probabilities p_1, p_2, and p_3, to find how these parameters should be changed such that the model reproduces the HER2 spheroids.

Altogether, with this case study we showed that the protocol described in this chapter can easily be adapted for setting up a parameter identification study of a cell model. Finding the best values for V may require the use of more complex sensitivity analysis techniques [205]. When the values for V are identified, a similar parameter sweep can be performed for probabilities p_1, p_2, and p_3 to identify the differences between WT and HER-2 cells.
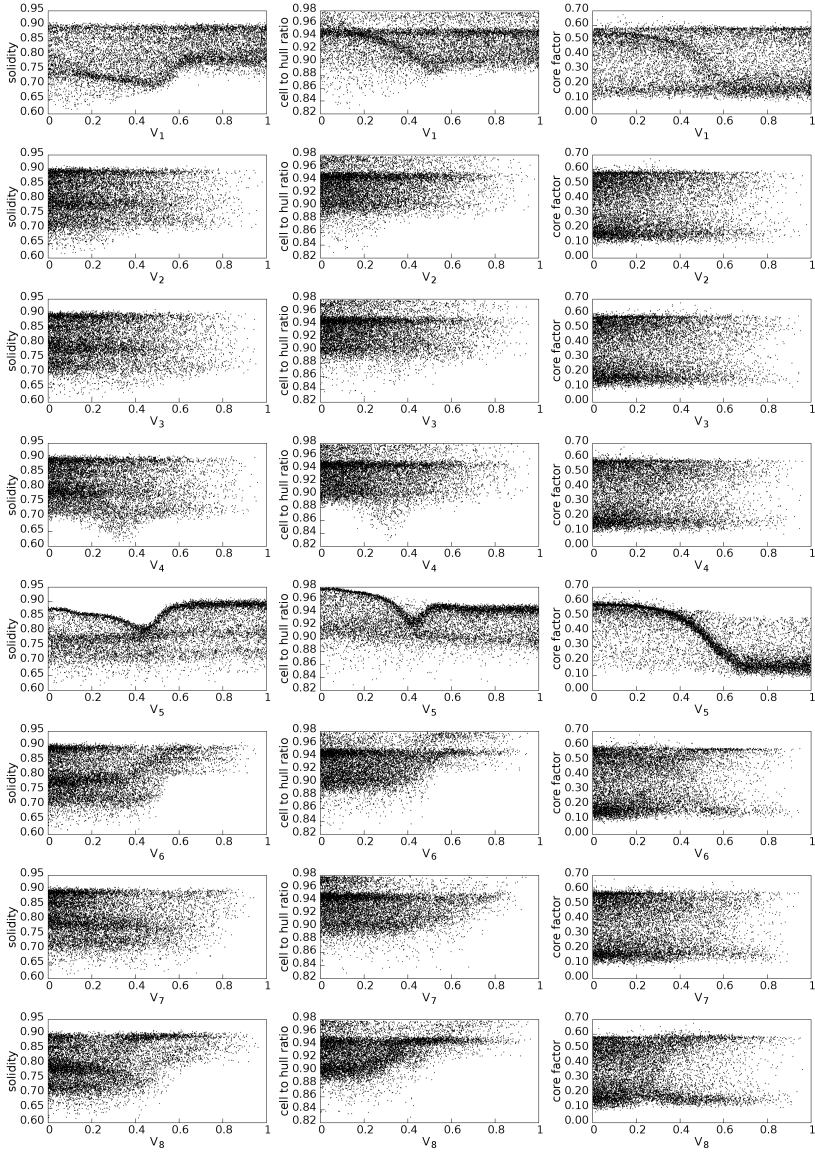
Figure 5.11: Effects of varying V_1-V_8 on the spheroid solidity, cell to hull ratio and compactness. Each point represents the mean of 10 simulations with identical values for V_1-V_8.

5.A   Notes

note 1 There are two Python branches: Python 2.x and Python 3.x, which are not fully compatible. All code supplied with this chapter and *Compu-Cell3D* is compatible with Python 2.6 and new versions of the Python 2.x branch.

note 2 Python uses indentation to delimit blocks of codes. In code that is copied from different sources, indentation may be broken due to different indentation lengths or mixing of tabs and spaces. See `http://www.Python.org/dev/peps/pep-0008/#indentation` and `http://www.Python.org/dev/peps/pep-0008/#tabs-or-spaces` for more information on how to correctly indent your code.

note 3 Windows users should install the Numpy or Scipy version that fits with your Python version. First check your Python version:

```
>> python -V
```

Note the first two digits of the Python version, e.g. *2.7*. Now go to the download page of Numpy or Scipy and select the latest version. Here you should find an installer that ends with your python version, e.g. "numpy-x.y.z-win32-superpack-python27.exe".

note 4 When you compile *CompuCell3D*, always check the *CompuCell3D* website for the most recent instructions and dependencies. Here we list some extra instructions for the compilation of *CompuCell3D*.
- The *CompuCell3D* developers recommend to use "cmake-gui", for systems without a graphical user interface the "cmake curses gui", also known as "ccmake", can be used as an alternative.
- Ensure that you compile *CompuCell3D* with the "release" flag because omitting this flag significantly increases simulation time. The "release" flag can be set with the "cmake-gui" or "ccmake".

note 5 *CC3DSimUtils* needs freetype fonts for the labels on images. You may need to install freetype (http://www.freetype.org/download.html) or change the variable fontpath in the function definitions of makeImage, stackImages and morphImages (all in "ImageUtils.py" in *CC3DSimUtils*).

note 6 For windows users we strongly recommend to download the installer for Mahotas at: `http://www.lfd.uci.edu/~gohlke/pythonlibs/`. Building the source of Mahotas, for example using pip, is not recommended.

note 7 *CompuCell3D* interprets all paths relative to its own path. Therefore, when running a simulation using runScript.sh you should specify the full path to the simulation file, for example

- Windows:
  `C:\Users\username\project_name\scripts\script.cc3d`
- Linux: `/home/username/project_name/scripts/script.cc3d`
- OS X: `/Users/username/project_name/scripts/script.cc3d`

note 8 On windows, running runScript.bat changes the working directory to the CC3DPATH. Make sure to change it back to the PROJECTPATH afterwards.

note 9 In this model we use a connectivity constraint to ensure that each cell consists of single connected component. Calculating the connected components is computationally expensive, therefore *CompuCell3D* only checks for local connectivity by checking if a cell is a single connected component within a small neighborhood. This can cause pixels to become *frozen*, because any change in their neighborhood breaks local connectivity. We fixed this by adding an extra test to the connectivity constraint for pixels that fit the pattern of a frozen pixel. We used this fixed connectivity constraint for all our simulation. This plugin ("ConnectivityFroNo.zip") can be downloaded from the supplementary materials and compiled as a part of the *CompuCell3D* developer zone, see the *CompuCell3D* developers' manual [206] for instructions.

note 10 On Windows the Python installation directory may not be in the $PATH, this results in an error like:

```
'Python' is not recognized as an internal or
    external command, operable program or batch file
    .
```

Adding the installation directory of Python to your $PATH system variable should solve this problem.

note 11 Random seeds are used to initialize a random generator. Every time a random generator is initialized with the same results, it returns the same sequence of pseudo-random numbers. Thus, if we run a *CompuCell3D* simulation twice with identical seeds, we get identical results. If no random seed is provided, *CompuCell3D* uses the current time to generate a random seed. When multiple simulations are started at the same moment, for example on a computer cluster, they will get the same seed. Thus, predefining random seeds has two advantages: 1) the results are reproducible; 2) the random seeds in parameter sweep are unique.

note 12 It is often more efficient to leave one core of a node idle. This core is then reserved for system processes while the remaining nodes are reserved for user processes, *i.e.* the simulations. To do so, set ppn

(processes per node) in "preprocess_cluster.py" to one less than there are cores (number of cores of the requested node).

note 13 Due to a bug in the current version of *VirtualLeaf* (1.0.1), if *VirtualLeaf* is invoked with both a *leaf* file and a *plugin* in which another *leaf* file is defined, the *leaf* file defined in the *plugin* will be used. To correct this problem, add the following code to "virtualleaf.cpp' after the line with "model_catalogue.InstallFirstModel();", and recompile:

```
if (leaffile){
   main_window->Init(leaffile);
}
```

5.B   Supplementary materials

All the supplementary materials can be found at
`http://persistent-identifier.org/?identifier=urn:nbn:nl:ui:18-22500`.

6

Discussion

6.1   Summarizing discussion

In this thesis we aimed to better understand why several types of cells with different behavior are involved in blood vessel formation. In particular, we studied how endothelial cells and pericytes interact during blood vessels formation (chapter 3), and we studied the role of tip and stalk cell differentiation of endothelial cells in angiogenesis (chapter 4). For this we used simple, cell-based, computational models. Such models can show how a multicellular tissue develops due to the collective behavior of single cells with cell-type specific behaviors and are therefore a good tool to study the role of specific cell types in angiogenesis. Whereas most previous modeling studies derived the modeled cell behaviors from experimental observations, we used our model to predict cell behavior that is sufficient for reproducing experimental observations. We chose this approach because it is often hard to infer the behavior of single cells from multicellular experiments in which the behavior of a cell is affected by the other cells and the cell's environment. This modeling approach requires model simulations for large ranges of parameter values. For this, we created a protocol for large scale parameter sweeps with cell-based models (chapter 5). While this protocol was developed with the cellular Potts method and the modeling framework *CompuCell3D* in mind, the method can easily be adapted for other modeling methods and corresponding software that can run without user interaction.

 Instead of building a new model for each of the topics we studied, we built upon two previous, computational angiogenesis models. In the first model, networks are formed by *elongated* cells that chemotact towards a chemoattractant secreted by all cells [25]. In the second model, round cells form networks due to *contact-inhibited* chemotaxis towards a chemoattractant that all cells secrete [28]. Before we can build upon these models, we must fully understand the mechanism that drives angiogenesis in each of the models.

In the contact inhibition model, angiogenesis is driven by two mechanisms. Initial sprouts form by the random movements of highly motile cells, or due to buckling caused by the inward force of chemotaxis on a volume conserved blob of cells. The chemoattractant gradient at the tips of these small sprouts is shallower than in between the sprouts and therefore new extensions are most likely at the sprout tips [28]. In contrast, for the model with elongated cells, it was not yet understood why these elongated cells form networks. Therefore, we studied how cell elongation can drive angiogenesis (chapter 2). For this we thoroughly analyzed the evolution of the networks and the behavior of individual cells using methods commonly used in liquid crystal theory. By analyzing the ordering of cells during pattern formation we showed that elongated cells tend to align along their long axis and this alignment is independent of chemotaxis. The clusters of cells that form due to alignment are limited in their rotation and this inhibits network collapse. These results suggest that cell elongation promotes the formation of branches and prevents merging of those branches.

 After we analyzed how elongated cells contribute to angiogenesis we used elongated cells in a model of that includes two cell types: endothelial cells and pericytes (chapter 3). Pericytes are perivascular cells that wrap around small blood vessels [97]. They are thought to stabilize blood vessels [97], but various studies indicated that pericytes also play a role during angiogenesis [69–71]. When endothelial cells and pericytes are combined in a vasculogenesis assay, a network is formed that quickly collapses and from the resulting blob of cells sprouts reappear. To identify the endothelial-pericyte interactions may cause this pattern formation we built an angiogenesis model that includes the two cell types and tested for what endothelial-pericyte interactions the model reproduces the *in vitro* pattern formation. The behavior of endothelial cells and pericytes were based on vasculogenesis assays with only one cell types. In these assays endothelial cells formed networks that resembled those formed with elongated cells and therefore they are modeled as elongated cells that secrete their own chemoattractant. Pericytes formed networks that quickly collapsed into blobs and these patterns can be reproduced by modeling pericytes as round cells that secrete their own chemoattractant. Based on the endothelial-pericyte interactions described in the literature, we proposed two signaling scenarios: paracrine signaling and contact-dependent signaling. In the paracrine signaling scenario endothelial cells secrete a chemoattractant for pericytes and vice versa. In the contact-dependent signaling scenario endothelial cells secrete a chemoattractant for pericytes, and endothelial cells that contact pericytes secrete a chemoattractant for endothelial cells. Then, we systematically varied the chemoattractant properties for both scenarios, using the protocol from chapter 5. With both signaling scenarios the model reproduced network formation

and network collapse, but only for the contact-dependent signaling scenario sprouting occurred after network collapse. These results suggest that endothelial cells and pericyte interact during angiogenesis via secreted chemoattractants.

Next, we studied the role of tip-stalk cell differentiation in angiogenesis to better understand why these two endothelial cell phenotypes are involved in angiogenesis. For this, we searched for cell behaviors that cause cells to lead and affect the resulting network morphology. We adapted the contact-inhibition model of angiogenesis to include both tip and stalk cells. Then, one by one, we varied the values of each parameter that controls tip cell behavior to find parameter values for which tip cells lead sprouts and affect angiogenesis. In this manner we found that when tip cells are less attracted to the chemoattractant secreted by all endothelial cells than stalk cells, these tip cells lead sprouts and affect angiogenesis. A study of published gene expression studies pointed towards Apelin as a candidate for this chemoattractant. Apelin is a chemoattractant for endothelial cells that is secreted by endothelial cells and the Apelin receptor, APJ, is only detected in stalk cells. Thus, Apelin is a chemoattractant for stalk cells and not for tip cells. We tested this hypothesis by inhibiting Apelin signaling in spheroid sprouting assays with either a wild-type population of endothelial cells, or a population of only stalk cells. In absence of tip cells, few sprouts develop in such sprouting assays. As we expected, Apelin inhibition reduced sprouting in spheroids with a wild-type endothelial cell population, while having little effect on spheroids with only stalk cells. These results suggest that Apelin could be a cause of the differential behavior of tip and stalk cells.

Altogether, we used cell-based models to study the role of cell mixing in angiogenesis. Specifically, we studied the interactions between endothelial cells and pericytes during angiogenesis, and the role of tip and stalk cell differentiation in angiogenesis. In both cases we used high-throughput simulations to explore the effects of cell behaviors or the properties of signaling molecules. In this manner we proposed that, during angiogenesis, endothelial cells and pericytes interact via diffusing molecules. Furthermore, we suggested that tip cell selection can stabilize network formation with tip cells, and we hypothesized that Apelin may be a cause of the differences in behavior of tip and stalk cells.

6.2   Future work

6.2.1   From abstract to realistic models

In this thesis we used relatively simple models to study the collective behavior of mixed cell types in angiogenesis. Such models provide a good tool to study the mechanisms by which several cell types affect angiogenesis. While

these model results can be compared with *in vitro* experiments on a qualitative level, as we did in chapters 3 and 4, comparing simulation results to experimental results at a quantitative level is often complicated. For example, when the proteins used for *in vitro* perturbations are not represented in the model, the *in vitro* perturbation must somehow be translated to a model parameter. This can only be done if the quantitative link between the protein and the model parameter is known, otherwise the model cannot be compared to experiments at a quantitative level. As a result, model validation is limited, as well as the predictive power of the models. Here we will discuss several improvements that would make the models presented in this thesis more realistic, and therefore more similar to *in vitro* and *in vivo* experiments.

In our models, cells behave according to a set of rules that remained unchanged during the simulation. However, in reality, the behavior of cells is the result of subcellular signaling in response to external signals. By including the subcellular regulation of cell behavior, the models can be directly related to *in vitro* experiments in which pathway components are upregulated, knocked out, or added ectopically. In the model with tip and stalk cells (chapter 4), cell fate depends on a simplified subcellular pathway but this pathway is not directly linked to cell behavior. Furthermore, in the model with elongated cells (chapter 2) and in the model with pericytes and endothelial cells (chapter 3) none of the cell behavior is connected to subcellular signaling. However, regulation of cell shape in time and space could affect the model outcome, but we did not consider this for cell elongation. In the literature two hypotheses are proposed for the cause of endothelial cell elongation. Several studies proposed that endothelial cells elongate in response to vascular endothelial growth factor (VEGF) [78, 79, 207]. If the VEGF concentration is homogeneous and constant over time, all cells will elongate and this would not affect the model outcome. However, when the VEGF concentration is heterogeneous, or changes over time, the model outcome could be affected. Other studies report that endothelial cells elongated in response to stress in the extracellular matrix (ECM) [208]. A recent computational model of angiogenesis in which the forces cells exert on the ECM induce strain-stiffening supports this hypothesis [126]. Elongation induced by stress in ECM implicates that cells elongate during angiogenesis. Overall, for both hypotheses cell elongation may occur during morphogenesis. Therefore, we should test if elongation during pattern formation affects the formed patterns.

As mentioned above the ECM may affect the shape of cells. Furthermore, the ECM can also affect the distribution of diffusive growth factors and signaling molecules by fixating them. A well-known example of a growth factor that binds to the ECM is VEGF-A [209]. VEGF-A has a heparin binding domain via which it can bind to heparin sulphate proteoglycans, which are part of the ECM [210]. Experiments with embryos that produce VEGF lacking the heparin

binding domain of VEGF showed defects in the developing vasculature [169], indicating that VEGF-ECM binding plays an important role in blood vessel formation. Furthermore, *in vitro*, the binding and unbinding of VEGF to the ECM determines the spatial VEGF pattern [52]. Köhn-Luque and coworkers [29, 52] built a model based on this hypothesis and showed that spatial pattern of VEGF via ECM binding can cause endothelial cells to form networks. In our study of pericyte-endothelial interactions we considered VEGF as one of the possible chemoattractants for endothelial cells, but we did not consider ECM binding. Therefore, a next step in this study would be to consider ECM binding of the chemoattractants. In this way we can further characterize what properties the chemoattractants should have to cause the patterns we observed in the *in vitro* experiments.

When considering mechanical feedback between cells and the ECM and the effect of the ECM on local gradients, we assumed that cells are moving on top of the ECM. In contrast, in 3D cells migrate through the ECM and this requires cells to degrade the ECM. In our study of endothelial tip and stalk cells we validated our 2D modeling results using a 3D sprouting assay. Because of this difference, we could only compare the results at a qualitative level. Furthermore, there were some discrepancies between the model and the experiments, which could be result of this difference. Therefore, to further validate the role of Apelin in tip and stalk cell behavior we should adapt the model presented in chapter 4 to include ECM tunneling and again compare the simulation results with the 3D sprouting assays. Creating a 3D model of angiogenesis with tip and stalk cells is possible, but such a model would be computationally expensive. Because of this, we propose a 2D approach in which cells have to degrade ECM before they can migrate. This approach has been presented previously in a 2D cellular Potts model that studied the role of haptotaxis and haptokinesis [197].

Up to here we discussed the role of the ECM and the regulation of cell behaviors that are included in our models. However, in all the models we omitted proliferation of endothelial cells based on the assumption that cells do not divide in *in vitro* assays. This assumption only holds for *in vitro* vasculogenesis where there is a supply of endothelial cells. In contrast, during *in vivo* sprouting angiogenesis, proliferation is necessary for sprout extension [56]. The cells that proliferate are the stalk cells just behind the tip cells, while the stalk cells farther away from the tip become quiescent cells that do not proliferate [15]. Exactly how this is regulated is not yet clear. Interestingly, both pericytes and Apelin have been implicated to play a role in the regulation of stalk cell proliferation [168]. Pericytes are known to stabilize blood vessels by inhibition proliferation [101]. Apelin, which is secreted in large amounts by tip cells [123, 142, 143], inhibits pericyte recruitment [168]. Thus, close to the sprout tip, there are no pericytes and the stalk cells proliferate. Farther away

from the tip, pericytes are associated to the sprout and proliferation is inhibited. This new hypothesis has been proposed based on experimental data [168], but has not yet been tested mechanistically. Our previous work on both pericytes and tip and stalk cells gives us the ability to test this hypothesis with a computational model.

6.2.2 Validation of angiogenesis models

As discussed in section 1.2.1 several models can explain the formation of vascular network formation. In these models network formation is driven by processes such as: contact-inhibited chemotaxis [28], mechanical interactions between cells and the ECM [21–24, 83, 126], attraction to elongated structures [30, 31], and chemotaxis to ECM bound VEGF [29, 52]. Several of these models can partially reproduce *in vitro* vasculogenesis. The cell-elongation model reproduces the temporal dynamics of pattern coarsening that is observed in vasculogenesis assays with HUVEC on Matrigel [25]. Furthermore, the models based on mechanical interactions between cells and the ECM reproduce the dependence of network formation on the stiffness of the ECM [22, 126]. Finally, in the angiogenesis model that considered VEGF-ECM association, the morphometrics of the networks fitted very well to the metrics of networks of quail embryos [29]. However, this fit only holds for a narrow range of parameters, as was shown by a parameter sensitivity analysis of the model [29]. Altogether, vascular network formation can be reproduced with models based on various hypotheses. Therefore, it remains unclear which hypothesis is true. It is likely that multiple mechanisms can play a role at the same time and that their importance depends on the stage of network development and the environment. For example, mechanical feedback only works when the substrate is sufficient stiff, while the several other mechanisms can produce networks independent of the substrate's mechanical properties.

To determine which model is correct in which specific context of angiogenesis, we focus on the model parameters. A model is only valid when the parameters for which the model fits to experimental data are realistic for that experiment. Using our approach of high-throughput simulations, we can explore the parameters of each of the models and find parameter sets for which a certain model fits experimental data. Note that ideally, this fit not only concerns the final network, but also the network development over time. Then, for each model and parameter set we should determine whether the parameter values are realistic for the experimental data that fits with the model outcome. If a model reproduces experimental patterns with realistic parameters, the modeled mechanism may be the cause of those patterns. In this manner we could link the various proposed mechanisms for angiogenesis to specific experimental setups and use the correct model for further studies related to that experimental setup.

Bibliography

[1]   Folkman, J. and Kalluri, R. Tumor angiogenesis. In: *Cancer Medicine*. Ed. by Kufe, D. W. et al. 6th ed. BC Decker Inc, 2003, 161–194.

[2]   Witmer, A. N. et al. Vascular endothelial growth factors and angiogenesis in eye disease. *Prog. Retin. Eye Res.* 22(1), 2003, 1–29.

[3]   Valastyan, S. and Weinberg, R. A. Tumor metastasis: molecular insights and evolving paradigms. *Cell* 147(2), 2011, 275–292.

[4]   Gupta, G. P. and Massagué, J. Cancer metastasis: building a framework. *Cell* 127(4), 2006, 679–95.

[5]   Jain, R. K. et al. Engineering vascularized tissue. *Nat. Biotechnol.* 23(7), 2005, 821–823.

[6]   Naderi, H. et al. Review paper: critical issues in tissue engineering: biomaterials, cell sources, angiogenesis, and drug delivery systems. *J. Biomater. Appl.* 26(4), 2011, 383–417.

[7]   Novosel, E. C. et al. Vascularization is the key challenge in tissue engineering. *Adv. Drug Deliv. Rev.* 63(4-5), 2011, 300–311.

[8]   Laschke, M. W. and Menger, M. D. Vascularization in tissue engineering: angiogenesis versus inosculation. *Eur. Surg. Res.* 48(2), 2012, 85–92.

[9]   Merks, R. M. H. and Koolwijk, P. Modeling Morphogenesis in silico and in vitro: Towards Quantitative, Predictive, Cell-based Modeling. *Math. Model. Nat. Phenom.* 4(4), 2009, 149–171.

[10] Risau, W. Mechanisms of angiogenesis. *Nature* 386(6626), 1997, 671–674.

[11] Udan, R. S. et al. Understanding vascular development. *Wiley Interdiscip. Rev. Dev. Biol.* 3(2), 2012, 327–346.

[12] De Spiegelaere, W. et al. Intussusceptive angiogenesis: a biologically relevant form of angiogenesis. *J. Vasc. Res.* 49(5), 2012, 390–404.

[13] De Smet, F. et al. Mechanisms of vessel branching: filopodia on endothelial tip cells lead the way. *Arter. Thromb. Vasc. Biol.* 29(5), 2009, 639–649.

[14] Adams, R. H. and Alitalo, K. Molecular regulation of angiogenesis and lymphangiogenesis. *Nat. Rev. Mol. Cell Biol.* 8(6), 2007, 464–478.

[15] Gerhardt, H. et al. VEGF guides angiogenic sprouting utilizing endothelial tip cell filopodia. *J. Cell Biol.* 161(6), 2003, 1163–1177.

[16] Merks, R. M. H. and Glazier, J. A. A cell-centered approach to developmental biology. *Physica A* 352(1), 2005, 113–130.

[17] Jakobsson, L. et al. Endothelial cells dynamically compete for the tip cell position during angiogenic sprouting. *Nat. Cell Biol.* 12(10), 2010, 943–953.

[18] Arima, S. et al. Angiogenic morphogenesis driven by dynamic and heterogeneous collective endothelial cell movement. *Development* 138(21), 2011, 4763–4776.

[19] Gamba, A. et al. Percolation, morphogenesis, and Burgers dynamics in blood vessels formation. *Phys. Rev. Lett.* 90(11), 2003, 118101.

[20] Serini, G. et al. Modeling the early stages of vascular network assembly. *EMBO J.* 22(8), 2003, 1771–1779.

[21]   Manoussaki, D. et al. A mechanical model for the formation of vascular networks in vitro. *Acta Biotheor.* 44(3-4), 1996, 271–282.

[22]   Namy, P. et al. Critical conditions for pattern formation and in vitro tubulogenesis driven by cellular traction fields. *J. Theor. Biol.* 227(1), 2004, 103–120.

[23]   Tranqui, L. and Tracqui, P. Mechanical signalling and angiogenesis. The integration of cell-extracellular matrix couplings. *C. R. Acad. Sci. III, Sci. Vie* 323(1), 2000, 31–47.

[24]   Tracqui, P. et al. Cellular networks morphogenesis induced by mechanically stressed microenvironments. *J. Biol. Phys. Chem.* 5(2-3), 2005, 57.

[25]   Merks, R. M. H. et al. Cell elongation is key to in silico replication of in vitro vasculogenesis and subsequent remodeling. *Dev. Biol.* 289(1), 2006, 44–54.

[26]   Merks, R. M. H. et al. Cell-oriented modeling of in vitro capillary development. In: *Cellular Automata*. Springer, 2004, 425–434.

[27]   Merks, R. M. H. and Glazier, J. A. Dynamic mechanisms of blood vessel growth. *Nonlinearity* 19(1), 2006, C1–C10.

[28]   Merks, R. M. H. et al. Contact-inhibited chemotaxis in de novo and sprouting blood-vessel growth. *PLoS Comput. Biol.* 4(9), 2008, e1000163.

[29]   Köhn-Luque, A. et al. Early embryonic vascular patterning by matrix-mediated paracrine signalling: a mathematical model study. *PLoS ONE* 6(9), 2011, e24175.

[30]   Szabó, A. et al. Network formation of tissue cells via preferential attraction to elongated structures. *Phys. Rev. Lett.* 98(3), 2007, 38102.

[31]   Szabó, A. et al. Multicellular sprouting in vitro. *Biophys. J.* 95(6), 2008, 2702–2710.

[32]   Anderson, A. R. A. and Chaplain, M. A. J. A mathematical model for capillary network formation in the absence of endothelial cell proliferation. *Appl. Math. Lett.* 11(3), 1998, 109–114.

[33]   Bauer, A. L. et al. Topography of extracellular matrix mediates vascular morphogenesis and migration speeds in angiogenesis. *PLoS Comput. Biol.* 5(7), 2009, e1000445.

[34]   Bauer, A. L. et al. A cell-based model exhibiting branching and anastomosis during tumor-induced angiogenesis. *Biophys. J.* 92(9), 2007, 3105–3121.

[35]   Jackson, T. L. and Zheng, X. A Cell-based Model of Endothelial Cell Migration, Proliferation and Maturation During Corneal Angiogenesis. *Bull. Math. Biol.* 72(4), 2010, 830–868.

[36]   Manoussaki, D. A mechanochemical model of angiogenesis and vasculogenesis. *Esaim Math .Model. Numer. Anal.* 37(4), 2003, 581–599.

[37]   Tosin, A. et al. Mechanics and chemotaxis in the morphogenesis of vascular networks. *Bull. Math. Biol.* 68(7), 2006, 1819–1836.

[38]   Szabó, A. and Czirók, A. The Role of Cell-Cell Adhesion in the Formation of Multicellular Sprouts. *Math. Model. Nat. Phenom.* 5(1), 2010, 106–122.

[39]   Boas, S. E. M. and Merks, R. M. H. Synergy of cell-cell repulsion and vacuolation in a computational model of lumen formation. *J. R. Soc. Interface* 11(92), 2014, 20131049.

[40]   Kleinstreuer, N. et al. A Computational Model Predicting Disruption of Blood Vessel Development. *PLoS Comput. Biol.* 9(4), 2013, e1002996.

[41]   Bentley, K. et al. Agent-based simulation of notch-mediated tip cell selection in angiogenic sprout initialisation. *J. Theor. Biol.* 250(1), 2008, 25–36.

[42]   Bentley, K. et al. Tipping the balance: robustness of tip cell selection, migration and fusion in angiogenesis. *PLoS Comput. Biol.* 5(10), 2009, e1000549.

[43]   Liu, G. et al. Module-based multiscale simulation of angiogenesis in skeletal muscle. *Theor. Biol. Med. Model.* 8, 2011, 6.

[44]   Qutub, A. A. and Popel, A. S. Elongation, proliferation & migration differentiate endothelial cell phenotypes and determine capillary sprouting. *BMC Syst. Biol.* 3, 2009, 13.

[45]   Arnaoutova, I. et al. The endothelial cell tube formation assay on basement membrane turns 20: state of the science and the art. *Angiogenesis* 12(3), 2009, 267–274.

[46] Chappell, J. C. et al. How blood vessel networks are made and measured. *Cells Tissues Organs* 195(1-2), 2012, 94–107.

[47] Vernon, R. B. et al. Reorganization of basement membrane matrices by cellular traction promotes the formation of cellular networks in vitro. *Lab. Invest.* 66(5), 1992, 536–547.

[48] Vailhé, B et al. In vitro angiogenesis is modulated by the mechanical properties of fibrin gels and is related to alpha(v)beta3 integrin localization. *Dev. Biol.* 33(10), 1997, 763–773.

[49] Ambrosi, D. et al. Cell directional persistence [corrected] and chemotaxis in vascular morphogenesis. *Bull. Math. Biol.* 66(6), 2004, 1851–1873.

[50] Dejana, E. Endothelial cell-cell junctions: happy together. *Nat. Rev. Mol. Cell Biol.* 5(4), 2004, 261–270.

[51] Wijelath, E. S. et al. Heparin-II domain of fibronectin is a vascular endothelial growth factor-binding domain: enhancement of VEGF biological activity by a singular growth factor/matrix protein synergism. *Circ. Res.* 99(8), 2006, 853–860.

[52] Köhn-Luque, A. et al. Dynamics of VEGF matrix-retention in vascular network patterning. *Phys. Biol.* 10(6), 2013, 66007.

[53] Hillen, F. and Griffioen, A. W. Tumour vascularization: sprouting angiogenesis and beyond. *Cancer Metastasis Rev.* 26(3-4), 2007, 489–502.

[54] Anderson, A. R. A. and Chaplain, M. A. J. Continuous and discrete mathematical models of tumor-induced angiogenesis. *Bull. Math. Biol.* 60(5), 1998, 857–899.

[55] Ausprunk, D. H. and Folkman, J. Migration and proliferation of endothelial cells in pre-formed and newly formed blood vessels during tumor angiogenesis. *Microvasc. Res.* 14(1), 1977, 53–65.

[56] Sholley, M. et al. Mechanisms of neovascularization. Vascular sprouting can occur without proliferation of endothelial cells. *Lab. Invest.* 51(6), 1984, 624–634.

[57] Hellström, M. et al. Dll4 signalling through Notch1 regulataes formation of tip cells during angiogenesis. *Nature* 445(7129), 2007, 776–780.

[58] Suchting, S. et al. The Notch ligand Delta-like 4 negatively regulates endothelial tip cell formation and vessel branching. *Proc. Natl. Acad. Sci. U.S.A.* 104(9), 2007, 3225–3230.

[59] Siekmann, A. F. and Lawson, N. D. Notch signalling limits angiogenic cell behaviour in developing zebrafish arteries. *Nature* 445(7129), 2007, 781–784.

[60] Lobov, I. B. et al. Delta-like ligand 4 (Dll4) is induced by VEGF as a negative regulator of angiogenic sprouting. *Proc. Natl. Acad. Sci. U.S.A.* 104(9), 2007, 3219–3224.

[61] Ridgway, J. et al. Inhibition of Dll4 signalling inhibits tumour growth by deregulating angiogenesis. *Nature* 444(7122), 2006, 1083–1087.

[62] Patel, N. S. et al. Up-regulation of delta-like 4 ligand in human tumor vasculature and the role of basal expression in endothelial cell function. *Cancer Res.* 65(19), 2005, 8690–8697.

[63] Hainaud, P. et al. The role of the vascular endothelial growth factor-Delta-like 4 ligand /Notch4-ephrin B2 cascade in tumor vessel remodeling and endothelial cell functions. *Cancer Res.* 66(17), 2006, 8501–8510.

[64] Fisher, A. B. et al. Endothelial cellular response to altered shear stress. *Am. J. Physiol. Lung Cell Mol. Physiol.* 281(3), 2001, L529–L533.

[65] McDougall, S. R. et al. Mathematical modelling of dynamic adaptive tumour-induced angiogenesis: clinical implications and therapeutic targeting strategies. *J. Theor. Biol.* 241(3), 2006, 564–589.

[66] Qutub, A. A. et al. Multiscale Models of Angiogenesis. *IEEE Eng. Med. Biol. Mag.* 28(2), 2009, 14–31.

[67] Qutub, A. A. et al. "Integration of angiogenesis modules at multiple scales: from molecular to tissue." In: *Pac. Symp. Biocomput.* 2009, 316–327.

[68] Shirinifard, A. et al. 3D multi-cell simulation of tumor growth and angiogenesis. *PLoS ONE* 4(10), 2009, e7190.

[69]   Fruttiger, M. Development of the mouse retinal vasculature: angiogenesis versus vasculogenesis. *Invest. Ophthalmol. Vis. Sci.* 43(2), 2002, 522–527.

[70]   Enge, M. et al. Endothelium-specific platelet-derived growth factor-B ablation mimics diabetic retinopathy. *EMBO J.* 21(16), 2002, 4307–4316.

[71]   Morikawa, S. et al. Abnormalities in pericytes on blood vessels and endothelial sprouts in tumors. *Am. J. Pathol.* 160(3), 2002, 985–1000.

[72]   Elsdale, T. R. Parallel orientation of fibroblasts in vitro. *Exp. Cell Res.* 51(2-3), 1968, 439–50.

[73]   Pietak, A. and Waldman, S. D. Seeing tissue as a 'phase of matter': exploring statistical mechanics for the cell. *Phys. Biol.* 5(1), 2008, 016007.

[74]   Szabó, A. et al. Collective cell motion in endothelial monolayers. *Phys. Biol.* 7(4), 2010, 46007.

[75]   Elsdale, T. R. Fibroblast cultures and dermatoglyphics: the topology of two planar patterns. *Dev. Genes Evol.* 180(2), 1976, 121–147.

[76]   Angelini, T. E. and Hannezo, E. Glass-like dynamics of collective cell migration. *Proc. Natl. Acad. Sci. U.S.A.* 108(12), 2011, 4714–4719.

[77]   Garrahan, J. P. Dynamic heterogeneity comes to life. *Proc. Natl. Acad. Sci. U.S.A.* 108(12), 2011, 4701–4702.

[78]   Cao, Y. et al. Vascular endothelial growth factor C induces angiogenesis in vivo. *Proc. Natl. Acad. Sci. U.S.A.* 95(24), 1998, 14389–14394.

[79]   Drake, C. J. et al. VEGF regulates cell behavior during vasculogenesis. *Dev. Biol.* 224(2), 2000, 178–188.

[80]   Parsa, H et al. Uncovering the behaviors of individual cells within a multicellular microvascular community. *Proc. Natl. Acad. Sci. U.S.A.* 108(12), 2011, 5133–5138.

[81]   Scianna, M. et al. A multiscale hybrid approach for vasculogenesis and related potential blocking therapies. *Prog. Biophys. Mol. Biol.* 106(2), 2011, 450–462.

[82]   Manoussaki, D. Modeling and simulation of the formation of vascular networks. *ESAIM Proc.* 12, 2002, 108–114.

[83]   Murray, J. D. On the mechanochemical theory of biological pattern formation with application to vasculogenesis. *C. R. Biol.* 326(2), 2003, 239–252.

[84]   Graner, F. and Glazier, J. A. Simulation of biological cell sorting using a two-dimensional extended Potts model. *Phys. Rev. Lett.* 69(13), 1992, 2013–2016.

[85]   Glazier, J. A. and Graner, F. Simulation of the differential adhesion driven rearrangement of biological cells. *Phys. Rev. E* 47(3), 1993, 2128–2154.

[86]   Glazier, J. A. et al. Coordinated action of N-CAM, N-cadherin, EphA4, and ephrinB2 translates genetic prepatterns into structure during somitogenesis in chick. *Curr. Top. Dev. Biol.* 81, 2008, 205–247.

[87]   Hester, S. D. et al. A Multi-cell, Multi-scale Model of Vertebrate Segmentation and Somite Formation. *PLoS Comput. Biol.* 7(10), 2011, e1002155.

[88]   Zajac, M et al. Model of convergent extension in animal morphogenesis. *Phys. Rev. Lett.* 85(9), 2000, 2022–2025.

[89]   Käfer, J. et al. Cell adhesion and cortex contractility determine cell patterning in the Drosophila retina. *Proc. Natl. Acad. Sci. U.S.A.* 104(47), 2007, 18549–18554.

[90]   Savill, N. J. and Hogeweg, P. Modelling morphogenesis: from single cells to crawling slugs. *J. Theor. Biol.* 184(3), 1996, 229–235.

[91]   De Gennes, P. G. and Prost, J. *The physics of liquid crystals*. 2nd editio. Oxford University Press, 1993.

[92]   Foffi, G et al. Arrested phase separation in a short-ranged attractive colloidal system: A numerical study. *J. Chem. Phys.* 122(22), 2005, 224903.

[93]   Solomon, M. J. and Spicer, P. T. Microstructural regimes of colloidal rod suspensions, gels, and glasses. *Soft Matter* 6(7), 2010, 1391–1400.

[94] Bernal, J. D. and Fankuchen, I. X-ray and crystallographic studies of plant virus preparations. *J. Gen. Physiol.* 25(1), 1941, 111–146.

[95] Bruggen, M. P. B. van and Lekkerkerker, H. N. W. Metastability and Multistability: Gelation and Liquid Crystal Formation in Suspensions of Colloidal Rods. *Langmuir* 18(19), 2002, 7141–7145.

[96] Wilkins, G. M. H. et al. Colloidal system to explore structural and dynamical transitions in rod networks, gels, and glasses. *Langmuir* 25(16), 2009, 8951–8959.

[97] Gaengel, K. et al. Endothelial-mural cell signaling in vascular development and angiogenesis. *Arter. Thromb. Vasc. Biol.* 29(5), 2009, 630–638.

[98] Armulik, A. et al. Pericytes: developmental, physiological, and pathological perspectives, problems, and promises. *Dev. Cell* 21(2), 2011, 193–215.

[99] Benjamin, L. E. et al. A plasticity window for blood vessel remodelling is defined by pericyte coverage of the preformed endothelial network and is regulated by PDGF-B and VEGF. *Development* 125(9), 1998, 1591–1598.

[100] Stratman, A. N. et al. Pericyte recruitment during vasculogenic tube assembly stimulates endothelial basement membrane matrix formation. *Blood* 114(24), 2009, 5091–5101.

[101] Hellström, M. et al. Lack of pericytes leads to endothelial hyperplasia and abnormal vascular morphogenesis. *J. Cell Biol.* 153(3), 2001, 543–553.

[102] Ribatti, D. et al. The role of pericytes in angiogenesis. *Dev. Biol.* 55(3), 2011, 261–268.

[103] Antonelli-Orlidge, A. et al. An activated form of transforming growth factor beta is produced by cocultures of endothelial cells and pericytes. *Proc. Natl. Acad. Sci. U.S.A.* 86(12), 1989, 4544–4548.

[104] Sato, Y. and Rifkin, D. B. Inhibition of endothelial cell movement by pericytes and smooth muscle cells: activation of a latent transforming growth factor-beta 1-like molecule by plasmin during. *J. Cell Biol.* 109(1), 1989, 309–315.

[105] Sato, Y et al. Characterization of the activation of latent TGF-beta by co-cultures of endothelial cells and pericytes or smooth muscle cells: a self-regulating system. *J. Cell Biol.* 111(2), 1990, 757–763.

[106] Horiguchi, M. et al. Matrix control of transforming growth factor-β function. *J. Biochem.* 152(4), 2012, 321–329.

[107] Oh, S. P. et al. Activin receptor-like kinase 1 modulates transforming growth factor-beta 1 signaling in the regulation of angiogenesis. *Proc. Natl. Acad. Sci. U.S.A.* 97(6), 2000, 2626–2631.

[108] Goumans, M. J. et al. Balancing the activation state of the endothelium via two distinct TGF-beta type I receptors. *EMBO J.* 21(7), 2002, 1743–1753.

[109] Goumans, M. J. et al. Activin receptor-like kinase (ALK)1 is an antagonistic mediator of lateral TGFbeta/ALK5 signaling. *Mol. Cell* 12(4), 2003, 817–828.

[110] Hirschi, K. K. et al. PDGF, TGF-β, and heterotypic cell-cell interactions mediate endothelial cell-induced recruitment of 10T1/2 cells and their differentiation to a smooth muscle fate. *J. Cell Biol.* 141(3), 1998, 805–814.

[111] Lindahl, P. et al. Pericyte Loss and Microaneurysm Formation in PDGF-B-Deficient Mice. *Science* 277(5323), 1997, 242–245.

[112] Hellström, M. et al. Role of PDGF-B and PDGFR-beta in recruitment of vascular smooth muscle cells and pericytes during embryonic blood vessel formation in the mouse. *Development* 126(14), 1999, 3047–3055.

[113] Stratman, A. N. et al. Endothelial-derived PDGF-BB and HB-EGF coordinately regulate pericyte recruitment during vasculogenic tube assembly and stabilization. *Blood* 116(22), 2010, 4720–4730.

[114] Witzenbichler, B. et al. Chemotactic Properties of Angiopoietin-1 and -2, Ligands for the Endothelial-specific Receptor Tyrosine Kinase Tie2. *J. Biol. Chem.* 273(29), 1998, 18514–18521.

[115] Holmes, K. et al. Vascular endothelial growth factor receptor-2: structure, function, intracellular signalling and therapeutic inhibition. *Cell. Signal.* 19(10), 2007, 2003–2012.

[116] Ferrara, N. Vascular endothelial growth factor: basic science and clinical progress. *Endocr. Rev.* 25(4), 2004, 581–611.

[117] Darland, D. C. et al. Pericyte production of cell-associated VEGF is differentiation-dependent and is associated with endothelial survival. *Dev. Biol.* 264(1), 2003, 275–288.

[118] Reinmuth, N. et al. Induction of VEGF in perivascular cells defines a potential paracrine mechanism for endothelial cell survival. *FASEB J* 15(7), 2001, 1239–1241.

[119] Franco, M. et al. Pericytes promote endothelial cell survival through induction of autocrine VEGF-A signaling and Bcl-w expression. *Cell* 118(10), 2011, 2906–2917.

[120] Byrne, A. M. et al. Angiogenic and cell survival functions of vascular endothelial growth factor (VEGF). *J. Cell. Mol. Med.* 9(4), 2005, 777–794.

[121] Zajac, M. et al. Simulating convergent extension by way of anisotropic differential adhesion. *J. Theor. Biol.* 222(2), 2003, 247–259.

[122] Claxton, S. and Fruttiger, M. Periodic Delta-like 4 expression in developing retinal arteries. *Gene Expr. Patterns* 5(1), 2004, 123–127.

[123] Siemerink, M. J. et al. CD34 marks angiogenic tip cells in human vascular endothelial cell cultures. *Angiogenesis* 15(1), 2012, 151–163.

[124] Folkman, J and Hauenschild, C. Angiogenesis in vitro. English. *Nature* 288(5791), 1980, 551–556.

[125] Califano, J. and Reinhart-King, C. A. A balance of substrate mechanics and matrix chemistry regulates endothelial cell network assembly. English. *Cell Mol. Bioeng.* 1(2), 2008, 122–132.

[126] Oers, R. F. M. van et al. Mechanical cell-matrix feedback explains pairwise and collective endothelial cell behavior in vitro. *PLoS Comput. Biol.* 2014. arXiv:1308.3721, In press.

[127] Sainson, R. C. A. et al. Cell-autonomous notch signaling regulates endothelial cell branching and proliferation during vascular tubulogenesis. *FASEB J* 19(8), 2005, 1027–1029.

[128] Williams, C. K. et al. Up-regulation of the Notch ligand Delta-like 4 inhibits VEGF-induced endothelial cell function. *Blood* 107(3), 2006, 931–939.

[129] Scehnet, J. S. et al. Inhibition of Dll4-mediated signaling induces proliferation of immature vessels and results in poor tissue perfusion. *Blood* 109(11), 2007, 4753–4760.

[130] Jakobsson, L. et al. VEGFRs and Notch: a dynamic collaboration in vascular patterning. *Biochem. Soc. Trans.* 37(Pt 6), 2009, 1233–1236.

[131] Hiratsuka, S et al. Flt-1 lacking the tyrosine kinase domain is sufficient for normal development and angiogenesis in mice. *Proc. Natl. Acad. Sci. U.S.A.* 95(16), 1998, 9349–9354.

[132] Rahimi, N. et al. Receptor chimeras indicate that the vascular endothelial growth factor receptor-1 (VEGFR-1) modulates mitogenic activity of VEGFR-2 in endothelial cells. *J. Biol. Chem.* 275(22), 2000, 16986–16992.

[133] Long, B. L. et al. Cells as state machines: Cell behavior patterns arise during capillary formation as a function of BDNF and VEGF. *J. Theor. Biol.* 326, 2012, 43–57.

[134] Palm, M. M. and Merks, R. M. H. Vascular networks due to dynamically arrested crystalline ordering of elongated cells. *Phys. Rev. E* 87(1), 2013, 12725.

[135] Gory-Fauré, S. et al. Role of vascular endothelial-cadherin in vascular morphogenesis. *Development* 126(10), 1999, 2093–2102.

[136] Shirinifard, A. et al. Adhesion Failures Determine the Pattern of Choroidal Neovascularization in the Eye: A Computer Simulation Study. *PLoS Comput. Biol.* 8(5), 2012, e1002440.

[137] Donà, E. et al. Directional tissue migration through a self-generated chemokine gradient. *Nature* 503(7475), 2013, 285–289.

[138] Benedito, R. et al. Notch-dependent VEGFR3 upregulation allows angiogenesis without VEGF-VEGFR2 signalling. *Nature* 484(7392), 2012, 110–114.

[139] Benedito, R. et al. The notch ligands Dll4 and Jagged1 have opposing effects on angiogenesis. *Cell* 137(6), 2009, 1124–1135.

[140] Bentley, K. et al. The role of differential VE-cadherin dynamics in cell rearrangement during angiogenesis. *Nat. Cell Biol.* 16(4), 2014, 309–321.

[141] Harrington, L. S. et al. Regulation of multiple angiogenic pathways by Dll4 and Notch in human umbilical vein endothelial cells. *Microvasc. Res.* 75(2), 2008, 144–154.

[142] Toro, R. del et al. Identification and functional analysis of endothelial tip cell-enriched genes. *Blood* 116(19), 2010, 4025–4033.

[143] Strasser, G. A. et al. Microarray analysis of retinal endothelial tip cells identifies CXCR4 as a mediator of tip cell morphology and branching. *Blood* 115(24), 2010, 5102–5110.

[144] Seghezzi, G et al. Fibroblast growth factor-2 (FGF-2) induces vascular endothelial growth factor (VEGF) expression in the endothelial cells of forming capillaries: an autocrine mechanism contributing to angiogenesis. *J. Cell Biol.* 141(7), 1998, 1659–1673.

[145] Geudens, I. and Gerhardt, H. Coordinating cell behaviour during blood vessel formation. *Development* 138(21), 2011, 4569–4583.

[146] Gupta, S. K. et al. Chemokine Receptors in Human Endothelial Cells. *J. Biol. Chem.* 273(7), 1998, 4282–4287.

[147] Salcedo, R. and Oppenheim, J. J. Role of chemokines in angiogenesis: CXCL12/ SDF-1 and CXCR4 interaction, a key regulator of endothelial cell responses. *Microcirculation* 10(3-4), 2003, 359–370.

[148] Tatemoto, K et al. Isolation and characterization of a novel endogenous peptide ligand for the human APJ receptor. *Biochem. Biophys. Res. Commun.* 251(2), 1998, 471–476.

[149] Kasai, A. et al. Apelin is a novel angiogenic factor in retinal endothelial cells. *Biochem. Biophys. Res. Commun.* 325(2), 2004, 395–400.

[150] Kälin, R. E. et al. Paracrine and autocrine mechanisms of apelin signaling govern embryonic and tumor angiogenesis. *Dev. Biol.* 305(2), 2007, 599–614.

[151] Salvucci, O et al. Regulation of endothelial cell branching morphogenesis by endogenous chemokine stromal-derived factor-1. *Cell* 99(8), 2002, 2703–2711.

[152] Reinhart-King, C. A. et al. Cell-cell mechanical communication through compliant substrates. *Biophys. J.* 95(12), 2008, 6044–6051.

[153] Cox, C. M. et al. Apelin, the ligand for the endothelial G-protein-coupled receptor, APJ, is a potent angiogenic factor required for normal vascular development of the frog embryo. *Dev. Biol.* 296(1), 2006, 177–189.

[154] Eyries, M. et al. Hypoxia-induced apelin expression regulates endothelial cell proliferation and regenerative angiogenesis. *Circ. Res.* 103(4), 2008, 432–440.

[155] Kasai, A. et al. Retardation of retinal vascular development in apelin-deficient mice. *Arter. Thromb. Vasc. Biol.* 28(10), 2008, 1717–1722.

[156] Milde, F. et al. A hybrid model for three-dimensional simulations of sprouting angiogenesis. *Biophys. J.* 95(7), 2008, 3146–3160.

[157] Artel, A. et al. An Agent-Based Model for the Investigation of Neovascularization Within Porous Scaffolds. *Tissue Eng. Part A* 17(17-18), 2011, 2133–2141.

[158] Mehdizadeh, H. et al. Three-dimensional modeling of angiogenesis in porous biomaterial scaffolds. *Biomaterials* 34(12), 2013, 2875–2887.

[159] Travasso, R. D. M. et al. Tumor angiogenesis and vascular patterning: a mathematical model. *PLoS ONE* 6(5), 2011, e19989.

[160] Bautch, V. L. VEGF-Directed Blood Vessel Patterning: From Cells to Organism. *Cold Spring Harb. Perspect. Med.* 2(9), 2012.

[161] Caolo, V. et al. Feed-forward signaling by membrane-bound ligand receptor circuit: the case of notch delta-like 4 ligand in endothelial cells. *J. Biol. Chem.* 285(52), 2010, 40681–40689.

[162] Kidoya, H. et al. Spatial and temporal role of the apelin/APJ system in the caliber size regulation of blood vessels during angiogenesis. *EMBO J.* 27(3), 2008, 522–534.

[163] Hara, C. et al. Laser-Induced Choroidal Neovascularization in Mice Attenuated by Deficiency in the Apelin-APJ System. *Invest. Ophthalmol. Vis. Sci.* 54(6), 2013, 4321–5329.

[164] Taylor, K. L. et al. Notch Activation during Endothelial Cell Network Formation in Vitro Targets the Basic HLH Transcription Factor HESR-1 and Downregulates VEGFR-2/KDR Expression. *Microvasc. Res.* 64(3), 2002, 372–383.

[165] Funahashi, Y. et al. Notch regulates the angiogenic response via induction of VEGFR-1. *J. Angiogenes Res.* 2(1), 2010, 3.

[166] Park, J. E. et al. Placenta growth factor. Potentiation of vascular endothelial growth factor bioactivity, in vitro and in vivo, and high affinity binding to Flt-1 but not to Flk-1/KDR. *J. Biol. Chem.* 269(41), 1994, 25646–25654.

[167] Gavard, J and Gutkind, J. S. VEGF controls endothelial-cell permeability by promoting the β-arrestin-dependent endocytosis of VE-cadherin. *Nat. Cell Biol.* 8(11), 2006, 1223–1234.

[168] Kasai, A. et al. Inhibition of apelin expression switches endothelial cells from proliferative to mature state in pathological retinal angiogenesis. *Angiogenesis* 16(3), 2013, 723–734.

[169] Ruhrberg, C. et al. Spatially restricted patterning cues provided by heparin-binding VEGF-A control blood vessel branching morphogenesis. *Genes Dev.* 16(20), 2002, 2684–2698.

[170] Bray, S. J. Notch signalling: a simple pathway becomes complex. *Nat. Rev. Mol. Cell Biol.* 7(9), 2006, 678–689.

[171] Galler, B. A. and Fisher, M. J. An improved equivalence algorithm. *Commun. ACM* 7(5), 1964, 301–303.

[172] Graham, R. L. An efficient algorith for determining the convex hull of a finite planar set. *Inf. Process. Lett.* 72(1), 1972, 132–133.

[173] Guidolin, D. et al. A new image analysis method based on topological and fractal parameters to evaluate the angiostatic activity of docetaxel by using the Matrigel assay in vitro. *Microvasc. Res.* 67(2), 2004, 117–124.

[174] Dougherty, E. R. and Lotufo, R. A. *Hands-on morphological image processing*. SPIE PRESS, 2003.

[175] Coelho, L. Mahotas: Open source software for scriptable computer vision. *J. Open Res. Softw.* 1(1), 2013, e3.

[176] *Pymorph.* http://luispedro.org/software/pymorph.

[177] Dijkstra, E. W. A note on two problems in connexion with graphs. *Numer. Math.* 1(1), 1959, 269–271.

[178] Swat, M. H. et al. Multi-Scale Modeling of Tissues Using CompuCell3D. In: *Comput. Methods Cell Biol.* Ed. by Asthagiri, A. R. and Arkin, A. P. Academic Press, 2012, 325–366.

[179] Palm, M. M. and Merks, R. M. H. Large-scale parameter studies of cell-based models of tissue morphogenesis using CompuCell3D or VirtualLeaf. In: *Tissue Morphogenesis: Methods and Protocols*. Ed. by Nelson, C. M. Vol. 1189, Methods in Molecular Biology. New York: Springer, 2014, In press.

[180] Korff, T and Augustin, H. Integration of endothelial cells in multicellular spheroids prevents apoptosis and induces differentiation. *J. Cell Biol.* 143(5), 1998, 1341–1352.

[181] Schneider, C. A. et al. NIH Image to ImageJ: 25 years of image analysis. *Nat. Methods* 9(7), 2012, 671–675.

[182] Meijering, E et al. Design and validation of a tool for neurite tracing and analysis in fluorescence microscopy images. *Cytometry A* 58A(2), 2004, 167–176.

[183] *Reverse Transfection of siRNA.* http://www.thermoscientificbio.com/uploadedfiles/resources/reverse-transfection-of-sirna-protocol.pdf.

[184] Tukey, J. Comparing individual means in the analysis of variance. *Biometrics* 5(2), 1949, 99–114.

[185] Abdi, H. and Williams, L. Newman-Keuls Test and Tukey Test. In: *Encyclopedia of Research Design.* Ed. by Salkind, N. Thousand Oaks: Sage, 2010, 897–904.

[186] Anderson, A. R. A. et al., eds. *Single-cell-based models in biology and medicine*. Basel: Birkhäuser Verlag, 2007.

[187] Drasdo, D and Höhme, S. Individual-based approaches to birth and death in avascular tumors. *Math. Comput. Model.* 37(11), 2003, 1163–1175.

[188] Alarcón, T. et al. A Multiple Scale Model for Tumor Growth. *Multiscale Model. Simul.* 3(2), 2005, 440–475.

[189] Kim, Y. et al. A hybrid model for tumor spheroid growth in vitro I: theoretical development and early results. *Math. Models Methods Appl. Sci.* 17(supp01), 2007, 1773–1798.

[190] Macklin, P. et al. Patient-calibrated agent-based modelling of ductal carcinoma in situ (DCIS): from microscopic measurements to macroscopic predictions of clinical progression. *J. Theor. Biol.* 301, 2012, 122–140.

[191] Hoehme, S. et al. Prediction and validation of cell alignment along microvessels as order principle to restore tissue architecture in liver regeneration. *Proc. Natl. Acad. Sci. U.S.A.* 107(23), 2010, 10371–10376.

[192] Merks, R. M. H. et al. VirtualLeaf: an open-source framework for cell-based modeling of plant tissue growth and development. *Plant Physiol.* 155(2), 2011, 656–666.

[193] Hamant, O. et al. Developmental patterning by mechanical signals in Arabidopsis. *Science* 322(5908), 2008, 1650–1655.

[194] Hirashima, T. et al. Dynamic modeling of branching morphogenesis of ureteric bud in early kidney development. *J. Theor. Biol.* 259(1), 2009, 58–66.

[195] Engelberg, J. A. et al. MDCK cystogenesis driven by cell stabilization within computational analogues. *PLoS Comput. Biol.* 7(4), 2011, e1002030.

[196] Andasari, V. et al. Integrating intracellular dynamics using CompuCell3D and Bionetsolver: applications to multiscale modelling of cancer cell growth and invasion. *PLoS ONE* 7(3), 2012, e33726.

[197] Daub, J. T. and Merks, R. M. H. A Cell-Based Model of Extracellular-Matrix-Guided Endothelial Cell Migration During Angiogenesis. *Bull. Math. Biol.* 75(8), 2013, 1377–1399.

[198] Swat, M. H. et al. *CompuCell3D Reference Manual*. 2012.

[199] Noble, W. S. A quick guide to organizing computational biology projects. *PLoS Comput. Biol.* 5(7), 2009, e1000424.

[200] Henderson, R. L. Job scheduling under the portable batch system. In: *Job scheduling strategies for parallel processing*. Springer, 1995, 279–294.

[201] Merks, R. M. H. and Guravage, M. A. Building simulation models of developing plant organs using VirtualLeaf. In: *Plant Organogenesis*. Ed. by De Smet, I. Springer, 2013, 333–352.

[202] Debnath, J. et al. The Role of Apoptosis in Creating and Maintaining Luminal Space within Normal and Oncogene-Expressing Mammary Acini. *Cell* 111(5), 2002, 29–40.

[203] Debnath, J. et al. Morphogenesis and oncogenesis of MCF-10A mammary epithelial acini grown in three-dimensional basement membrane cultures. *Methods* 30(3), 2003, 256–268.

[204] Muthuswamy, S. K. et al. ErbB2, but not ErbB1, reinitiates proliferation and induces luminal repopulation in epithelial acini. *Nat. Cell Biol.* 3(9), 2001, 785–792.

[205] Saltelli, A. and Chan, K. and Scott, E. *Sensitivity analysis*. Wiley, 2008.

[206] Swat, M. et al. *Developers´ Documentation for CompuCell3D*. 2009.

[207] Helmlinger, G. et al. Growth factors: Formation of endothelial cell networks. *Nature* 405(6783), 2000, 139–141.

[208] Winer, J. P. et al. Non-linear elasticity of extracellular matrices enables contractile cells to communicate local position and orientation. *PLoS ONE* 4(7), 2009, e6382.

[209] Houck, K. A. et al. Dual regulation of vascular endothelial growth factor bioavailability by genetic and proteolytic mechanisms. *J. Biol. Chem.* 267(36), 1992, 26031–26037.

[210] Stringer, S. E. The role of heparan sulphate proteoglycans in angiogenesis. *Biochem. Soc. Trans.* 34(Pt 3), 2006, 451–453.

Summary

Angiogenesis is the process by which new blood vessels develop by splitting of or by sprouting from existing vessels. The sprouts formed in the latter mechanism, known as sprouting angiogenesis, branch out and connect with other sprouts to form a new network of blood vessels. This process involves both the endothelial cells, which make up the inner lining of a vessel, and the perivascular cells, which surround the vessel. The collective behavior of these cells results in the formation of sprouts and eventually vascular networks. The cells involved in angiogenesis differ in shape and behavior, which affects their collective behavior. Furthermore, the cells also affect one another via diffusive and membrane bound signaling molecules. In this thesis we aim to understand how the interaction between multiple cell-types exhibiting subtle differences in behavior change the resulting collective angiogenic sprouting.

To this end, we developed cell-based, computational models of angiogenesis, based on the cellular Potts model. The inputs of these models are the observed or hypothesized behavior of individual cells and the output is the resulting collective cell behavior: e.g., the formation of angiogenic sprouts or vascular networks. By assigning different behavior to a subset of the cells, these models can be used to study the interplay between cell types exhibiting different behavior. Because the exact parameter values are not always known, we need to perform simulations for a wide range of parameter values. For this, we developed a high-throughput simulation pipeline, which is presented in chapter 5, that automates setting up the simulation scripts, running the simulations on a computer cluster and analyzing the results. This pipeline allowed us to screen a wide range of new hypotheses concerning the differences between cell types, and thereby enabled us to develop new hypotheses that could be tested in the wet-lab.

In chapter 2, we studied the role of cell elongation in angiogenesis. Based on *in vitro* observations, previous simulation studies have proposed that cells form vascular networks because they are attracted to one another via an autocrine chemoattractant. With such a mechanism cells form aggregates, unless additional mechanisms make the cells organize into sprouts. One of these additional mechanisms is cell elongation. To understand how the elon-

gated cell shape contributes to the formation of network-like structures, we studied the aggregation of elongated cells in absence of the chemoattractant. We found that also without chemotaxis cells organize into networks, provided that the cells slightly adhere to one another. The elongated cells align side-to-side and thereby formed cell clusters. Individual, elongated cells rotate easily, but rotation becomes increasingly difficult as the cluster size increases. As the clusters grow in size, due to cell-cell adhesion, the dynamics slows down, until it essentially stalls. Even though the configuration still slowly evolves towards the equilibrium, consisting of a single cluster with groups of aligned cells, this equilibrium is not reached in practice; this phenomenon is known as "arrested dynamics". In the model with chemoattraction between the cells, the pattern continues to evolve, which suggest that in that model the network represents a true equilibrium.

With the insights into the role of cell elongation obtained in this way, in chapter 3 we studied the role of pericytes in angiogenesis. Pericytes are a type of perivascular cells that are observed in growing sprouts during ocular and tumor angiogenesis. To better understand how pericytes are involved in angiogenesis we attempted to reproduce *in vitro* observations of co-cultures of endothelial cells and pericytes with computational modeling. *In vitro*, endothelial cells and pericytes rapidly form networks. Unlike the stable networks formed in endothelial monocultures, the networks formed in the mixed cultures collapse into a cluster. Interestingly, new sprouts extend from these clusters after a couple of days. To test if and how reported chemotactic interactions between endothelial cells and pericytes could cause the *in vitro* patterns we simulated several model variants that differ in which cells secrete which chemoattractants. For this, we built a model with elongated endothelial cells and round pericytes that are each attracted to their own autocrine chemoattractant. Then, we generated model variants by adding additional chemoattractants for endothelial cells and varying which cell types secrete which chemoattractant. We found that networks develop in simulations where pericytes secrete a chemoattractant for endothelial cells and vice versa. Similar to the *in vitro* experiments, these network are unstable and quickly collapse into a cluster. To also reproduce sprouting, one model adjustment was needed: Not pericytes secrete a chemoattractant for endothelial cells, but endothelial cells that are in direct contact with pericytes secrete that chemoattractant. Together, the results presented in chapter 3 hypothesize crosstalk between endothelial cells and pericytes via chemoattractants. Whether these interactions indeed play a role in the collective behavior of endothelial cells and pericytes during angiogenesis is the topic of ongoing investigations.

The study presented in chapter 4 concerns differences between two subtypes of endothelial cells: the tip cells that lead the sprouts, and the stalk

cells that follow the tip cells and proliferate to facilitate sprout extension. Whereas tip and stalk cell differentiation is necessary for *in vivo* angiogenesis, computational models and cell culture models can recapitulate aspects of blood vessel formation in monocultures, without tip and stalk cell differentiation. To develop new ideas on the mechanisms by which tip cells could contribute to blood vessel formation we extended an existing computational model with tip and stalk cell differentiation, avoiding any a priori assumptions about the differences between tip and stalk cells. We then systematically changed the behavior of the tip cells, to identify model variants in which the computational tip cells' behavior matched that of real tip cells: They lead sprouts and impact the resulting blood vessel networks. Our model predicted that tip cells may be less attracted to the chemoattractant. Interestingly, this prediction matched the expression pattern of a known molecular signal, called Apelin. We tested our computational predictions in an actual cell culture model of angiogenic sprouting, which indeed turned out to be sensitive to interference with Apelin signaling.

In this thesis we aimed to understand how the interactions between cell-types exhibiting different behaviors affect angiogenic sprouting. In high-throughput simulation experiments we varied the chemotactic interacts between endothelial cells and pericytes and found that such interactions could reproduce the patterns these cells formed in *in vitro* cocultures. With a similar approach we searched for cell behavior for which computational tip cells resemble real tip cells. In this manner we found that the reduced sensitivity of the tip cells to Apelin may cause them to lead sprouts and affect the morphology of vascular networks. Altogether, in this thesis we reverse engineered possible roles for pericytes and tip cells in angiogenesis by performing high-throughput simulation experiments.

Samenvatting

Angiogenese is het proces waarbij nieuwe bloedvaten ontstaan uit bestaande bloedvaten doordat een bloedvat in tweeën splitst of doordat er nieuwe zijtakken, zogenaamde *spruiten*, ontstaan. De spruiten die ontstaan in het laatste geval, genaamd spruitvormende angiogenese, vertakken en vormen verbindingen met andere spruiten en zo ontstaat een netwerk van bloedvaten. Bij dit proces zijn zowel de endotheelcellen uit de binnenste laag van het bloedvat als de daarom heen liggende perivasculaire cellen betrokken. Het collectieve gedrag van deze cellen leidt tot de vorming van spruiten en de daaropvolgende ontwikkeling van netwerken. De cellen betrokken bij angiogenese verschillen in gedrag en vorm en dit heeft invloed op het collectieve gedrag. Daarnaast kunnen de cellen elkaars gedrag beïnvloeden via diffunderende en membraangebonden signaalmoleculen. Dit proefschrift analyseert het samenspel tussen cellen van verschillende types, die verschillen in gedrag en vorm, tijdens angiogenese.

Om het samenspel tussen cellen tijdens angiogenese te onderzoeken maken we gebruik van cel-gebaseerde computermodellen die gebaseerd zijn op het *cellular Potts* model. In deze modellen wordt het gedrag en de vorm van de cellen voorgeschreven en simulaties laten zien hoe de cellen zich organiseren tot een weefsel, zoals spruiten of netwerken van bloedvaten. Door verschillend gedrag voor te schrijven voor een subset van de cellen kunnen deze modellen gebruikt worden om het samenspel tussen verschillende celtypes te bestuderen. Omdat de correcte parameterwaardes niet altijd bekend zijn is het noodzakelijk om simulaties uit te voeren met uiteenlopende parameterwaardes. Hiervoor hebben we een *high-throughput* simulatie protocol opgesteld, beschreven in hoofdstuk 5, dat het opzetten van simulatiescripts, het uitvoeren van de simulaties op een computercluster, en het analyseren van de resultaten automatiseerd. Gebruikmakende van dit protocol kunnen we uiteenlopende hypotheses met betrekking tot de rol van verschillen in celgedrag in angiogenese testen en zo nieuwe hypotheses ontwikkelen die daarna in het laboratorium getest kunnen worden.

In hoofdstuk 2 hebben we de rol van langwerpige cellen in angiogenese onderzocht. In eerdere simulatiestudies werd, naar aanleiding van *in vitro* observaties, aangenomen dat cellen netwerken vormen omdat ze elkaar aantrek-

ken via een autocriene chemoattractant. Dit mechanisme resulteert echter in de vorming van celclusters, tenzij er een extra mechanisme is dat ervoor zorgt dat de cellen zich organiseren in spruiten. Één van deze mechanismes is het langwerpig worden van de cellen. Om te begrijpen waarom juist langwerpige cellen netwerken vormen hebben we het collectieve gedrag van de langwerpige cellen onderzocht in afwezigheid van een chemoattractant. Uit onze simulaties bleek dat langwerpige cellen een netwerk vormen, mits deze cellen enigszins aan elkaar plakken. Tijdens dit proces lijnen de cellen uit langs hun lange cellen en vormen celclusters. Terwijl een losse cel gemakkelijk kan roteren, is de rotatie van cellen in een groot cluster beperkt. Doordat de clusters blijven groeien neemt de dynamiek van de patroonontwikkeling af totdat er een quasi-statisch patroon ontstaat. Alhoewel dit patroon zich heel langzaam blijft ontwikkelen naar de evenwichtsconfiguratie, één cluster bestaande uit groepjes uitgelijnde cellen, wordt dit evenwicht nooit bereikt; dit fenomeen wordt *arrested dynamics* genoemd. Wanneer de cellen wel een chemoattractant afgeven ontstaat er een netwerk dat blijft evolueren, wat suggereert dat een netwerk het ware evenwicht is van dat model.

  Met een beter begrip van de rol van cellengte hebben we, in hoofdstuk 3, ons computermodel uitgebreid met pericyten. Dit zijn perivasculaire cellen die, onder andere, aanwezig in de spruiten tijdens angiogenese in het netvlies en in tumoren. Om uit te vinden hoe pericyten bijdragen aan angiogenese hebben we getracht om observaties uit *in vitro* experimenten met endotheelcellen en pericyten te reproduceren met een computermodel. *In vitro* vormen endotheelcellen en pericyten netwerken die, in tegenstelling tot netwerken gevormd door enkel endotheelcellen, ineenstorten in een celcluster. Uit dat cluster vormen zich later weer nieuwe spruiten. Om te testen of en hoe interactie tussen endotheelcellen en pericyten via chemoattractanten de *in vitro* patroonvorming kan veroorzaken hebben we een aantal modelvarianten getest die verschillen in welke cellen welke chemoattractanten afgeven. Hiervoor hebben we een model gemaakt met lange endotheelcellen en ronde pericyten die beide een eigen chemoattractant afgeven. Aan dit basismodel hebben we extra chemoattractanten voor beide celtypes toegevoegd. Welke cellen deze extra chemoattractanten afgeven verschilt per model variant. Wanneer pericyten een chemoattractant afgeven voor endotheelcellen en vice versa ontstaan er netwerken die ineenstorten, zoals ook gebeurd in de *in vitro* experimenten. Met één aanpassing kan ook spruitvorming vanuit het celcluster gereproduceerd worden: Niet pericyten maar de endotheelcellen direct naast pericyten geven de chemoattractant voor endotheelcellen af. Deze resultaten suggereren dat interactie tussen pericyten en endotheelcellen, via chemoattractanten, het collectieve gedrag van deze cellen beïnvloedt en daardoor een rol kan spelen in angiogenese. Lopend onderzoek moet uitwijzen of deze interacties inderdaad een rol spelen in het collectieve

gedrag van endotheelcellen en pericyten tijdens angiogenese.

Het onderzoek gepresenteerd in hoofdstuk 4 heeft betrekking op de verschillen in twee suptypes van endotheelcellen: tipcellen die de spruiten leiden, en de stalkcellen die de tipcellen volgen en verlenging van de spruit mogelijk maken door celgroei. Alhoewel differentiatie van tipcellen en stalkcellen noodzakelijk is in *in vivo* angiogenese hebben computermodellen en *in vitro* studies laten zien dat netwerken ook kunnen vormen met één type endotheelcel. Om nieuwe inzichten te verkrijgen over hoe tipcellen kunnen bijdragen aan de vorming van bloedvaten hebben we een bestaand angiogenese model uitgebreid met tip- en stalkceldifferentiatie, zonder daarbij gebruik te maken van a priori aannames met betrekking tot het gedrag van beide celtypes. Door systematisch het gedrag van tipcellen te variëren hebben we gezocht naar eigenschappen waarvoor het gedrag van de gemodelleerde tipcellen overeenkomt met dat van echte tipcellen: tipcellen leiden spruiten en beïnvloeden de morfologie van de gevormde netwerken. Hieruit volgde de modelvoorspelling dat tipcellen minder aangetrokken zijn tot een autocriene chemoattractant dan stalkcellen. Deze voorspelling komt overeen met het expressiepatroon van de endotheelcel chemoattractant *Apelin*. We hebben de modelvoorspelling getest in een *in vitro* model van spruitvorming en dit model was inderdaad gevoelig voor Apelin.

In dit proefschrift hebben we interactie tussen cellen met verschillend gedrag tijdens angiogenese onderzocht. Met high-throughput simulatie-experimenten waarin we de interacties tussen endotheelcellen en pericyten via chemoattractanten variëren hebben we gevonden dat zulke interactie verantwoordelijk kunnen zijn voor de patronen die endotheelcellen en pericyten vormen in *in vitro* experimenten. Met een soortgelijke aanpak hebben we gezocht naar gedrag waarvoor de tipcellen in het computermodel zich gedragen zoals echte tipcellen. Op deze wijze hebben we gevonden dat de lage sensitiviteit van tipcellen voor Apelin ervoor kan zorgen dat zij spruiten leiden en de morfologie van het vasculaire netwerk beïnvloeden. Alles bij elkaar hebben we in dit proefschrift mogelijke rollen voor pericyten en tipcellen in angiogenese herleid door middel van high-througput simulatie-experimenten.

Dankwoord

Woensdagavond 21 mei, terwijl ik een een spelletjescafé in Parijs aan het winnen ben, krijg ik een mailtje van mijn promotor met de bevrijdende mededeling dat mijn proefschrift is goedgekeurd. Vierenhalf jaar onderzoek en schrijven zijn eindelijk klaar en het proefschrift is af. Hoewel promoveren soms een eenzame bezigheid is, was dit proefschrift er niet geweest zonder de directe en indirecte hulp van velen. Op deze plaats wil ik deze mensen bedanken.

De eerste die ik wil bedanken is mijn promotor: Roeland Merks. Toen ik Roeland bijna 5 jaar geleden voor het eerst ontmoette werd ik meteen besmet met zijn enthousiasme voor het modelleren van biologische groei. Tijdens mijn promotie is dit enthousiasme een bron van motivatie geweest. Roeland, enorm bedankt dat ik onder jouw begeleiding mij heb mogen ontwikkelen als onderzoeker, mijn sterke kanten verder heb kunnen ontwikkelen en mijn zwakke kanten heb kunnen verbeteren.

Naast mijn promotor wil ik een aantal mensen bedanken die direct betrokken zijn geweest bij mijn onderzoek. Voor het onderzoek met pericyten heb ik samengewerkt met Henri Versteeg. De experimentele data van Henri was essentieel voor het onderzoek en de discussies over het project waren erg nuttig. Voor het onderzoek met tip- en stalkcellen wil ik Erik van Dijk en Marchien Dallinga bedanken. Erik, ik heb dankbaar gebruik gemaakt van het tipcelselectie model waarmee ik nu zeer mooie resultaten heb verkregen. Marchien wil ik bedanken voor het uitvoeren van de validatie-experimenten en de discussies over tip- en stalkcellen. Daarnaast wil ik Marchien ook bedanken voor het tonen van oprechte interesse in modelleren. Dit heeft mij gemotiveerd om meer samenwerking te zoeken met experimentalisten.

Binnen Roeland's groep heb ik met veel plezier samengewerkt met Milan, Michael, Josephine, Frederik, Sonja, Erik, Andràs, René, Remi, Séverine, Floriane, Harold, Lisanne, en iedereen die ik hier vergeten ben. Sonja wil ik bedanken voor het vele proofreaden en de steun tijdens de laatste fase van mijn promotie. Daarnaast waren de vele kopjes thee en chocolademelk een welkome afleiding tijdens de lange werkdagen en een goede manier om de proefschrift-frustraties van mij af te praten. Michael wil ik bedanken voor zijn gezelschap als mijn kamergenoot. Het was enorm fijn om mijn kamer te delen met iemand die ook de *nerdy things in life* kan waarderen, zoals mooie Python code,

Emacs, en *chocolate pi*.

Ook de overige leden van de *Life Sciences* groep wil ik bedanken. De grote, volle kaart met alle lieve boodschappen is een mooie herinnering aan mijn tijd op het CWI. Omdat de Life Science groep in de de laatste jaren enorm is gegroeid, kan ik hier niet iedereen bedanken. Een aantal mensen wil ik toch nog even persoonlijk bedanken. Christine wil ik bedanken voor het samen theeleuten, waarbij ik oefende met langzaam spreken en Christine met Nederlands spreken. Jaldert wil ik bedanken voor zijn gezelschap als mijn kamergenoot. Hoewel we altijd met de rug naar elkaar toe hebben gezeten heb ik de periode als kamergenoot met Jaldert als gezellig, en nuttig beschouwd.

Als laatste wil ik mijn familie en vrienden bedanken voor hun steun tijdens mijn promotie. Jos, Mar, Marije en Jean bedankt voor jullie warme welkom in Amsterdam. Jullie gastvrijheid heeft mij veel geholpen bij de overgang van Eindhoven naar Amsterdam. Susan, bedankt voor de hulp bij het vinden van een outfit voor de verdediging. Peter, Niek, en Marieke, ik wil jullie bedanken voor alle steun tijdens mijn promotie. Het is enorm fijn om te weten dat er mensen zijn die naar je willen luisteren, en met raad en daad willen bijstaan.

Publications

Refereed journal articles and book chapters

M.M. Palm, H.H. Versteeg and R.M.H. Merks, *Diffusive signaling between endothelial cells and pericytes can cause network collapse and subsequent sprouting* (in preparation).

F. Lignet, A. Emde, M.M. Palm, Y. Yarden, E. Grenier, R.M.H. Merks and B. Ribba, *Explaining morphogenesis of mammary epithelial spheroids overexpressing HER2: a cell-based computational model* (in preparation).

M.M. Palm, M.G. Dallinga, E. van Dijk, I. Klaassen, R.O. Schlingemann and R.M.H. Merks, *Computational Screening of Angiogenesis Model Variants Predicts that Apelin Signaling Helps Tip Cells Move to the Sprout Tip to Accelerate Sprouting* (submitted).

M.M. Palm and R.M.H. Merks, *Large-scale parameter studies of cell-based models of tissue morphogenesis using* CompuCell3D *or* VirtualLeaf, Tissue Morphogenesis, Methods in Molecular Biology, 2014 (in press).

M.M. Palm and R.M.H. Merks, *Vascular networks due to dynamically arrested crystalline ordering of elongated cells*, Physical Review E, Volume 87(1), 2013.

S.E.M. Boas, M.M. Palm, P. Koolwijk and R.M.H. Merks, *Computational Modeling of Angiogenesis: Towards a Multi-Scale Understanding of Cell-Cell and Cell-Matrix Interactions*, Mechanical and Chemical Signaling in Angiogenesis, Studies in Mechanobiology, Tissue Engineering and Biomaterials Volume 12, 2013, 161-183.

Conference proceedings

M.M. Palm, M.N. Steijaert, H.M.M. ten Eikelder, P.A.J. Hilbers, *Modeling molecule exchange at membranes*, Proceedings of the Third International Conference on the Foundations of Systems Biology in Engineering; Denver, Colorado (2009).

Selected oral & poster presentations

M.M. Palm, M.G. Dallinga, E. van Dijk, I. Klaassen, R.O. Schlingemann and R.M.H. Merks, *A parameter study of a computational angiogenesis model suggests that limited Apelin sensitivity enables tip cells to lead sprouts*, 9th European Conference on Mathematical and Theoretical Biology; Gothenburg, Sweden (2014).

M.M. Palm, E. van Dijk, K.A. Feenstra and R.M.H. Merks, *How tip cells contribute to Angiogenesis: Exploring specialized cell behavior in a cell-based model*, 5th International Conference on Computational Bioengineering; Leuven, Belgium (2013).

M.M. Palm and R.M.H. Merks, *A parameter sensitivity analysis to identify cell properties for tip cells in a Cellular Potts model of blood vessel formation*, Probabilistic Cellular Automata workshop; Eindhoven, the Netherlands (2013).

M.M. Palm and R.M.H. Merks, *Tip-stalk cell differentiation enables fast formation of highly connected vascular networks*, Annual meeting of the Dutch Society for Theoretical Biology; Schoorl, the Netherlands (2012).

M.M. Palm and R.M.H. Merks, *The role of cell elongation in the formation of vascular networks*, 8th European Conference on Mathematical and Theoretical Biology; Krakow, Poland (2011).

M.M. Palm and R.M.H. Merks, *The role of cell elongation in the formation of vascular networks*, Annual meeting of the Dutch Society for Theoretical Biology; Schoorl, the Netherlands (2011).

M.M. Palm and R.M.H. Merks, *The role of cell shape and rigidity in vascular network formation*, Spring meeting of the Institute for Programming research and Algorithmics; Vlijmen, the Netherlands (2011).

M.M. Palm and R.M.H. Merks, *Cell shape and rigidity can be sufficient for vascular network formation*, 4th International Meeting on Angiogenesis; Amsterdam, the Netherlands (2011).

M.M. Palm and R.M.H. Merks, *The role of cell elongation in the formation of vascular network*, 2nd annual symposium of the Netherlands Consortium for Systems Biology; Soesterberg, the Netherlands (2010).

Curriculum vitae

Margriet Palm was born on the 26th of February of 1985 in Malden (The Netherlands). From 1997 to 2003 she attended the Kandinsky College in Nijmegen, were she graduated in 2003. In that same year she moved to Eindhoven to study Biomedical Engineering at the Eindhoven University of Technology. During the masters program she worked on computational projects addressing the bioinformatical analysis of biological pathways, the development of signaling networks using evolutionary algorithms, and the integration of signaling network models. Part of this work was carried out as an intern at the Friedrich-Schiller-Universität in Jena (Germany). In 2009 she obtained her masters degree *cum laude* with a thesis "Partial and Temporal Modelling of Chemical Reaction Networks - A Comparison of the Particle Based Stochastic Simulator *Smoldyn* and Classic Reaction Diffusion Equations".

 Margriet started as a PhD student in the Life Sciences group of *Centrum Wiskunde & Informatica* (CWI) in Amsterdam (the Netherlands) under the supervision of Roeland Merks. As of January 2014, she is working as a postdoctoral researcher at the *Institut National de Recherche en Informatique et en Automatique* (INRIA) in Rocquencourt (France) in the Multicellular Systems Biology group headed by Dirk Drasdo.